Precision Control of High Speed Ball Screw Drives

by

Amin Kamalzadeh

A thesis
presented to the University of Waterloo
in fulfillment of the
thesis requirement for the degree of
Doctor of Philosophy
in
Mechanical Engineering

Waterloo, Ontario, Canada, 2008

AUTHOR'S DECLARATION

I hereby declare that I am the sole author of this thesis. This is a true copy of the thesis, including any required final revisions, as accepted by my examiners.

I understand that my thesis may be made electronically available to the public.

Abstract

Industrial demands for higher productivity rates and more stringent part tolerances require faster production machines that can produce, assemble, or manipulate parts at higher speeds and with better accuracy than ever before. In a majority of production machines, such as machine tools, ball screw drives are used as the primary motion delivery mechanism due to their reasonably high accuracy, high mechanical stiffness, and low cost. This brings the motivation for the research in this thesis, which has been to develop new control techniques that can achieve high bandwidths near the structural frequencies of ball screw drives, and also compensate for various imperfections in their motion delivery, so that better tool positioning accuracy can be achieved at high speeds.

A precision ball screw drive has been designed and built for this study. Detailed dynamic modeling and identification has been performed, considering rigid body dynamics, nonlinear friction, torque ripples, axial and torsional vibrations, lead errors, and elastic deformations. Adaptive Sliding Mode Controller (ASMC) is designed based on the rigid body dynamics and notch filters are used to attenuate the effect of structural resonances. Feedforward friction compensation is also added to improve the tracking accuracy at velocity reversals. A bandwidth of 223 Hz was achieved while controlling the rotational motion of the ball screw, leading to a servo error equivalent to 1.6 um of translational motion.

The motor and mechanical torque ripples were also modeled and compensated in the control law. This improved the motion smoothness and accuracy, especially at low speeds and low control bandwidths. The performance improvement was also noticeable when higher speeds and control bandwidths were used. By adding on the torque ripple compensation, the rotational tracking accuracy was improved to 0.95 um while executing feed motions with 1 m/sec velocity and 1 g acceleration.

As one of the main contributions in this thesis, the dynamics of the 1st axial mode (at 132 Hz) were actively compensated using ASMC, which resulted in a command tracking bandwidth of 208 Hz. The mode compensating ASMC (MC-ASMC) was also shown to improve the dynamic stiffness of the drive system, around the axial resonance, by injecting additional damping at this mode. After compensating for the lead errors as well, a translational tracking accuracy of 2.6 um was realized while executing 1 m/sec feed motions with 0.5 g acceleration transients. In terms of bandwidth, speed, and accuracy, these results surpass the performance of most ball screw driven machine tools by 4-5 times.

As the second main contribution in this thesis, the elastic deformations (ED) of the ball screw drive were modeled and compensated using a robust strategy. The robustness originates from using the real-time feedback control signal to monitor the effect of any potential perturbations on the load side, such as mass variations or cutting forces, which can lead to additional elastic deformations. In experimental results, it is shown that this compensation scheme can accurately estimate and correct for the elastic deformation, even when there is 130% variation in the translating table mass. The ED compensation strategy has resulted in 4.1 um of translational accuracy while executing at 1 m/sec feed motion with 0.5 g acceleration transients, without using a linear encoder. This result is especially significant for low-cost CNC (Computer Numerically Controlled) machine tools that have only rotary encoders on their motors. Such machines can benefit from the significant accuracy improvement provided by this compensation scheme, without the need for an additional linear encoder.

Acknowledgements

I would like to express my sincere gratitude to my supervisor, Dr. Kaan Erkorkmaz, for the support and knowledge he has provided to me during my graduate studies. It has been a pleasure and a great experience working with him.

I would also like to acknowledge my friends and colleagues at the Precision Controls Laboratory (PCL), as well as the faculty and staff members of the University of Waterloo, Mechanical and Mechatronics Engineering Department. In particular, I would like to thank Dr. Amir Khajepour for his support and guidance, and Mr. Robert Wagner and Mr. Andy Barber for their help in design and manufacturing of the experimental setup.

I would like to thank Mr. Wilson Wong, my good friend and colleague from PCL, who has helped me in the early stages of real-time software coding and instrumentation.

Finally, I greatly appreciate the encouragement, support, and love of my dear family, which truly made my graduate studies possible.

Dedication

I dedicate this thesis to Nahal Doroudian who accompanied me along the way and provided support, encouragement, and sacrifice. I deeply appreciate all her help and support.

Table of Contents

List of Figures

List of Tables

Chapter 1
Introduction

Ball screw drives are currently the most common means of delivering high precision motion in work machines, such as machine tools, where both high rigidity and positioning accuracy are required. They have several distinctive advantages such as low cost, high mechanical stiffness, large displacement stroke, and the ability to provide robustness to the servo system against work (e.g. cutting) forces and load inertia variations due to their inherent gear ratio. However, because of their contact-type design ball screw drives are subject to wear. They are also limited by lower acceleration and velocity values, compared to direct drives (e.g. linear motors), which are gradually becoming more accepted in the machine tool industry. However, linear motors are significantly more expensive and their control is more challenging, due to the lack of a motion transmission ratio. This results in the disturbances or load variation to be directly felt by the motor, thereby bringing serious robustness issues. Hence, as tried and tested technology, ball screw drives are still in widespread use in machine tools as well as other types of production machinery. In fact, major machine tool builders continue to invest in and maintain their own dedicated production lines to manufacture the ball screw drives required for their machines.

The challenges associated with controlling any type of feed drive system, whether it is ball screw-driven or direct drive based, are achieving high positioning accuracy at elevated speeds and accelerations; maintaining a sufficient amount of stiffness over a wide frequency range for disturbance force rejection; and delivering a specified performance in a robust manner in the presence of acceptable variations in the feed drive's dynamics. With the recent advances in high speed machining, maintaining the dynamic tool positioning accuracy has become more important than ever before, in order to be able to take advantage of the productivity gains facilitated by high cutting speeds [57]. This in return brings new challenges in terms of control law design. High dynamic accuracy requires the positioning bandwidths to be greater than even before [53], in order to follow the rapidly varying tool commands without violating the part's geometric tolerances. The trend is now towards new motion control techniques that can achieve responsive frequency ranges (i.e. bandwidths) beyond 100 Hz. This requires higher sampling frequencies and finer position feedback to be used; both of which are available through more powerful real-time computers and high resolution position sensors (i.e. sinusoidal encoders or laser interferometers). In addition, it is vital to have a profound understanding of the dynamics that govern the response of a feed drive system, so that adequate compensators can be designed that take full advantage of its physical capabilities. This is

essential for achieving the highest possible dynamic accuracy and disturbance rejection characteristics.

This thesis follows a systematic approach in modeling the dynamics of ball screw drives and introduces new control techniques that deliver higher motion accuracy at elevated speeds. All modeling and control work is carried out on a high precision ball screw drive, supported on air guideways, that was built at the Precision Controls Laboratory at the University of Waterloo. The setup is instrumented with multiple position sensors at different locations, which allows detailed physical models and new control techniques to be developed and experimentally validated.

Henceforth, the proceeding chapters in this thesis are organized as follows:

A literature review on the existing modeling and control techniques for ball screw drives is presented in Chapter 2. In particular, the high order dynamics comprising of axial and torsional vibrations is of interest, as one of the goals in this thesis is to develop new control techniques that can achieve bandwidths in the vicinity of these structural modes. In addition, imperfections of the ball screw's motion delivery originating from lead errors and motion loss in the preloaded nut are also of concern. Other issues that are reviewed are the rigid body dynamics, friction characteristics, torque ripples, thermal expansions, and elastic deformations. Compensation strategies that deal with such effects are also surveyed.

Basic dynamics of the ball screw drive are modeled and identified in Chapter 3, comprising of rigid body motion, current loop dynamics, nonlinear friction characteristics, as well as the torsional and axial vibrations. The vibration modes are modeled using Finite Element and analytical approaches. They are validated experimentally with frequency response measurements. The models and parameters identified in this chapter are used in the following chapters for controller design and stability analyses.

In Chapter 4, the basic control methodology chosen in this thesis, which is Adaptive Sliding Mode Control (ASMC), is introduced and used for controlling the rigid body dynamics. The general ASMC formulation, developed by Slotine and Li [60] and further improved by Zhu et al. [75], is presented. As a special case, the control of a rigid body based plant with an unknown external disturbance is studied. This case boils down to the well-known PID controller with feedforward acceleration and velocity compensation terms. However, the ASMC design provides an efficient model-based means of tuning the feedback and feedforward gains. In order to improve the servo tracking accuracy at motion reversal, feedforward friction compensation is applied. In addition, to avoid exciting the structural resonances through the control signal, notch filters are designed for the torsional and axial

modes. Two feedback scenarios are studied: the first one using only rotational measurements from the ball screw, and the second one using direct translational position feedback obtained from the table. Rotary feedback results in a collocated control situation, where high bandwidth can be achieved with minimal interference from the 1st axial and 1st torsional modes (respectively at 132 Hz and 445 Hz). However, the translational accuracy of the drive is not guaranteed. In this scenario, active cancellation of the ball screw's torsional vibrations is also investigated. The second case with direct translational feedback, on the other hand, brings a significant limitation in terms of the achievable control bandwidth (<70 Hz). This is due to the non-collocated control situation it causes in terms of the 1st axial mode.

In Chapter 5, the force/torque ripples in the motion delivery, which can occur in both ball screw as well as direct drive systems, are identified, modeled, and compensated in the control law. The torque ripple model comprises of the largest harmonic components, which are identified using a Kalman filter [30] for disturbance observation. It is shown that compensating for the torque ripples can provide a significant improvement in the positioning accuracy and motion smoothness of feed drives, particularly during low speed movements and when there are limitations on the achievable control bandwidth.

In Chapter 6, the ASMC is extended to actively compensate for the dynamics of the 1st axial mode, resulting in the so-called Mode Compensating ASMC (MC-ASMC). This is one of the major contributions in this thesis. The MC-ASMC results in superior positioning accuracy over the rigid body based design which was implemented with notch filtering of the 1st axial mode. The achieved command tracking bandwidth is 208 Hz, which is 4-5 times higher than the bandwidth realized in ball screw driven CNC (Computer Numerically Controlled) machine tools. The MC-ASMC also improves the damping and disturbance rejection characteristics around the 1st axial mode, indicating a more favorable response in terms of avoiding machining chatter vibrations [3]. In conjunction with active vibration damping, the lead errors in the ball screw drive have also been modeled and compensated, which yields a further improvement in the dynamic positioning accuracy. With this developed scheme, a translational tracking accuracy of 2.6 um has been maintained while traversing at 1000 mm/sec speed with 0.5 g acceleration transients. This result surpasses the performance of most ball screw-driven CNC machine tools by 4-5 times in terms of accuracy and speed. Although the MC-ASMC was demonstrated to give highly promising results, during its practical implementation it was seen that tuning this controller was not a trivial task. Hence, in order to aid in the design and safe implementation of MC-ASMC, a detailed stability analysis is conducted and the stability predictions are verified in further tracking experiments, at the end of Chapter 6.

In Chapter 7, a different approach is taken for realizing high positioning accuracy and stiffness. Instead of compensating for the axial vibrations, the quasi-static elastic deformation (ED) is estimated and cancelled out in the control law. A simplified lumped model is used for predicting the torque that is transmitted through the preloaded nut. This model is also capable of capturing the drive's position-dependent flexibility characteristic. Both feedforward and feedback compensation techniques have been investigated.

The feedback based elastic deformation compensation, which is the second major contribution in this thesis, is shown to be robust against dynamic changes (e.g. mass variations) on the load side. This is because this approach continuously monitors the real-time control signal, which helps it detect and account for such perturbations. This compensation strategy results in an additional feedback loop, for which the stability implications have been studied by conducting Nyquist analyses. It is shown that the proposed feedback based ED compensation strategy always results in an improvement in the drive's translational accuracy. This is particularly significant for low-cost ball screw drives that have only rotational feedback, typically on the motor shaft. The performance improvement is also demonstrated when both linear and rotational feedback are available.

During the course of this research, all of the developed control algorithms were validated in tracking experiments, as well as in frequency response command following and disturbance rejection (i.e. impact hammer) tests. Currently the ball screw setup is undergoing retrofits so that these algorithms can also be validated in more realistic machining experiments in the near future.

Chapter 2
Literature Review

The growing demands for high productivity manufacturing have motivated research in new control techniques for multi-axis machines. In order to produce, assemble, or manipulate parts in minimum time without violating their tolerances, multi-axis machines are designed to achieve controlled high-speed and high-accuracy movements. With the recent advances in high speed machining [57], spindle speeds and material removal rates have increased by an order of magnitude in the last two decades. Typical high-speed machine tools today have spindle speeds around 30,000 to 40,000 rpm. To take advantage of such high cutting speeds, the feed drives also need to provide fast tool or part motion, while maintaining or improving the positioning accuracy. This requires the servo system to have a high bandwidth [53] and good disturbance rejection characteristics. This is required to track sudden changes in the commanded position trajectory, while being robust against external disturbances such as machining forces. As another requirement, smooth trajectory generation is also essential in order to constrain the motion commands in the low frequency range. This helps to avoid excessive tracking errors and also prevents exciting the machine's structural vibrations, contributing to the overall machined part quality [2][16].

This chapter reviews some of the research on dynamic modeling and control of ball screw drives. Section 2.1 addresses the work modeling and identification. Section 2.2 focuses on controller design. The conclusions are presented in Section 2.3.

2.1 Modeling of Ball Screw Drives

Dynamic modeling of ball screw drives can be performed at different complexity levels considering various effects such as the rigid body motion, bearing and guideway friction, electrical dynamics, torsional, axial, and bending flexibility, high order vibrations, hysteresis type motion loss in the preloaded nut, and motor and mechanical torque ripples. Rigid body modeling is one of the simplest approaches, which considers the effects of inertia as well as viscous and Coulomb type friction. More advanced modeling that considers torsional, axial, and possibly bending vibrations [49][68][71], the kinematics and dynamics that influence the motion loss in the preloaded nut [11][59][70], the velocity dependent nonlinear friction [5][17][38], and motor torque ripples [45][46][50], enables more accurate prediction of the drive's response. In return, this knowledge can be incorporated into control

law design to achieve better tracking and disturbance rejection characteristics. Some of the research on modeling of ball screw drives is presented in the following.

2.1.1 Rigid Body Dynamics

Rigid body dynamics captures the fundamental behavior which dominates the low frequency range. This essentially consists of rigid inertia, viscous damping, and Coulomb friction effects. Rigid body dynamic identification was performed by Erkorkmaz and Altintas [17] by using the Least Squares [44] approach. In this method, an input signal (u) is provided to the motor, which is proportional to motor torque in the low frequency range, when the motor is operating in current control mode. The motor torque can be expressed in the form $\tau = K_a K_t u$ where K_a and K_t are the current amplifier gain and motor torque constant, respectively. By applying a series of piecewise-constant inputs and using the Least Squares technique on the logged velocity and motor torque data, the inertia and viscous damping parameters can be identified considering the following rigid body dynamic model:

$$\omega(s) = \frac{1}{Js + B}[\tau - T_d] \tag{2.1}$$

Above, $\omega(s)$ is the drive's velocity expressed in the Laplace (i.e. "s") domain. J is the inertia, and B is the viscous damping. T_d is the disturbance imposed by constant Coulomb friction opposing the direction of travel. T_d can be represented with two parameters (T^+ and T^-) in the Least Squares identification, where $T_d = T^+$ when $\omega > 0$ and $T_d = T^-$ when $\omega > 0$.

This technique is used for identifying the rigid body dynamics of the ball screw in Section 3.3.2. More details of the rigid body identification technique can be found in [17] and Appendix A.

2.1.2 Friction

Friction is one of the most significant sources of disturbance in CNC (Computer Numerical Controlled) machines. It typically causes tracking error spikes during motion reversals, which occur at sharp corners or circular arc quadrants in the toolpath. This is due to a sudden and discontinuous change of the true friction value at a zero velocity crossing, to which the controller disturbance adaptation law (or integral action) cannot immediately respond. Hence, accurate identification and pre-compensation of friction helps alleviate the corresponding positioning errors at motion reversals.

Dedicated friction modeling and compensation techniques that consider the Stribeck effect [5] where static friction changes to dynamic friction, has been presented in literature [5][17][38].

Identification of friction can be performed in various ways, among which the use of Kalman filtering [30] to observe the equivalent disturbance has been adopted in this thesis following the work in [17]. This approach was found to be effective in capturing the Stribeck curve accurately. Among compensation techniques, feedforward friction compensation was found to be more effective compared to the feedback approach, as it did not interference with the closed loop dynamics, which can have its own stability implications.

2.1.3 Structural Vibrations

Structural vibrations comprise an essential part of the ball screw drive dynamics. These vibrations, if not adequately dampened out or avoided, can limit the achievable control bandwidth to be significantly below the 1st vibration mode [54]. Accurate knowledge of the vibration modes is necessary for the application of most vibration compensation techniques. Structural vibrations have been modeled in literature through analytical methods [8][68], frequency response measurements [21][62][68] and Finite Element (FE) modeling [1][21][49][62][71].

With knowledge of the vibration modes, feedforward (FF) compensation techniques can be developed which avoid exciting the torsional or axial vibrations of ball screw drives, such as the one presented by Chen and Tlusty [8]. In feedback suppression techniques, a lumped model can be used to represent the dynamics of vibration mode(s). Such a lumped model has been developed by

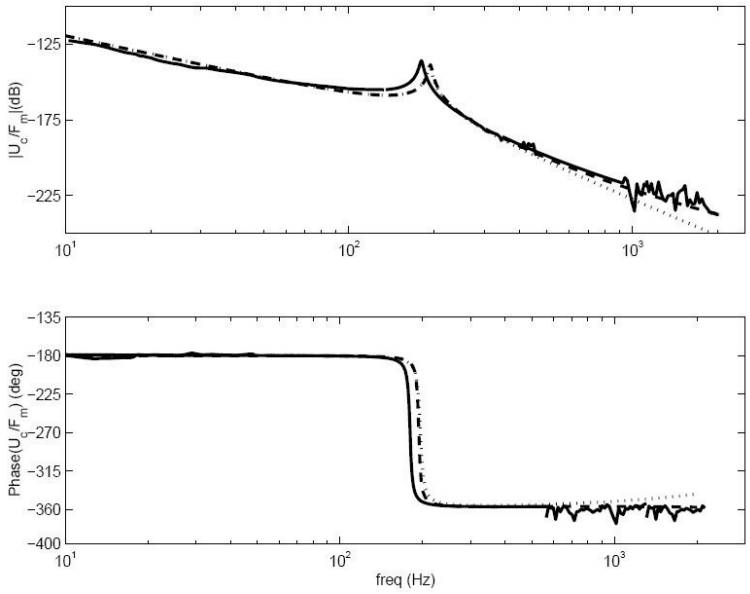

Figure 2.1: Measured (solid line) and predicted (dashed line) transfer functions of ball screw drive (source: Varanasi and Nayfeh [68]).

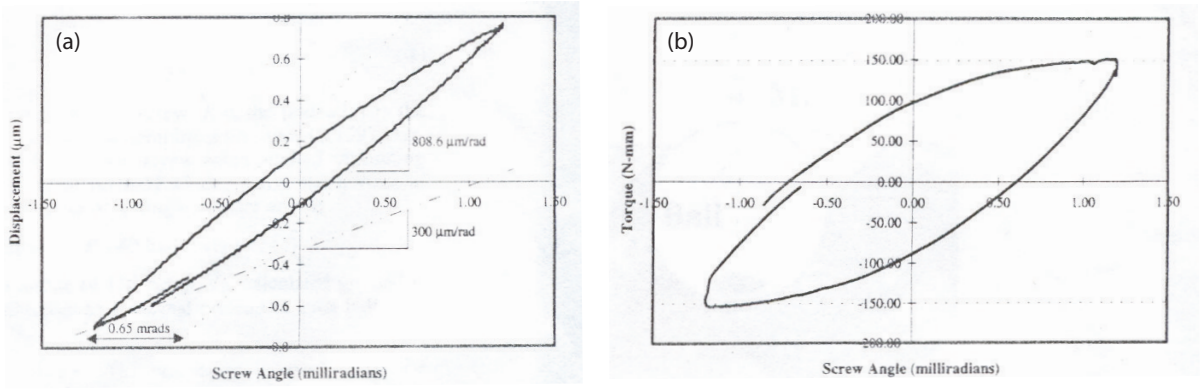

Figure 2.2: Hysteresis behaviour of the ball screw nut (source: Cuttino et al. [11]): (a) Angular displacement hysteresis, (b) Friction torque hysteresis.

Varanasi and Nayfeh [68] analytically, representing the 1st mode of torsional vibration. The frequency response function (FRF) they predicted with their model was verified to be consistent with the measured first axial resonance, as shown in Figure 2.1. Similarly, a lumped model was developed to investigate vibration compensation strategies for the first axial mode in this thesis [32]. Although it is relatively straightforward to match single-mode lumped models to experimental data, higher order models require the use of a modal analysis package to accurately identify the modal parameters and vibration magnitudes contributed by each mode to the final response of the drive.

2.1.4 Motion Delivery in the Preloaded Nut

The motion delivery in the preloaded nut exhibits a hysteresis type nonlinear behavior originating from the rolling, slippage, and elastic deformation of the recirculating balls. Lin et al. [43] conducted a detailed kinematic analysis revealing that the steel balls continuously undergo micro-scale slip between the screw and the nut during the motion transmission. Cuttino et al. [11] pursued this work and successfully modeled the elastic deformation of the balls, related slip phenomena, and hysteresis behavior in the nut mechanism. This motion loss can be observed in the nut linear position vs. ball screw angle and also in the friction torque vs. ball screw angle profiles, as seen in Figure 2.2 [11].

The nonlinear motion loss in the nut produces a translational position error if the control loop is solely closed with angular encoders. This effect can be alleviated to a certain extent by constructing compensation functions or using a linear encoder for direct translational feedback. Both approaches have been followed in this thesis. Since this topic was earlier studied in detail by other researchers, elaborate modeling of the nut dynamics has been kept outside the scope of this thesis.

2.2 Control Law Design

This section reviews some of the contributions on feed drive controls. Simpler techniques like PID or P-PI velocity cascade control are typically implemented by either trial and error tuning, or using simple plant models that capture only rigid body dynamics. More advanced techniques, on the other hand, might require modeling of the axial and torsional vibrations, hysteresis behavior in the nut, nonlinear friction characteristics, lead errors, and motor torque ripples. In return, more detailed models can improve the control law design and ultimately the tracking performance, by helping compensate for such effects. Another important factor in the controller design is robustness against external disturbances (i.e. cutting forces) and changes in the dynamic characteristics of the drive (e.g. viscous friction, inertia, etc.).

2.2.1 Tracking versus Contouring Control

Motion control systems fall into two major categories, which are tracking and contouring control. In multi-axis machines, tracking control refers to independent position control of each axis drive using its own feedback. Contouring control, on the other hand, is the case where the contour error (i.e. geometric deviation from the desired toolpath) is directly estimated and used in the feedback law. Koren [36] initiated the work in contouring control by developing the Cross-Coupling Controller (CCC). This initial design considered solely linear toolpaths in estimating the contour error. This algorithm was later extended to accommodate circular and parabolic toolpaths in [37]. Erkorkmaz and Altintas [14][15] presented a real-time contour error estimation method for arbitrarily shaped toolpaths, and implemented it successfully in a CCC scheme in conjunction with Zero Phase Error Tracking Control (ZPETC) [65]). This helped to simultaneously reduce the contouring and tracking errors. Following the concept of directly reducing the contouring error rather than individual axis tracking errors, Chiu and Tomizuka [9] devised a scheme in which the multi-axis dynamics of the machine tool is projected along the tangential and normal directions of the toolpath. They designed a controller to reduce the tracking errors in the normal and bi-normal directions of motion, which in turn helped to reduce the contour error.

In this thesis, the control algorithms are developed following the tracking control school of thought. This is a more practical approach compared to applying contouring control, especially considering that the robotics and machine tool industries are currently moving towards reconfigurable designs which require more flexibility and interchangeability in the control system implementation. The objective is to indirectly minimize the contour error, by minimizing the tracking errors in the individual axes.

2.2.2 Controller Design for High Accuracy and Vibration Avoidance

The most favorable characteristics in a servo system are the suppression of disturbances and parameter variation effects for a wide frequency range, robustness against unmodeled high frequency dynamics and measurement noise, and a wide command following bandwidth. Pritschow noted the importance of achieving high closed-loop bandwidth in order to track sudden changes in the reference trajectory and also to reject disturbances caused by cutting (i.e. work) forces and friction in [53]. Although many controllers have been developed based on rigid body dynamics alone, neglecting the influence of structural resonances significantly limits the achievable bandwidth [54]. For example, the flexibility of a ball screw causes torsional and longitudinal (i.e. axial) vibrations which can be excited through the control signal or disturbances caused by the cutting force or friction. If the dynamics that govern these vibrations are not considered in the control law design, instability occurs when the feedback gains are increased too much for tight position tracking.

One solution that alleviates this problem to a certain extent is to insert a notch filter into the control loop. Although the notch filter helps to attenuate the resonance effect, it does little to recover the phase margin, which still ultimately limits the achievable bandwidth. Furthermore, if the resonance frequency shifts due to a change in the mass of stiffness parameters, the closed-loop performance or even stability may be lost. Nevertheless, a significant improvement can be obtained by using a notch filter, compared to the pure rigid body-based design case. In machine tool drives, Smith [62] has successfully implemented notch filtering as a solution to this problem. It is important to note that even with notch filtering, structural vibrations are not completely eliminated due to the existence of external disturbance forces and uncertainties in the drive model. On the other hand, active vibration damping, if implemented correctly, can result better servo performance by attenuating the structural vibrations through the use of feedback.

Another preventative measure in avoiding structural vibrations is Input Command Pre-shaping (ICP) (or Input Shaping). Early investigation of this approach was conducted by Smith [61] through the use of Posicast control (*Smith imagined the corresponding control motion as casting a fly, and hence named it Positive-cast or Posicast*). In input shaping, the input command is modified (i.e. pre-shaped) through the construction of a series of impulses in order to achieve vibration-free positioning [29], using a dynamic model of the system. The method is based on the idea that superimposed impulse responses will be cancelled out by each other after the last input impulse is applied [27]. Hyde and Seering [25] presented the theory behind ICP. For a simple case of a sequence with two impulses, they showed that the sequence consists of an impulse and a second impulse with a lesser magnitude occurring after half the period of the damped vibration. The action of adding an

appropriately delayed impulse response, which is performed by the ICP method, is equivalent to adding zeros at the system modes. Similarly, Jones and Ulsoy [29] viewed the ICP technique as a pole-zero cancellation problem and found that it is equivalent to a special case of feedforward notch filtering of the position commands.

Feedforward control can also be used to cancel out the stable dynamics of a closed-loop system, thereby yielding an overall command following transfer function that is very close to unity for a wide frequency range. One of the notable contributions in this area came from Tomizuka [65], who introduced the Zero Phase Error Tracking Controller (ZPETC) which is based on cancellation of all of the closed loop poles and stable closed loop zeros. Theoretically, this controller yields zero phase shift between the commanded and actual position values, and a gain that is very close to unity for a wide frequency range. A similar contribution was also made by Weck and Ye [69]. However, the performance of feedforward controllers is very sensitive to the accuracy of the assumed dynamic model [52], as has been shown by Pritschow and Philipp. In reality, a drive's dynamics, even if they can be identified in detail [66], can vary over time and cannot be kept unchanged. The most important shortcoming of any type of feedforward approach is its open loop nature, which requires closed-loop robustness to be realized in feedback before it can be successfully applied.

As mentioned earlier, a more effective way to deal with structural vibrations is to attempt to attenuate them in feedback control. This facilitates the achievement of a wider closed-loop bandwidth and better disturbance rejection. Chen and Tlusty were among the first to study this concept for machine tool drives, in which they demonstrated the effectiveness of vibration damping using accelerometer feedback in simulations [8]. In recent years, as more powerful control computers and high resolution feedback devices have became available, successful experimental results have been reported by researchers for ball screw drives. Symens et al. [64] used H_∞ robust control with gain scheduling, which helped track the variations in structural dynamics with axis position. Zatarain et al. [72] improved the drive stiffness, damping, and tool positioning accuracy by fusing linear encoder measurements with accelerometer feedback through a Kalman filter. Accelerometer feedback was also used by Symens et al. As a contribution from industry (Siemens AG), Schäfers [56] developed a control loop tuning strategy which emulates the behavior of a mechanical damper, allowing high jerk movements to be executed without vibrating the translational part of the drive. All of these methods enable a significant improvement in the command following bandwidth, dynamic (i.e. frequency dependent) stiffness, and disturbance rejection characteristics.

Recently, Kamalzadeh and Erkorkmaz have developed an active vibration damping and position control strategy for ball screw drives using Adaptive Sliding Mode Control (ASMC) [32]. This

approach utilizes the methodology set forth by Slotine and Li [60] and actively compensates for the dynamics of the 1st axial mode. One nice feature about this controller is that it inherently contains the command following (feedforward) and disturbance rejection (robustness) terms that are synthesized through the solution of one Lyapunov inequality. Compared to other approaches, this control law is relatively easy to design and has been demonstrated to achieve a high command following bandwidth (208 Hz), and good accuracy (2.3 um) during high travel speeds and accelerations (1000 mm/sec, 0.5 g). This controller design is one of the main contributions in this thesis, and is presented in Chapter 6.

ASMC has also been used to control the rigid body dynamics in this thesis. In this case, the vibratory modes have been attenuated by inserting notch filters into the control loop. Active vibration cancellation for the 1st torsional mode, through additional control terms, has also been investigated and reported in [21].

The idea of Sliding Mode Control was pioneered by Utkin [67]. The original idea was based on discontinuous switching of the control signal in order to keep the system states on a "sliding surface", which represents a stable linear differential equation governing how the states should converge to the origin (or to their desired values). Hence, the closed-loop response is dictated by the parameters of the sliding surface. Slotine and Li [60] refined this methodology by developing a general and adaptive framework, which resulted in a continuous and nonlinear control law with Lyapunov-guaranteed stability. Later Zhu et al. [75] provided the stability proof for conducting the parameter adaption within known bounds.

In the early stages of the research in this thesis, many control techniques were investigated such as Pole-Placement, ZPETC, and ASMC. Adaptive Sliding Mode Control was chosen as the foundation for several of the developed compensation techniques, due to its excellent tracking performance and robustness against disturbances and low frequency dynamic variations.

2.2.3 Compensation of Torque/Force Ripples

Variation of the motor torque due to changes in the relative position between the rotor and stator is known as the motor torque ripple. Disturbances, such as motor and mechanical torque ripples, cause inaccurate torque delivery from the drive which in turn can deteriorate the motion control accuracy. Torque ripples can be modeled and compensated as a function of the motor position and the torque command [23][50].

In AC servo-drives, which are becoming the mainstream in machine tool and industrial robotics applications, the torque ripple is composed of cogging torque, reluctance torque, mutual torque, and

the DC current offset torque [24]. Cogging torque originates from the presence of stator slots and has a frequency at which the slots are located along the stator [22]. Reluctance torque is due to the rotor geometry discontinuity (holes, saliencies, and other geometrical discontinuities which interrupt the internal flux). This causes variations in reluctance as the rotor rotates. Mutual torque is due to the interaction between the rotor magnetic field and stator current. Ideally, a motor should produce a constant mutual torque if the stator windings and rotor magnetic field have a perfect sinusoidal distribution. However, since this is not achievable in practice, the produced mutual torque contains higher harmonics which cause the torque ripples [51]. The torque ripple due to DC current offset is caused by the offset in the current sensors and digital to analog converters (DAC) in the current control loop. In optimally designed AC permanent magnet motors, cogging, reluctance, and mutual torque ripples can be neglected [23]. The DC current offset ripples are more dominant among other mentioned factors, due to the offsets in the current sensors and DAC's being difficult to eliminate [24]. Mechanical torque ripples, on the other hand, can be observed when there are minor misalignments in the feed drive mechanism.

Many techniques have been proposed in literature for torque ripple minimization. The first class of these techniques focuses on improving the motor design [7][28][39]. The second class considers injecting additional control signals for canceling out the ripples, by supplying an equivalent current to the motor. This cancellation can be performed in the current or motion control loops. As an example of torque ripple compensation in the current control loop, Parasiliti et al. [50] used a Kalman filter [30] to identify the harmonic components of the magnetic flux linkage and predict the necessary motor current to compensate for the ripples. However, to implement such an algorithm, the current amplifier hardware needs to be modified. In this thesis, torque ripple compensation is realized at the position and velocity control level, which is one level higher and more accessible. This work has been published in [31]. One of the advantages of this approach is that it allows the methodology to be applied on different types of feed drives in a generic manner, without having to modify the current loop. The torque ripple harmonics were identified using a Kalman filter disturbance observer. Details of this work are presented in Chapter 5.

2.2.4 Compensation of Elastic Deformations

Elastic deformations occur in ball screw drives typically due to inertial forces, guideway friction, and cutting forces, which result in elongation and compression of the ball screw. Many of the ball screw drives are controlled based on closing the position loop only with a rotary encoder, as these encoders are less expensive compared to linear encoders. When only rotary position feedback is used, the linear

positioning accuracy suffers due to lead errors, elastic deformations, thermal deformations, and motion loss in the preloaded nut [11][13][26][59][70]. By using direct position feedback through a linear scale, it is possible to alleviate these problems to a certain extent, mainly during steady-state positioning and low frequency movements. However, during high speeds and accelerations, these factors become apparent again; and can deteriorate the dynamic linear accuracy of the drive mechanism. Also, with the use of linear feedback, the inclusion of additional mechanical flexibility (i.e. the axial mode) inside the servo loop can cause the bandwidth to suffer [8][54][68] if the structural resonances are not compensated adequately. Although techniques have been developed to avoid or attenuate structural vibrations by pre-filtering the position commands or inserting notch filters inside the loop [21][27][29][62][69], these techniques usually result in a drop in the position tracking bandwidth compared to using collocated rotary feedback. Moreover, linear encoders typically cost ten times more compared to rotary encoders, and their installation involves additional expenses as well.

Among the above mentioned factors, compensation of the elastic deformations has received attention in motion controls literature. In the robotics field, Zhang et al. studied the "joint torque" feedback technique [73] using a torque sensor in a flexible robot arm mechanism. The joint torque refers to the joint displacement multiplied by the stiffness of the flexible transmission system. This is conceptually equivalent to the "transmitted torque" that is estimated in the elastic deformation compensation scheme presented in Chapter 7 of this thesis. In [73], the authors investigated the idea of injecting negative joint torque feedback to the control signal, and the relation between vibration suppression and disturbance rejection, which refers to the compensation of elastic deformations caused by disturbances. While a negative joint torque feedback is effective in vibration suppression (consistent with Chen and Tlusty's simulations [8] for negative acceleration feedback), it amplifies the effect of disturbances on the end effector position [74]. On the other hand, positive joint torque feedback improves the disturbance rejection characteristics, but has a destabilizing effect on the overall servo system. A similar effect was also observed in the feedback based elastic deformation compensation scheme developed in Chapter 7. However, in this thesis, the instability problem has been mitigated by designing additional filters and applying a detailed stability analysis.

Lim et al. [41][42] adopted the idea of positive joint torque feedback from Zhang et al. [74], and applied it on an X-Y positioning table. Their method works in a feedback manner and rejects the disturbances that cause elastic deformations. However, the performance of this method is limited due to two major shortcomings. First, this technique assumes a constant stiffness parameter for the ball screw drive and does not take into account its position dependent flexibility. Second, the effects of

viscous and Coulomb friction are neglected in computing the transmitted (i.e. joint) torque, which can lead to incorrect estimation of the elastic deformation.

In this thesis, more comprehensive and yet practical elastic deformation compensation strategies have been developed that address the shortcomings of earlier work. A feedforward approach has been developed [33], which considers both the position dependency and the sources of external friction in computing the elastic deformation. This approach is relatively simple but not very robust against parameter changes in the load side of the drive, such as table mass and guideway friction variations. A feedback based technique has also been developed [34], which is more robust and still relatively easy to implement. This technique is considered to be another major contribution in this thesis. Both approaches are detailed in Chapter 7, which deals with the compensation of elastic deformations in ball screw drives.

2.3 Conclusions

This chapter has presented a survey of some of the critical issues related to the modeling and control of ball screw drives. Namely they relate to the rigid body dynamics, friction, elastic deformations, torque ripples, lead errors, thermal deformations, structural vibrations, and motion loss in the preloaded ball-nut mechanism. In the following chapters, some of these issues will be studied in more detail. New control laws will be developed which focus on achieving high command following and disturbance rejection bandwidth through the avoidance or damping of structural vibrations. Also, the achievement of high positioning accuracy will be investigated by compensating for some of the repeatable effects such as torque ripples, lead errors, and elastic deformations.

Chapter 3
Modeling and Identification

3.1 Introduction

Development of high performance motion controllers requires a good understanding of the feed drive dynamics. In this chapter, the most significant dynamics of a ball screw drive, which is used as the primary experimental setup in this thesis, are modeled and experimentally identified. Section 3.2 details the design of the experimental setup. Section 3.3 focuses on the identification of rigid body dynamics, including effects like inertia, viscous friction, and Coulomb friction. The drive parameters, including Coulomb friction torque, are initially calculated using a Least Squares techniques. The friction model is then refined by observing the control signal equivalent friction disturbance using a Kalman filter, while jogging the drive under feedback control at different velocities. The amplifier current loop is also measured, to validate the frequency range in which effective actuation can be realized. Section 3.4 deals with the modeling and identification of the vibratory dynamics. Torsional vibrations are investigated using finite element analysis and frequency response testing. The first axial vibration mode, which is highly significant in terms of influencing the drive's linear positioning accuracy, is estimated through an analytical calculation and validated experimentally. The knowledge of torsional and axial vibration modes is crucial in designing high bandwidth motion controllers. Conclusions of this chapter are presented in Section 3.5.

3.2 Experimental Setup

The high speed ball screw drive built at the Precision Controls Laboratory, University of Waterloo is shown in Figure 3.1. The ball screw, which has 20 mm diameter and 20 mm pitch, is used to drive a table supported on an air guideway system. Actuation is provided through a 3 kW AC servomotor which is connected to the ball screw using a diaphragm-type non-backlash coupling. The motor is operated in current control mode. The bandwidth of the current control loop was measured to be 480 Hz. The ball screw is instrumented at both ends with two high resolution rotary encoders which deliver 5000 sinusoidal signals per revolution. These encoder signals can be reliably interpolated by 400 times in the motion controller, resulting in a position measurement resolution equivalent to 10 nm of table motion. Catalogue rated accuracy of these encoders are equivalent to 200 nm of table motion. For successful vibration measurement, these encoders have been mounted rigidly onto the ball screw and to the machine base. Encoder 1 is located at the free end of the ball screw, and Encoder 2 is right

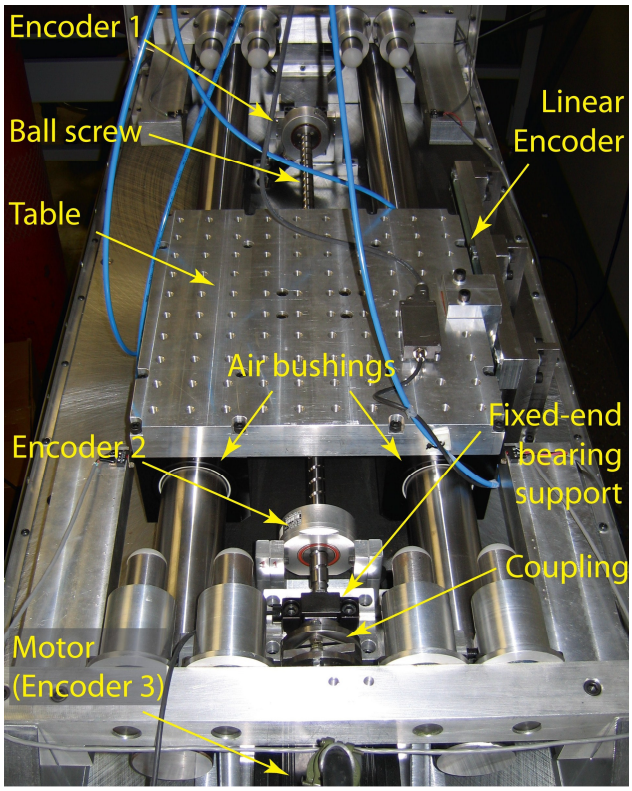

Figure 3.1: Experimental setup.

after the fixed bearing support, as seen in Figure 3.1. A third encoder (Encoder 3) is available on the back of the motor which delivers 16384 quadrature pulses, resulting in a position measurement resolution equivalent to 305 nm of table motion. This study was initially focused on rotary dynamics of the drive, using the measurements obtained from the rotary encoders. Later on, to investigate the axial vibrations and validate the final linear positioning accuracy of the table, a linear encoder with 4 um signal period was retrofitted on the table which provides a measurement resolution of 10 nm and an accuracy of 40 nm, as rated in the catalogue.

The high resolution of the encoders enables accurate detection of the frequency response at different points along the ball screw, by yielding clear acceleration signals after double differentiation with respect to time. Hence, the vibration mode shapes can be observed and verified up to a frequency of 2.5 kHz. The setup is controlled with a dSPACE controller which can achieve a sampling frequency up to 20 kHz.

3.3 Rigid Body Dynamic Identification

The rigid body dynamics comprise the most fundamental characteristics of ball screw drives, which dominate the low frequency behavior. Accurate knowledge of these dynamics is essential for any kind of model-based controller design. Furthermore, these characteristics should be determined before

higher order dynamics such as torsional or axial vibrations, or more complex phenomena like torque ripples, elastic deformations, or lead errors, are modeled and identified. This task is undertaken in the following subsections. In Section 3.3.1, the theoretical value of axis inertia is calculated. This is followed by Least Squares identification of the inertia, viscous damping, and Coulomb friction parameters in Section 3.3.2. Throughout most analyses in this thesis, dynamics of the current control loop is neglected. Validation for this simplification is provided in Section 3.3.3, with experimental measurement of the current loop bandwidth. In Section 3.3.4, the friction model is further refined by using a Kalman filter based disturbance observer. This facilitates correction to the friction parameters that were identified using Least Squares technique and produces an accurate description of the drive's friction characteristics, for feedforward compensation.

3.3.1 Theoretical Inertia Calculation

The overall inertia of the ball screw mechanism is estimated using catalogue and calculated values for different components . The catalogue rated motor and coupling inertias are $m_m = 9.10\times10^{-4}$ kgm^2 and $m_c = 9.013\times10^{-4}$ kgm^2, respectively. The inertia of the ball screw is calculated assuming a cylindrical structure:

$$J_{bs} = \rho l_{bs} \pi \frac{d^4}{32} \tag{3.1}$$

where $\rho = 7850$ kg/m^2 is the density of steel, $l_{bs} = 1.12$ m, is the ball screw length, d=0.02 m is the ball screw diameter, resulting in an equivalent inertia of 1.3810^{-4} kgm^2 for the ball screw. The table mass m_t was measured to be 33.474 kg. This can be expressed as equivalent rotary inertia as:

$$J_t = m_t(\frac{h_p}{2\pi})^2 = 1.38 \text{ x } 10^{-4} \text{ kgm}^2 \tag{3.2}$$

using the ball screw pitch length, $h_p = 0.02$ m. The total equivalent inertia of the ball screw drive can be calculated by summing up the inertia values for the motor, coupling, ball screw, and the table as:

$$J_{eq} = J_m + J_c + J_{bs} + J_t = 2.288 \text{ x } 10^{-3} \text{ kgm}^2 \tag{3.3}$$

This calculation was verified with the inertia estimated using Least Squares parameter identification in Section 3.3.2. The results are shown in Table 3.1, where there appears to be 8.6% difference between the two estimates. This discrepancy likely originates from the coarse approximation of the ball screw as a single-diameter cylinder, which neglects the cross-section area

changes and the helical groove. Nevertheless, an analytical estimate of the total inertia helps check the validity of experimental parameter estimates obtained in Section 3.3.2.

3.3.2 Least Squares Identification of Inertia, Viscous, and Coulomb Friction

Following the analytical estimation of inertia, experimental identification of a simple rigid body dynamic model comprising of inertia, viscous damping, and Coulomb friction, as shown in Figure 3.2, is presented in this section. Coulomb friction is incorporated into the model to avoid a bias in the viscous damping estimate. Following this parameter estimation, the friction model will be further refined using Kalman filtering in Section 3.3.4.

The rigid body dynamics of the drive are captured with the following model:

$$\omega(s) = \frac{1}{Js + B}[\tau - T_d] \tag{3.4}$$

Above, ω is the angular velocity of the ball screw. J is the motor-equivalent total rotary inertia, B is the viscous friction coefficient, and τ is the motor torque. The Coulomb friction T_d is assumed

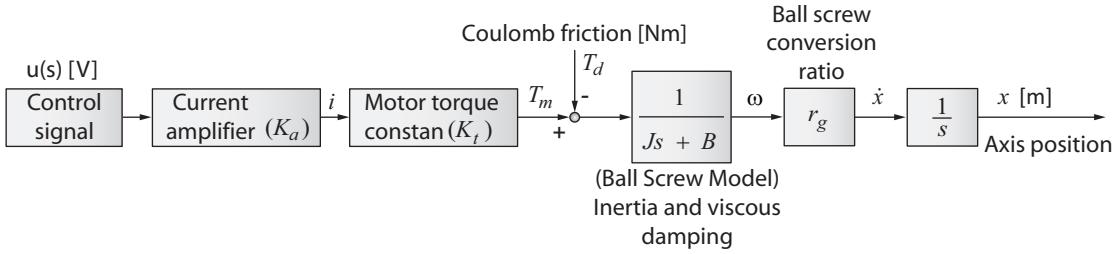

Figure 3.2: Rigid body dynamic model.

Table 3.1: Inertia parameters for the ball screw drive system.

Parameters	Values
Mass of table, air bushing, and other translational moving parts	33.474 kg
Ball screw inertia	1.3810×10^{-4} kgm^2
Coupling inertia	9.0133×10^{-4} kgm^2
Motor inertia	9.1×10^{-4} kgm^2
Total equivalent inertia - computed analytically based on ball screw lead of 20 mm	2.2886×10^{-3} kgm^2
Total equivalent inertia - experimentally identified using Least Squares parameter identification	2.1×10^{-3} kgm^2
Discrepancy between analytically computed and experimentally identified inertia values	8.6 %

to be in the form:

$$T_d = \begin{cases} T_C^+ & for \quad \omega > 0 \\ T_C^- & for \quad \omega < 0 \end{cases} \tag{3.5}$$

The ball screw rotational-to-translational motion conversion ratio is $r_g = h_p/(2\pi) = 3.1831\times10^{-3}$ m/rad. The motor torque can be expressed as $\tau(s) = K_a K_t u(s)$, where $u(s)$ is control input to the amplifier. K_a and K_t are the amplifier gain and the motor torque constants, with catalogue rated values of 1.7193 A/V and 0.57 Nm/A respectively. The axis position can then be expressed as:

$$x(s) = \frac{r_g}{s}\frac{1}{Js+B}[K_a K_t u(s) - T_d(s)] \tag{3.6}$$

In order to simplify the parameter estimation, the high order dynamics of the amplifier are ignored and only a constant amplifier gain (K_a) is considered. The effective frequency range of the current amplifier, for this assumption to hold, is later measured in Section 3.3.3.

The drive parameters were estimated using the Least Squares technique developed in [17]. The applied procedure is explained in Appendix A. A sequence of piecewise constant current commands were applied as the identification input. This input signal was selected in a form which excites the dynamics of interest for Lease Squares identification; that is, the pulse signals are large enough to produce high acceleration for identifying the inertia parameter, and long enough to result in high velocities for identifying the viscous damping parameter. Also, the amplitude of the pulses is varied in order to account for the amplitude dependency caused by the Coulomb friction term. The parameter estimates are summarized in Table 3.2. As mentioned earlier, the equivalent inertia was also calculated analytically using the table and air bushing masses and ball screw, coupling, and motor inertia values. These parameters are listed in Table 3.1. The analytical inertia is found to be close to the experimentally identified inertia with 8.6% error. This error could originate from the

Table 3.2: Identified parameters.

Ball screw drive parameters	
Equivalent inertia $\hat{J}$ kgm^2	2.1×10^{-3}
Viscous damping $\hat{B}$ kgm^2/sec	4.40×10^{-3}
Coulomb friction $\hat{T}_C^+$ N.m	7.30×10^{-3}
Coulomb friction $\hat{T}_C^-$ N.m	-6.68×10^{-3}

simplifying assumptions made when calculating the inertia of various mechanical components, including the ball screw. It could also originate from the discrepancy between the rated and actual amplifier gains and motor torque constants. Nevertheless, there is reasonable match between analytically computed and experimentally identified inertia parameters. From here on, the experimentally identified values are used in controller design and analysis.

It is important to note that when more detailed identification of friction is conducted in Section 3.3.4, it reveals that $\hat{B}$ is initially overestimated and T_C^+ and T_C^- are underestimated in the rigid body model. These parameters will be corrected as a more detailed friction profile is constructed which is a function of the axis velocity.

3.3.3 Identification of the Amplifier Current Loop

The current loop in the amplifier controls the motor current, which should be ideally be proportional to the amplifier input voltage. However, due to power limitations of the amplifier, as well as the motor armature dynamics and the amplifier current control circuitry, the current loop gain drops as the frequency of the input increases. In order to consider a more realistic model of the amplifier, and determine the frequency range up to which the "constant gain" assumption holds, tests have been conducted by applying a sinusoidal input voltage with 8 V amplitude at frequencies ranging from 10 to 2500 Hz, with 2 Hz increments. In these tests, the equivalent motor current was monitored from the amplifier, as shown in Figure 3.3. For each test, a sinusoidal curve was fit to the motor current data in order to measure the amplitude and phase shift of the response. The bode diagram for the motor current response, from input voltage to monitored current, is shown in Figure 3.4. As can be seen, the -3 dB drop occurs around 480 Hz. Although the current monitoring filter available in the amplifier was disabled during these tests, there may still be internal filtering, which could not be avoided. Nevertheless, the measurement indicates that the current loop has a bandwidth of at least 480 Hz.

To get an idea of the most significant dynamics, the frequency response data was also used to fit an analytical transfer function using the Complex Curve Fitting method [40], implemented in MATLAB [10]. A 3rd order model in the form:

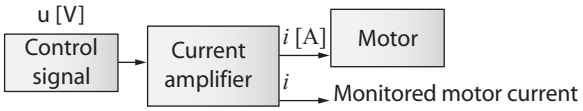

Figure 3.3: Current amplifier and motor block diagram.

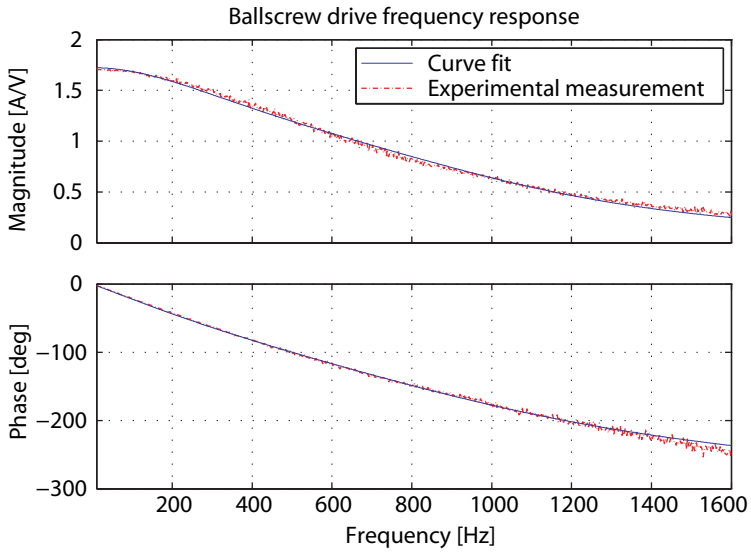

Figure 3.4: Measured current loop frequency response function.

Table 3.3: Poles, zeros, and gain of 3rd order approximation of the current loop.

Poles p_k rad/sec	**Frequency ω Hz**	**Damping ratio ζ**
-4169 + 5115i	1050	0.63
-4169 - 5115i	1050	0.63
-2763	440	1.00
Zero z_1 rad/sec	**Frequency ω Hz**	**Damping ratio ζ**
12949	2061	-1.000
Transfer function gain K_a A/V		1.7237

$$G_a(s) = K_a \frac{(s - z_1)}{\prod_{k=1}^{3}(s - p_k)} \tag{3.7}$$

was found to capture the observed current loop dynamics with adequate closeness. The poles, zeros, and gain are presented in Table 3.3. As indicated, the lowest frequency pole occurs at 440 Hz, roughly determining the usable current control bandwidth. However, the amplifier can still deliver current effecting higher frequencies, but with phase lag. This needs to be kept in mind during the controller design and stability analyses in proceeding chapters. For the purpose of identifying the rigid body dynamics, approximating the current amplifier with a fixed gain does not produce any detrimental error.

3.3.4 Detailed Identification of Friction Characteristics using a Kalman Filter

Detailed identification of friction is performed by moving the table under closed loop control at constant speeds and monitoring the control signal equivalent disturbance, which attributes the total friction in the drive, using a Kalman filter [30]. This scheme has been illustrated in Figure 3.5. In order to stabilize the feed drive, the Sliding Mode Controller, developed later in Chapter 4, is utilized. The Kalman filter design used for friction observation has been adopted from the methodology in [17] and [18], and is summarized in Appendix B. The Kalman filter can be expressed as a discrete-time model as:

$$\begin{bmatrix} \hat{x}(k) \\ \hat{\omega}(k) \\ \hat{d}(k) \end{bmatrix} = (\mathbf{I} - \mathbf{K}_{obs}\mathbf{C})\mathbf{A} \begin{bmatrix} \hat{x}(k-1) \\ \hat{\omega}(k-1) \\ \hat{d}(k-1) \end{bmatrix} + (\mathbf{I} - \mathbf{K}_{obs}\mathbf{C})\mathbf{B}\left[u(k-1)\right] + \mathbf{K}_{obs} \begin{bmatrix} x_m(k) \\ \omega_m(k) \end{bmatrix} \tag{3.8}$$

Above, $\mathbf{K}_{obs}$ is the observer gain, $\mathbf{A}$, $\mathbf{B}$, and $\mathbf{C}$ represent the discrete-time state space matrices of the rigid body dynamics, with numerical values presented in Appendix B. $\hat{d}$ is the estimated disturbance, mainly attributed to the total nonlinear friction in the ball screw mechanism, when there are no other disturbance forces (such as cutting), acting on the ball screw drive. $\hat{x}$, $\hat{\omega}$, x_m, and ω_m are the estimated and measured position and velocity values, respectively. A typical disturbance

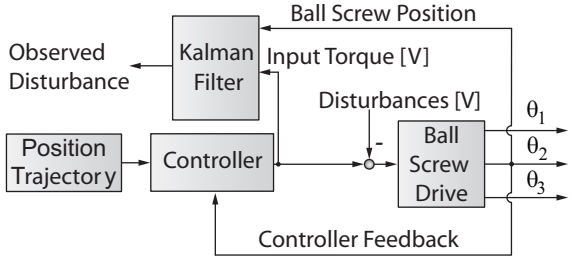

Figure 3.5: Kalman filtering.

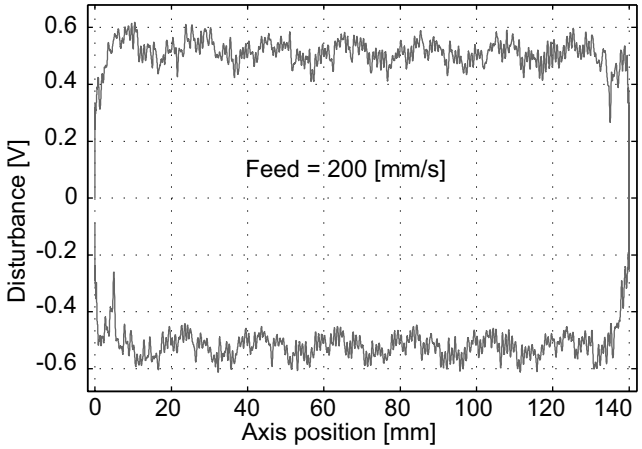

Figure 3.6: Estimated disturbance with Kalman filtering, jogging at a speed of 200 mm/sec.

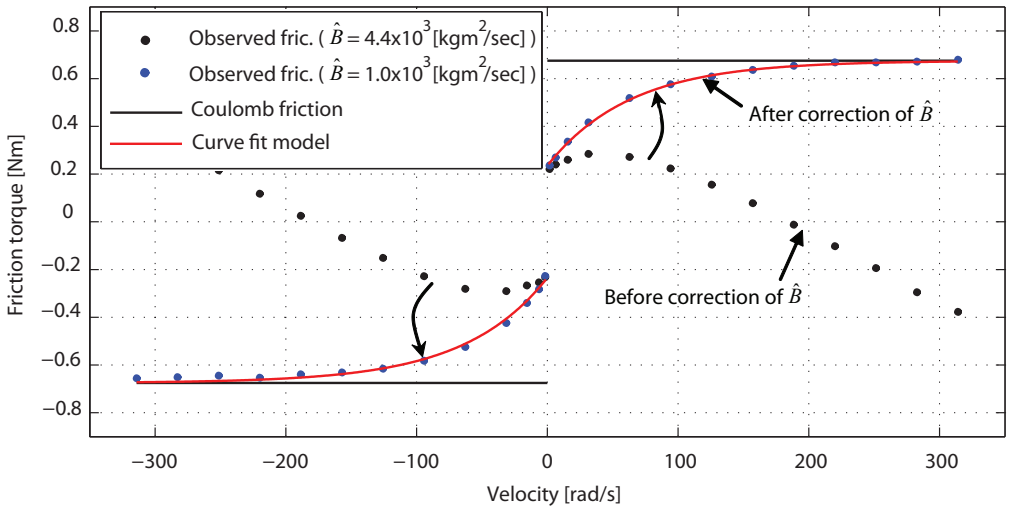

Figure 3.7: Observed and curve fit friction models.

estimate recorded while jogging the axis back and forth at 200 mm/sec is shown in Figure 3.6.

The average value of the disturbance attributes to friction and appears reasonably consistent over the range of motion [17]. Although the friction effect is isolated from the influence of torque ripples by averaging the disturbance at a constant speed, the effect of any constant disturbance such as an offset in the amplifier gain is absorbed in combination with the friction, in the identification process. Higher frequency harmonics are also evident, which correspond to 1x, 2x, 4x, 8x, and 12x of the motor rotation speed. These harmonics were observed to be quite repeatable and are attributed to the torque ripples in the motor and drive mechanism, which are studied in more detail in Chapter 5. The focus in this section is only on the friction, which is obtained by averaging the disturbance values observed while traveling at a constant velocity . By repeating the test for different speeds, the friction characteristic of the ball screw drive can be constructed as a function of motor velocity, as shown in Figure 3.7.

It should be noted that due to the earlier over-estimation of the viscous damping term $\hat{B}$, the average values of friction appear to be diminishing with increasing velocity, following a linear trend. By estimating the corresponding negative slope (-3.385×10^{-3} kgm^{2}/sec), the value of $\hat{B}$ was corrected as $\hat{B}'$=4.40×10^{-3}-3.385×10^{-3}=1.015×10^{-3} kgm^{2}/sec. The Kalman filter was redesigned and the experimentally recorded data was filtered once again, Now, it is seen that the high-velocity values of friction converge to constant asymptotes, which correspond to the updated values of Coulomb friction ($[T_C^+]'$=+0.675 Nm and $[T_C^-]'$= - 0.675 Nm), as seen in Figure 3.7.

A friction model was fit to the observations in the form, similar to the one used by Kato et al. [35]:

$$T_{fric} = \text{sgn}(\omega)[T_s + T_d(1 - e^{-|\omega|/\Omega})] \tag{3.9}$$

Here, T_{fric} [Nm] is the friction torque, ω [rad/sec] is motor angular velocity, $\Omega = 64$ rad/sec is the velocity constant, T_s = 0.235 Nm is the static friction torque, and T_d = 0.440 Nm such that $T_s + T_d$ =0.675 Nm equals the Coulomb friction torque. It should be noted that the overall shape of the friction model is different from the typical friction characteristics of feed drives with lubricated guideways. Due to the use of air bushings, the friction originating from the linear guideways is almost eliminated. The remaining friction originates from the support ball bearings, encoders, nut assembly, and the motor's internal bearings. Due to the dominance of rolling type friction, the Stribeck effect [5], which is recognized as a transition from a larger static friction to a smaller dynamic friction, is not observed.

The curve fit friction model represents the actual friction in the drive system more realistically than the simple Coulomb friction model used earlier in Least Squares parameter estimation. Furthermore, more accurate estimate of the viscous damping is also obtained. Hence, the analytical model in Eq. (3.9) and the updated value of the viscous damping $\hat{B}'$ have been used in the proceeding chapters for control law and feedforward compensation design.

3.4 Vibratory Dynamics

Insight into the vibratory dynamics of ball screw drives plays a crucial role in designing high bandwidth control laws, which is one of the aims in this thesis. Sections 3.4.1 presents a simple Finite Element approach to modeling the ball screw torsional vibrations. The finite element analysis results are verified and refined using experimental frequency response measurements. In Section 3.4.2, the first axial mode, which has a major influence on the achievable linear positioning bandwidth and accuracy, is modeled and measured experimentally. Results of the modeling and identification work on vibratory dynamics will be incorporated into controller design in the proceeding chapters, as notch filters and active vibration damping techniques to achieve higher control bandwidth and smooth tracking motion.

3.4.1 Finite Element Modeling of Torsional Modes and Experimental FRF Validation

The torsional vibration modes of the drive were modeled in ANSYS® software. The developed FE model is shown in Figure 3.8. Modal analysis was conducted to investigate the torsional resonances. The ball screw was modeled as a rod with a varying outside diameter at different sections. The motor shaft was modeled as a rigid cylinder with the inertia reported in the motor catalogue. The coupling

was modeled with two cylinders, attached rigidly to the motor and to the ball screw, connected with a torsional spring in between representing the coupling flexibility. The catalogue values were used for the inertia and flexibility of the coupling.

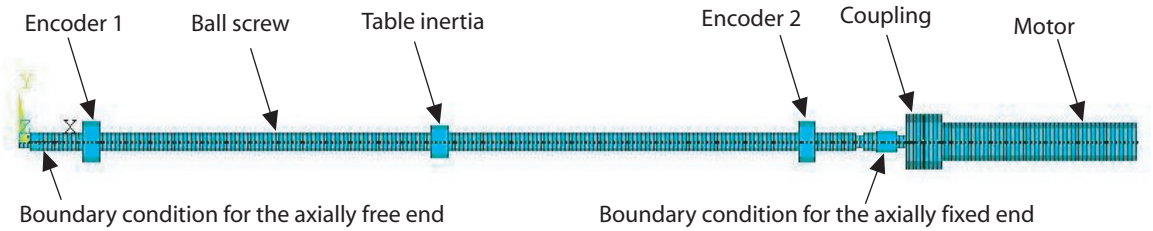

Figure 3.8: The finite element model in ANSYS.

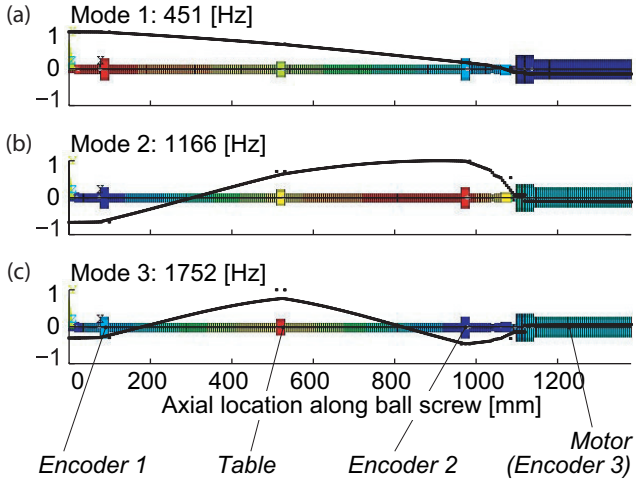

Figure 3.9: Torsional modes: (a) 1st mode, (b) 2nd mode, (c) 3rd mode.

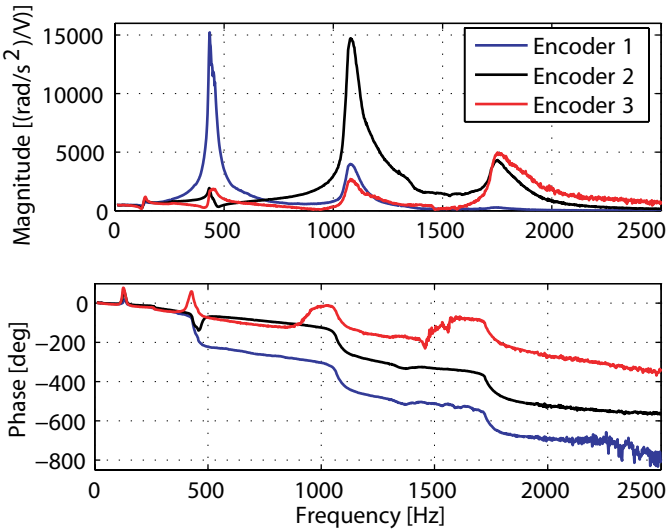

Figure 3.10: Measured open loop acceleration FRFs.

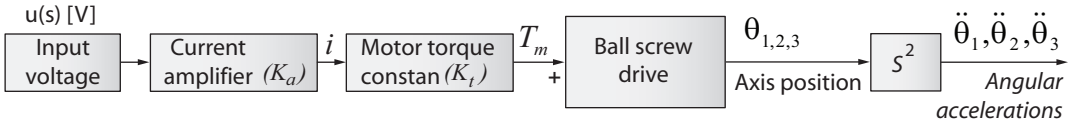

Figure 3.11: Amplifier, motor, and ball screw block diagram.

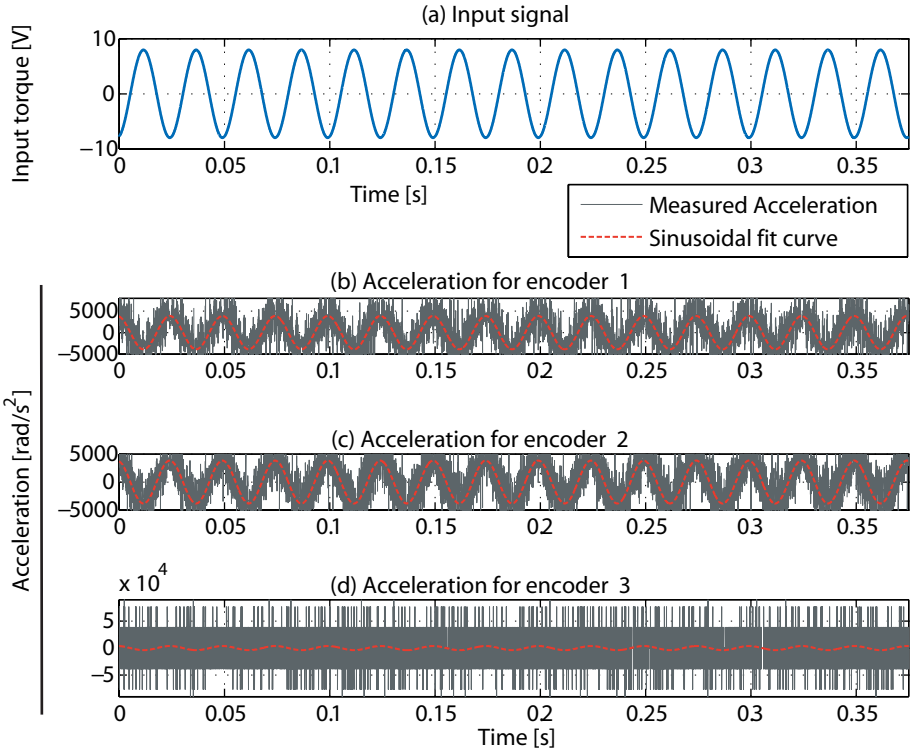

Figure 3.12: Acceleration measurement at 40 Hz.

The two bearings supporting the ball screw were modeled by applying appropriate boundary conditions on the ball screw. For the axially fixed end, all degrees of freedom except for rotation around the x-axis (i.e. main ball screw axis) were fixed. For the axially free end, the y-axis and z-axis displacements were fixed. The inertia contribution of the bearings was modeled by two rings attached to the ball screw at the bearing locations. Details of the ball screw, coupling, motor, and bearing ring geometries have been reported in Appendix C, along with the inertia and stiffness parameters of the model components.

The effect of table inertia was modeled as a disc element at the nut position, which accounts for partial mass of the table. Due to the hysteresis-type motion loss in the preloaded nut [11], very small motions of the ball screw do not fully transfer to the table and vice-versa. Thorough modeling of the nut dynamics is quite complex, and although there have been successful works reported in the literature [11][49][68][71], this task has been kept outside the scope of this thesis. In general, the nut dynamics is more significant at small motion range around velocity crossings due to stick-slip

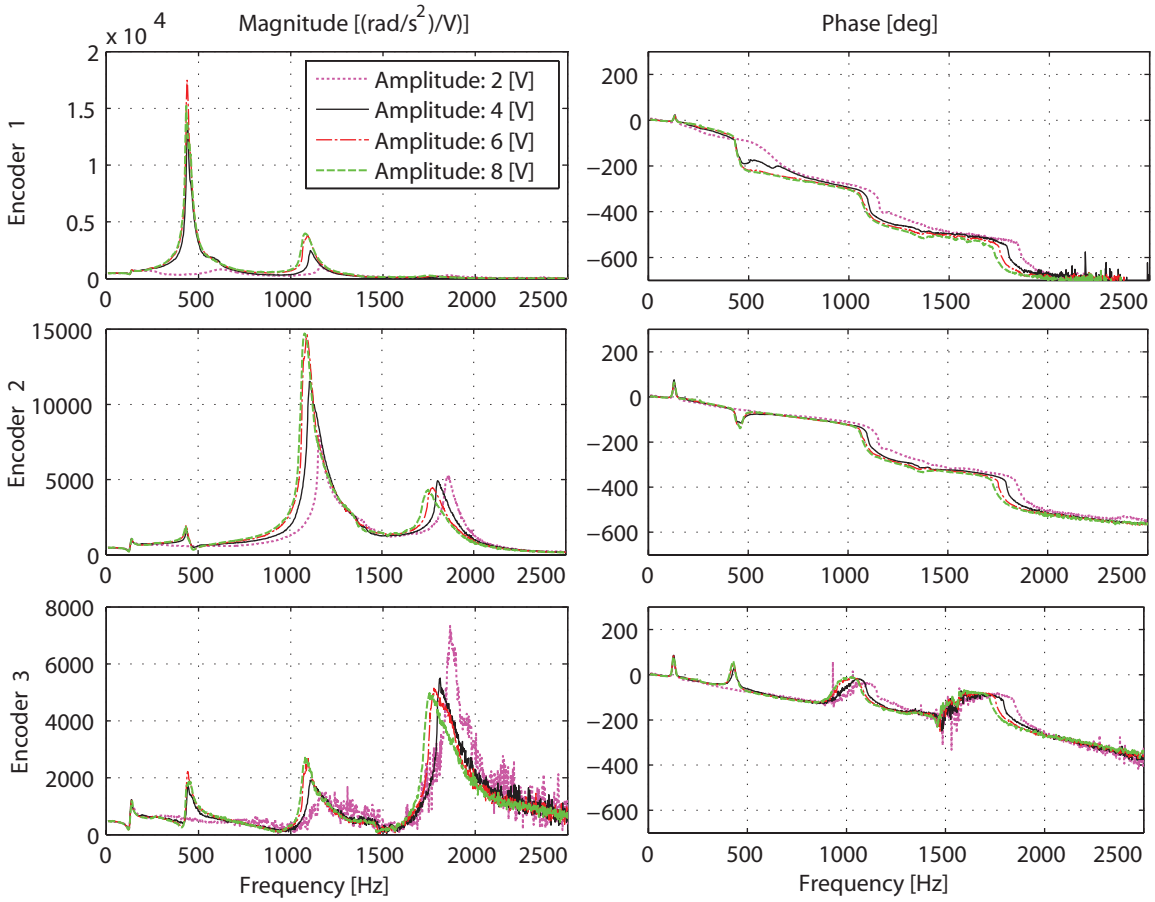

Figure 3.13: Torsional FRF with different amplitudes of input signal and the table at the middle position. Measurement from: (a) Encoder 1, (b) Encoder 2, (c) Encoder 3.

friction, and is less significant at high speeds. Here, the equivalent inertia reflected from the linear motion of the table and nut was determined experimentally, in order to yield consistent modal frequencies with measured Frequency Response Functions (FRF's). By trial and error, it was found that using an inertia element which accounts for 8.5% of the table's inertia was successful in predicting the observed torsional frequencies. All other parameters in the Finite Element model were either determined analytically, or substituted from catalogue values. The disk representing the table equivalent inertia was connected to the ball screw by a torsional spring, representing the stiffness of the preloaded nut. This torsional stiffness (15.10×10^3 Nm/rad) was calculated from the axial stiffness value (137×10^6 N/m) provided in the ball screw catalogue. Details of this calculation are presented in Appendix C.

The first three torsional modes are shown in Figure 3.9, with the corresponding natural frequencies of 451, 1166, and 1752 Hz. In the 1st torsional mode of vibration, the neutral position is near the motor end of the ball screw. The torsional displacement gradually increases from right to left along the ball screw and the maximum deflection happens at the free end. The motor has a negative

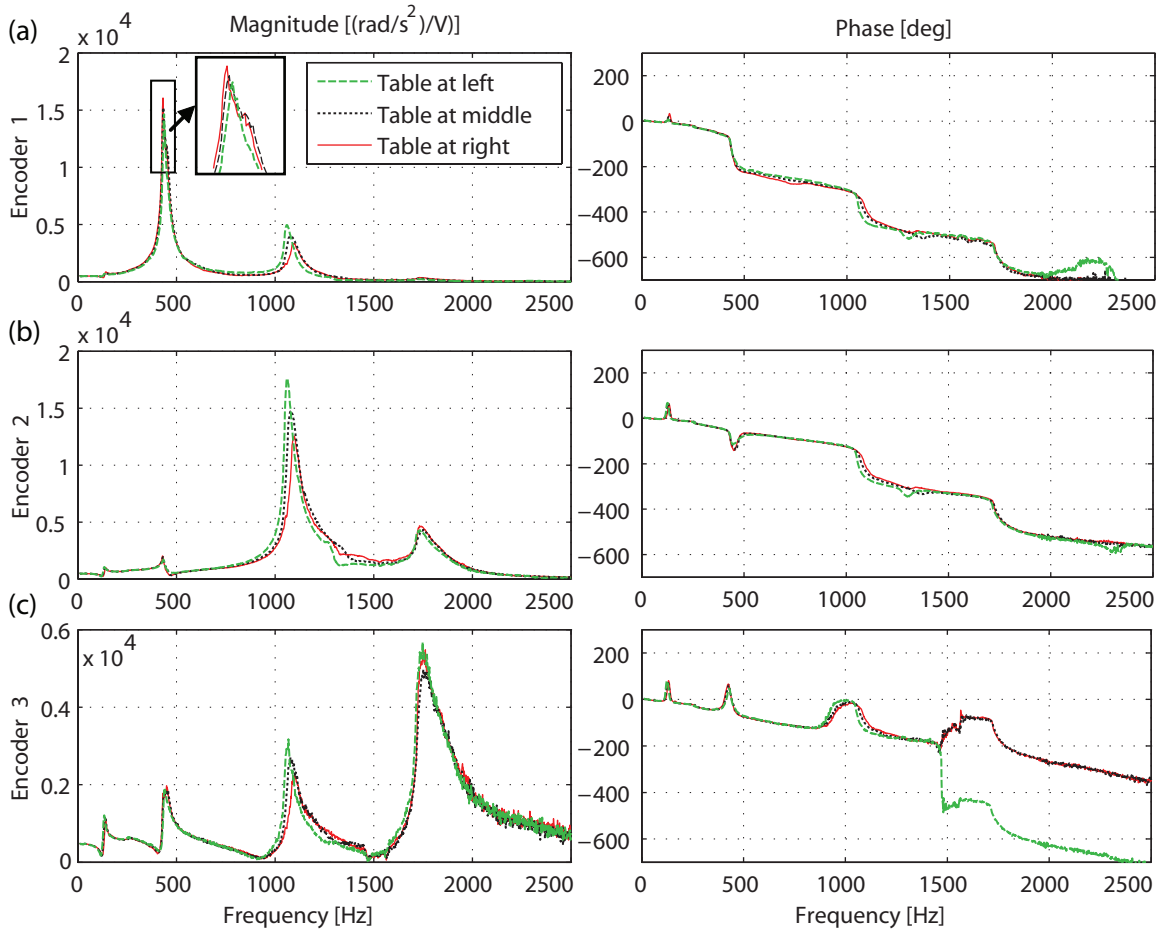

Figure 3.14: Torsional FRF with different table position. Measurement from: (a) Encoder 1, (b) Encoder 2, (c) Encoder 3.

displacement in this mode. In the 2nd torsional mode, there are two neutral positions, one near the motor and the other between the table location and the free end. The peak occurs near the position of Encoder 2. In the 3rd torsional mode, two neutral positions occur between the table and Encoders 1 and 2. A positive peak occurs at the table location, and negative peaks occur at both ends of the ball screw.

The torsional vibrations were verified in frequency response tests, where a sinusoidal testing signal was applied to the amplifier input and rotational displacements were measured from Encoders 1, 2, and 3, as shown in Figure 3.11. The displacement measurements were double differentiated to obtain acceleration profiles, which were used in magnitude and phase evaluation with respect to the excitation signal. A sample result, evaluated at 40 Hz excitation frequency, is shown in Figure 3.12. As can be seen, the acceleration signal estimated from of Encoders 1 and 2 are less noisy compared to the signal obtained from Encoder 3 (motor encoder), due to the higher resolution of the first two encoders. However, with averaging in the Least Squares technique used to fit the sinusoidal curves to

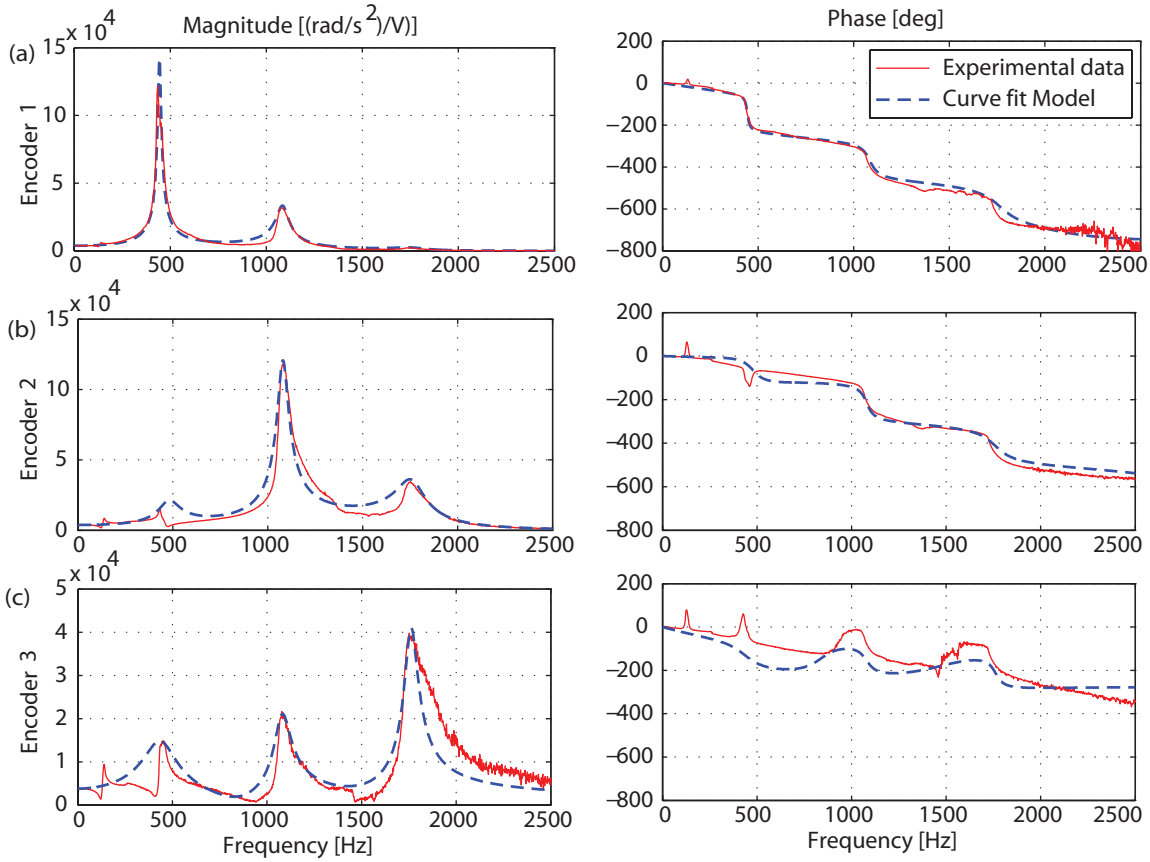

Figure 3.15: Experimental and curve-fit torsional FRFs for: (a) Encoder 1, (b) Encoder 2, (c) Encoder 3.

the signals, reasonably accurate estimations of vibration amplitude and phase are obtained, as seen in the FRF measurements shown in Figure 3.13 and Figure 3.14. These measurements contain the dynamics of the ball screw mechanism, as well as the amplifier and the motor.

The tests were performed for frequencies ranging from 10 to 2500 Hz with an increment of 2 Hz. To investigate amplitude and position dependency, different amplitudes of input and axial positions of the table were examined. The middle position is where the table is in the middle of its stroke length and the nut is 520 mm to right of the free end. The left and right positions are where the table is displaced by 150 mm to the left and right sides, in the mentioned order.

The measured torsional FRF's for four different amplitudes of the excitation, with the table positioned at the middle of its stroke, are shown in Figure 3.13. Figure 3.13(a), (b), and (c) correspond to measurement from Encoders 1, 2, and 3, respectively. The predicted torsional resonances are observed in the experimental results. Comparing the cases with different excitation amplitudes, where 10 V corresponds to the full rated torque of 9.8 Nm in to the motor catalogue, the cases with sufficient amplitude, starting with 4 V, resulted in consistent torsional FRF's as shown in

Table 3.4: Poles, zeros, and gain of 6th order torsional FRF observed by Encoder 1.

T.F. observed by Encoder 1			
Order K	**Poles $p_{k,1}$ rad/sec**	**Frequency ω Hz**	**Damping ratio (%)**
1	-526 + 11091i	1767.1	4.74
2	-526 - 11091i	1767.1	4.74
3	-205 + 6820i	1086	3
4	-205 - 6820i	1086	3
5	-56 + 2789i	444	2
6	-56 - 2789i	444	2
Order K	**Zero $Z_{k,1}$ rad/sec**	**Frequency ω Hz**	**Damping ratio (%)**
1	-7194 + 17114i	2954.7	38.75
2	-7194 – 17114i	2954.7	38.75
3	2273 + 12422i	2009.8	-18
4	2273 – 12422i	2009.8	-18
5	5655	900	-100
6	5655	900	-100
Transfer function gain $K_{en,1}$ A/V			3800

Figure 3.13. In the case with 2 V of input, the excitation amplitude is insufficient as the magnitude of the resonance peaks appear significantly attenuated, due to the nonlinear friction damping which becomes more dominant than the excitation being delivered by the motor. These measurements indicate reasonably linear and amplitude-independent behavior starting at 4 V of input.

The first torsional resonance occurs at 445 Hz and is mainly observed by Encoder 1, where vibration amplitude is maximum. The amplitudes observed at Encoders 2 and 3 are smaller, which is in agreement with the 1st mode shape shown in Figure 3.9. The second resonance occurs at 1080 Hz which is observed by all encoders. Encoder 2 is subject to the highest magnitude of vibration, which can be explained with the 2nd mode shape. The 3rd resonance is observed at 1755 Hz. Overall, it can be said that the torsional mode shapes obtained from FE analysis are in close agreement with the experimentally measured FRF's.

The accuracy of the measured data degenerates after 2500 Hz. This limitation is mainly due to the encoder resolution. Also, the bandwidth of the current loop is only 480 Hz, which results in lower

Table 3.5: Poles, zeros, and gain of 6th order torsional FRF observed by Encoder 2.

T.F. observed by Encoder 2			
Order K	**Poles $p_{k,2}$ rad/sec**	**Frequency ω Hz**	**Damping ratio (%)**
1	-476 + 11057i	1761.4	4.3
2	-476 - 11057i	1761.4	4.3
3	-183 + 6783i	1080	2.7
4	-183 - 6783i	1080	2.7
5	-350 + 3010i	482.3	11.56
6	-350 - 3010i	482.3	11.56
Order K	**Zero $Z_{k,2}$ rad/sec**	**Frequency ω Hz**	**Damping ratio (%)**
1	2854 + 18252i	2940.2	-15.45
2	2854 – 18252i	2940.2	-15.45
3	6786 + 3287i	1200	-90
4	6786 – 3287i	1200	-90
5	-1856 + 3167i	584.3	50.57
6	-1856 – 3167i	584.3	50.57
Transfer function gain $K_{en,2}$ A/V			3800

excitation at high frequencies. Another limitation is the sampling rate, which was set to 20 kHz for the FRF measurements. In high frequency measurements, the sinusoidal acceleration signal accommodates very few data points, which degrades the accuracy of the fit sinusoidal curves and consequently the FRF measurements. Nevertheless, the most significant torsional dynamics were successfully captured with the presented FRF measurement scheme.

A small peak is observed at about 140 Hz in the torsional frequency responses, which does not correspond to any torsional modes predicted in FEA. This frequency is close to the frequency of the 1st axial vibration resonance (169 Hz), which is predicted based on the table inertia and ball screw, nut, and bearing axial stiffness values, as detailed in Section 3.4.2. Since the ball screw is back drivable, traces of this axial mode are also reflected on the observed torsional FRF's. Further investigation of the axial vibrations, using a linear encoder, has verified this observation by demonstrating the 1st axial mode to be at around 132 Hz, as shown in Figure 3.16.

Table 3.6: Poles, zeros, and gain of 6th order torsional FRF observed by Encoder 3.

T.F. observed by Encoder 3			
Order K	**Poles $p_{k,3}$ rad/sec**	**Frequency ω Hz**	**Damping ratio (%)**
1	-221 + 11065i	1761.4	2
2	-221 - 11065i	1761.4	2
3	-271 + 6780i	1080	4
4	-271 - 6780i	1080	4
5	-559 + 2740i	445	20
6	-559 - 2740i	445	20
Order K	**Zero $Z_{k,3}$ rad/sec**	**Frequency ω Hz**	**Damping ratio (%)**
1	182870	29105	-100
2	-1410 + 9320i	1500	15
3	-1410 – 9320i	1500	15
4	-530 + 5270i	842	10
5	-530 - 5270i	842	10
6	1870	297	-100
Transfer function gain $K_{en,3}$ A/V			3800

The variation in torsional FRF's for different table position is investigated in Figure 3.14. An excitation amplitude of 8 V (corresponding to 7.84 Nm in steady-state) was used to obtain these measurements. As seen in Figure 3.14, the torsional FRF's are almost independent of the table position, except for some minor variations. When the table is at the left position, closer to the free end of the ball screw, Encoder 1 measures a lower peak for the first resonance compared to the cases where the table is at the middle or right, as shown in Figure 3.14(a). The peak of the 1st torsional mode occurs close to the position of Encoder 1, as seen in Figure 3.9. Hence, it is believed that moving the table towards Encoder 1 attenuates the 1st resonance by adding additional damping from the friction in the pre-loaded nut. A similar behavior is also observed for the attenuation of the peak of the second torsional resonance when the table is at the right position, i.e. close to the axial position of the 2nd resonance, as seen in Figure 3.14(b). Apart from these minor observations, the axial location of the table has no significant effect on the torsional modes of the ball screw drive.

To get an approximate idea of the pole and zero locations in the observed responses, transfer functions were fit to the experimental data obtained with 8 V of excitation and with the table in the middle position. A 6th order model, as in Eq. (3.10), was curve fit to the measured frequency responses, using the Complex Curve Fitting method [40]. The experimental and curve-fit FRF's are shown in Figure 3.15.

$$G_{en-i}(s) = K_{en-i}\frac{\prod_{k=1}^{6}(s - z_{k-i})}{\prod_{k=1}^{6}(s - p_{k-i})} \quad , \quad \text{where}: \ i: \text{Encoder number} \tag{3.10}$$

The poles, zeros, frequencies, and gains of the curve-fit transfer functions (from the amplifier input to ball screw angular acceleration, measured with different encoders) are presented in Table 3.4, Table 3.5, and Table 3.6. The curve-fit transfer function is reasonably successful in replicating the FRF measurement from Encoder 1. It is interesting to note that the pole locations and damping ratios are generally estimated with reasonable consistency between the three transfer functions, as would be expected for measurements taken from the same dynamic system. However, there are noticeable discrepancies between the analytical models and experimental measurements obtained from Encoders 2 and 3. This suggests that better modal parameter identification techniques could be employed, if the identified models were directly to be used in controller design. In this thesis, the curve-fit transfer functions are only used to aid in the tuning of notch filters, which are designed to attenuate the ball screw's structural vibrations.

3.4.2 Modeling and Measurement of the First Axial Mode

The first axial mode has a major influence on the final linear positioning accuracy, as well as the achievable control bandwidth. This mode is generated due to interaction between the inertia of the translating components, such as the table and nut, and the axial flexibility of the drive, resulting from the nut, ball screw, and the axially fixed bearing. Accurate modeling and identification and of this mode is a crucial step in designing high performance controllers that can overcome the bandwidth limitation posed by this mode.

The natural frequency of this mode was predicted using the catalogue rated stiffness values for the fixed axial bearing ($K_{fb} = 113\times10^6$ N/m) and the ball nut ($K_{nut} = 137\times10^6$ N/m). The ball screw axial stiffness was calculated assuming a cylindrical geometry as follows:

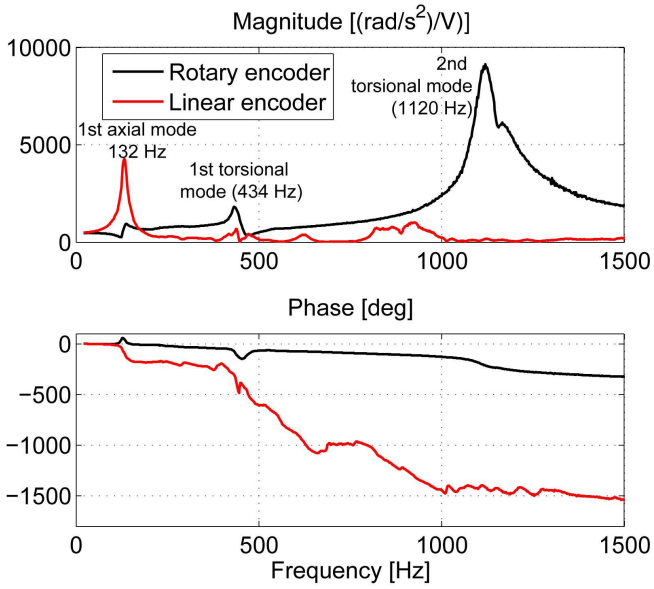

Figure 3.16: Axial and Torsional FRF (Rotary encoder refers to Encoder 2).

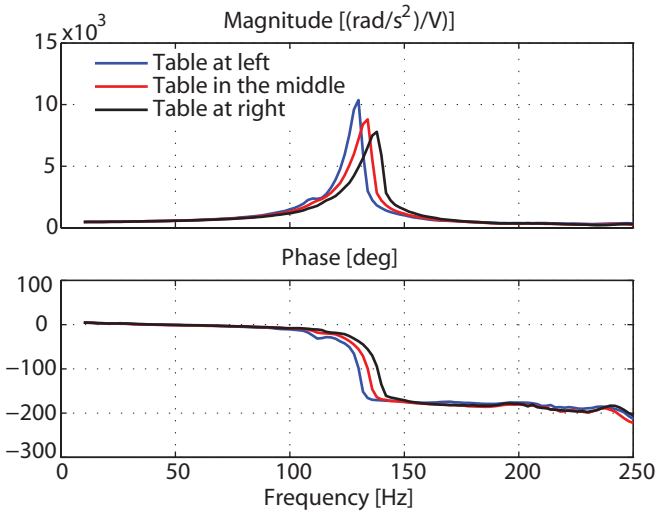

Figure 3.17: Axial vibration FRFs at different table locations.

$$K_{bs} = \frac{EA}{l_a} \tag{3.11}$$

Above, $E = 210\times10^9$ N/m^2, is Young's elasticity modulus for steel, A is the ball screw equivalent cross section (~2.545×10^{-4} m^2), and l_a is the ball screw approximate active length (~0.55 m from the fixed bearing location to the table at middle position). The ball screw stiffness is calculated to be 97.2×10^6 N/m. Consequently, the equivalent axial stiffness of the drive can be calculated by considering the three stiffness values as a combination of springs connected in series:

$$\frac{1}{K_{eq}} = \frac{1}{K_{bs}} + \frac{1}{K_{fb}} + \frac{1}{K_{nut}} \tag{3.12}$$

where $K_{eq} = 37.8 \times 10^6$ N/m. The natural frequency of the 1st axial mode can then be obtained as:

$$\omega_{axial} = \sqrt{\frac{K_{eq}}{m_t}} = \sqrt{\frac{37.8 \times 10^6}{33.474}} = 1.0629 \times 10^3 \text{ rad/sec (or 169 Hz)} \tag{3.13}$$

This frequency is verified by the axial frequency response measured by the linear encoder instrumented on the table. The frequency response shown in Figure 3.16 shows this mode at 132 Hz, and the measurements were taken when the table was in the middle of the stroke length. At a later stage of the research, more frequency response measurements were collected to investigate variation of this mode's dynamics with axis position, as seen in Figure 3.17. The frequency of this mode shifts roughly by ± 4 Hz, at the extreme left/right table positions (± 175 mm from the middle position). The amplitude of the peak changes by a maximum of 18%. The amplitude of the 1st axial mode was generally larger at the time of these measurements due to injection of hardening material (Moglice®) into air bushings to achieve higher mechanical stiffness. Later, this mode will be modeled as part of axis dynamics, in order to design an Adaptive Sliding Mode Controller that actively dampens out the axial vibrations.

3.5 Conclusions

This chapter has presented the development of a basic model for analysis and control of a ball screw drive. It has focused on modeling the rigid body motion, friction characteristics, as well as torsional and axial modes. Rigid body dynamics was identified using Least Squares parameter estimation, particularly for the total inertia. Nonlinear friction characteristics were identified through disturbance observation using a Kalman filter. The amplifier dynamics were identified and a current loop bandwidth of 480 Hz was measured through frequency response tests. The torsional and axial modes were modeled using finite element analysis and validated in frequency response measurements, indicating the first axial mode to be at 132 Hz, and the first three torsional modes at 445, 1080, 1755 Hz, respectively. In the proceeding chapters, this model will be developed further to accommodate the effects of torque ripples, lead errors, and elastic deformations, which will also be considered in the controller design.

Chapter 4
Adaptive Sliding Mode Controller Design

4.1 Introduction

This chapter presents the general framework for Adaptive Sliding Mode Control (ASMC), which is the principal design technique used in this thesis. ASMC was chosen for its excellent tracking and robustness features, which are facilitated through the inherent feedforward control and disturbance rejection characteristics that are realized during the synthesis of the control law. Section 4.2 presents the general design methodology. Section 4.3 details the ASMC design based on only rigid body dynamics of the drive. To attenuate the structural vibrations, notch filters are developed in Section 4.4, which significantly limit the excitation of the torsional and axial modes. Feedforward friction compensation is incorporated into the controller in Section 4.5. High speed tracking tests are performed in Section 4.6 in order to verify the performance of the developed controllers. The conclusions of this chapter are presented in Section 4.8.

4.2 General Formulation of Adaptive Sliding Mode Control (ASMC)

Utkin [67] pioneered the idea of using sliding surfaces for control, which was based on discontinuous switching of the control signal in order to keep the system states on a sliding surface. The sliding surface is defined by a stable linear differential equation, as seen in Figure 4.1. As long as the states can be kept on this surface, they eventually converge to (i.e. slide towards) the origin. The characteristic of the response is dictated by the parameters that define the sliding surface. Slotine and Li [60] refined this methodology by developing a general and adaptive framework, which resulted in a continuous and nonlinear control law with Lyapunov-guaranteed stability. Later Zhu et al. [75] provided the stability proof for conducting the parameter adaption within known bounds. In the following, the design methodology established in [60] and [75] is briefly reviewed.

The plant (i.e. system to be controlled) is assumed to be in the state-space form as,

$$\dot{\boldsymbol{x}} = \boldsymbol{A}\boldsymbol{x} + \boldsymbol{B}\boldsymbol{u} + \boldsymbol{d} \tag{4.1}$$

Above, $\boldsymbol{x} \in \Re^n$ is the state vector, $\boldsymbol{u} \in \Re^m$ is the control input, $\boldsymbol{A}$ is the state transition matrix, $\boldsymbol{B}$ is the input matrix and $\boldsymbol{d}$ is the disturbance vector. A sliding surface $\boldsymbol{\sigma} \in \Re^m$ can be defined in the form:

$$\boldsymbol{\sigma} = \boldsymbol{S}(\boldsymbol{x}_{ref} - \boldsymbol{x}) \tag{4.2}$$

where $\boldsymbol{x}_{ref}$ is the reference state vector, $\boldsymbol{x}$ is the system state vector, and $\boldsymbol{S}$ (the parameters of sliding surface) is chosen such that $\boldsymbol{x} \to \boldsymbol{x}_{ref}$ when $\boldsymbol{\sigma} = 0$. Also, the matrix product $\boldsymbol{SB}$ is assumed to be positive definite and symmetrical. The time derivative of $\boldsymbol{\sigma}$ can be expressed combining Eq. (4.1) and (4.2) as follows:

$$\dot{\boldsymbol{\sigma}} = \boldsymbol{S}(\dot{\boldsymbol{x}}_{ref} - \boldsymbol{Ax} - \boldsymbol{d}) - \boldsymbol{SBu} \tag{4.3}$$

It is assumed that $(\boldsymbol{SB})^{-1}(\dot{\boldsymbol{x}}_{ref} - \boldsymbol{Ax} - \boldsymbol{d})$ can be expressed as a linear combination of r parameters ($\boldsymbol{P} = [p_1, p_2, \ldots, p_r]^T$) and corresponding regressors ($\boldsymbol{Y} = [y_1, y_2, \ldots, y_r]$) in the form:

$$(\boldsymbol{SB})^{-1}\boldsymbol{S}(\dot{\boldsymbol{x}}_{ref} - \boldsymbol{Ax} - \boldsymbol{d}) = \boldsymbol{Y}(\dot{\boldsymbol{x}}_{ref}, \boldsymbol{x}) \cdot \boldsymbol{P} \tag{4.4}$$

Furthermore, it is assumed that each parameter which represents the drive dynamics lies within pre-known lower and upper bounds, i.e. $p_k \in [p_k^-, p_k^+]$. The following parameter adaptation rule is used:

$$\dot{\hat{\boldsymbol{P}}} = \Gamma^{-1}\boldsymbol{K}\boldsymbol{Y}^T\boldsymbol{\sigma} \tag{4.5}$$

where $\hat{\boldsymbol{P}}$ is the vector of estimated values for the system parameters. The true parameters are represented with vector $\boldsymbol{P}$. $\Gamma^{-1} = diag(\rho_1, ..., \rho_r)$ is a diagonal matrix consisting of positive adaptation gains ($\rho_k \geq 0$) which can be tuned for fast and stable convergence of the parameters. $\boldsymbol{K} = diag(\kappa_1, ..., \kappa_r)$ is a matrix of adaptation bound factors, where individual entries (κ_k) assume binary ("0" or "1") values to switch the adaptation on and off, in order to ensure that all estimated parameters (p_k) lie within their pre-known bounds (i.e. $\hat{p}_k \in [p_k^-, p_k^+]$). κ_k is defined as:

$$k_k = \begin{cases} 0 & if \quad \hat{p}_k \leq p_k^- \quad and \quad \varphi_k \leq 0 \\ 0 & if \quad \hat{p}_k \geq p_k^+ \quad and \quad \varphi_k \geq 0 \\ 1 & , \qquad\qquad otherwise \end{cases} \tag{4.6}$$

In the above expression, $\varphi = [\varphi_1, \ldots, \varphi_r]^T = \boldsymbol{Y}^T\boldsymbol{\sigma}$. Following this definition, it can be verified that the term $(\boldsymbol{P} - \hat{\boldsymbol{P}})^T(\boldsymbol{Y}^T\boldsymbol{\sigma} - \Gamma\dot{\hat{\boldsymbol{P}}})$ will always be negative semi-definite, because both the actual and estimated parameters are within known bounds, i.e. $p_k \in [p_k^-, p_k^+]$ and $\hat{p}_k \in [p_k^-, p_k^+]$. This feature will later be used in the stability proof, when applying Lyapunov's technique. Hence,

$$(\boldsymbol{P}-\hat{\boldsymbol{P}})^T(\boldsymbol{Y}^T\boldsymbol{\sigma}-\Gamma\dot{\hat{\boldsymbol{P}}})=\sum_{k=1}^{r}[(p_k-\hat{p}_k)\varphi_k(1-\kappa_k)]\le 0 \tag{4.7}$$

For stable control law design, a Lyapunov function is formulated in the form:

$$V=\frac{1}{2}[\boldsymbol{\sigma}^T(\boldsymbol{SB})^{-1}\boldsymbol{\sigma}+(\boldsymbol{P}-\hat{\boldsymbol{P}})^T\Gamma(\boldsymbol{P}-\hat{\boldsymbol{P}})] \tag{4.8}$$

Assuming that the true parameters do not change over time ($\dot{\boldsymbol{P}}=\boldsymbol{0}$), taking the time derivative of V and substituting the expression for $\dot{\boldsymbol{\sigma}}$ from Eq. (4.3) results in:

$$\begin{aligned}\dot{V}&=\frac{1}{2}[\dot{\boldsymbol{\sigma}}^T(\boldsymbol{SB})^{-1}\boldsymbol{\sigma}+\boldsymbol{\sigma}^T(\boldsymbol{SB})^{-1}\dot{\boldsymbol{\sigma}}+(\dot{\boldsymbol{P}}-\dot{\hat{\boldsymbol{P}}})^T\Gamma(\boldsymbol{P}-\hat{\boldsymbol{P}})+(\boldsymbol{P}-\hat{\boldsymbol{P}})^T\Gamma(\dot{\boldsymbol{P}}-\dot{\hat{\boldsymbol{P}}})]\\&=\boldsymbol{\sigma}^T(\boldsymbol{SB})^{-1}\boldsymbol{S}(\dot{\boldsymbol{x}}_{ref}-\boldsymbol{Ax}-\boldsymbol{d})-\boldsymbol{\sigma}^T\boldsymbol{u}-(\boldsymbol{P}-\hat{\boldsymbol{P}})^T\Gamma\dot{\hat{\boldsymbol{P}}}\end{aligned} \tag{4.9}$$

Substituting $(\boldsymbol{SB})^{-1}(\dot{\boldsymbol{x}}_{ref}-\boldsymbol{Ax}-\boldsymbol{d})$ with $\boldsymbol{Y}(\dot{\boldsymbol{x}}_{ref},\boldsymbol{x})\boldsymbol{P}$ from Eq. (4.4),

$$\dot{V}=\boldsymbol{\sigma}^T\boldsymbol{YP}-\boldsymbol{\sigma}^T\boldsymbol{u}-(\boldsymbol{P}-\hat{\boldsymbol{P}})^T\Gamma\dot{\hat{\boldsymbol{P}}} \tag{4.10}$$

By adding and subtracting $\boldsymbol{\sigma}^T\boldsymbol{Y}\hat{\boldsymbol{P}}$, $\dot{V}$ becomes:

$$\dot{V}=-\boldsymbol{\sigma}^T\boldsymbol{u}+(\boldsymbol{P}-\hat{\boldsymbol{P}})^T(\boldsymbol{Y}^T\boldsymbol{\sigma}-\Gamma\dot{\hat{\boldsymbol{P}}})+\boldsymbol{\sigma}^T\boldsymbol{Y}\hat{\boldsymbol{P}} \tag{4.11}$$

According to Eq. (4.7), $(\boldsymbol{P}-\hat{\boldsymbol{P}})^T(\boldsymbol{Y}^T\boldsymbol{\sigma}-\Gamma\dot{\hat{\boldsymbol{P}}})\le 0$. Hence, in order to ensure stability, $\dot{V}$ has to be made negative definite. This can be accomplished by equating the $-\boldsymbol{\sigma}^T\boldsymbol{u}+\boldsymbol{\sigma}^T\boldsymbol{Y}\hat{\boldsymbol{P}}$ term to a negative definite quantity, such as $-\boldsymbol{\sigma}^T\boldsymbol{K}_s\boldsymbol{\sigma}$. Here $\boldsymbol{K}_s\in\Re^{m\times m}$ and $\boldsymbol{K}_s>0$. Hence,

$$-\boldsymbol{\sigma}^T\boldsymbol{u}+\boldsymbol{\sigma}^T\boldsymbol{Y}\hat{\boldsymbol{P}}=-\boldsymbol{\sigma}^T\boldsymbol{K}_s\boldsymbol{\sigma} \tag{4.12}$$

This results in the ASMC control law:

$$\boldsymbol{u}=\boldsymbol{K}_s\boldsymbol{\sigma}+\boldsymbol{Y}(\dot{\boldsymbol{x}}_{ref},\boldsymbol{x})\hat{\boldsymbol{P}} \tag{4.13}$$

As can be observed from the above expression, there is no discontinuous switching of the control signal. This distinguishes this controller design from the switching-based sliding mode controller, which was developed by Utkin [67]. This method is more favorable for implementation on real physical systems, as high frequency switching of the actuation force/torque could be highly detrimental for the motors and mechanical components. The design choices for this controller are the sliding surface definition $\boldsymbol{\sigma}=\boldsymbol{S}(\boldsymbol{x}_{ref}-\boldsymbol{x})$, the feedback gain $\boldsymbol{K}_s$, adaptation gains Γ^{-1}. Proof of $\dot{V}$

being negative definite ensures asymptotic convergence of state regulation errors onto the sliding, where they eventually converge to zero. However, the parameters are not guaranteed to converge unless the control signal delivers sufficiently persistent excitation to the plant [55]. This may be tricky to realize on precision motion control systems, where the commanded trajectories are typically smooth up to acceleration or jerk level, and sudden changes or high frequency content in the control signal are not desirable.

4.3 ASMC Design for Rigid Body Dynamics

In this section, the ASMC design is adapted to control the rigid body dynamics of the ball screw drive. This control law has been used as the foundation in several compensation schemes, for torque ripples and elastic deformations etc., that are developed in later chapter of this thesis. In Chapter 6, the ASMC is also designed to explicitly consider the axial vibrations of the ball screw as part of the plant dynamics. It is interesting to note that when only rigid body dynamics are considered, the ASMC law takes the form of a PID controller with feedforward velocity and acceleration compensation terms, which makes this control law highly suitable for practical implementation on commercially available motion control hardware.

The rigid body dynamics of the drive in Eq. (3.6) can be simplified as:

$$\theta(s) = \frac{1}{s(ms+b)}[u(s) - d(s)] \tag{4.14}$$

Above, θ [rad] is the ball screw angular position, u is the control input, d represents the equivalent external disturbance, $m = J / K_a K_t$ [V/(rad/sec^2)], and $b = B / K_a K_t$ [V/(rad/sec)] are the control-signal normalized inertia and viscous damping terms. The above model can be expressed in state space form as:

$$\begin{bmatrix} \dot{\theta}(t) \\ \ddot{\theta}(t) \end{bmatrix} = \begin{bmatrix} 0 & 1 \\ 0 & -b/m \end{bmatrix} \begin{bmatrix} \theta(t) \\ \dot{\theta}(t) \end{bmatrix} + \begin{bmatrix} 0 \\ 1/m \end{bmatrix} u(t) - \begin{bmatrix} 0 \\ 1/m \end{bmatrix} d(t) \tag{4.15}$$

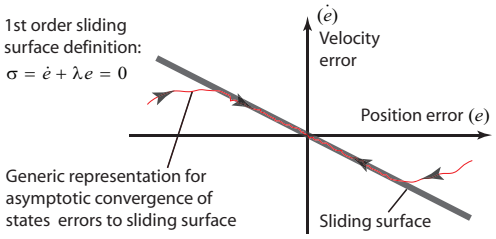

Figure 4.1: 1st order linear sliding surface.

Using the estimated inertia (J = 2.1×10^{-3} kgm^2) and viscous damping (B = 1.015×10^{-3} kgm^2/sec), and the catalogue values for amplifier gain (K_a = 1.7193 A/V) and motor torque constant (K_t = 0.57 Nm/A), the equivalent inertia and viscous damping can be respectively calculated as $m = J / K_a K_t$ = 2.1429×10^{-3} V/(rad/sec^2) and $b = B / K_a K_t$ = 1.0357 V/(rad/sec). As the model is second order, and there is only one control input, the sliding surface is chosen to be first order as follows

$$\sigma = (\dot{\theta}_{ref} - \dot{\theta}) + \lambda(\theta_{ref} - \theta) = \underbrace{[\lambda \quad 1]}_{\boldsymbol{S}} \cdot \left(\begin{bmatrix} \theta_{ref} \\ \dot{\theta}_{ref} \end{bmatrix} - \begin{bmatrix} \theta \\ \dot{\theta} \end{bmatrix} \right) = \boldsymbol{S}(\boldsymbol{x}_{ref} - \boldsymbol{x}) = 0 \tag{4.16}$$

Considering that the sliding surface represents a desired model with first order dynamics, the pole frequency $\lambda > 0$ represents the desired control bandwidth. Choosing the plant parameters to be m, b, and d, a regressor-parameter expression similar to the one in Eq. (4.4) can be constructed as follows:

$$\begin{aligned} (\boldsymbol{SB})^{-1}\boldsymbol{S}(\dot{\boldsymbol{x}}_{ref} - \boldsymbol{Ax} - \boldsymbol{Bd}) &= \left([\lambda \; 1] \begin{bmatrix} 0 \\ 1/m \end{bmatrix} \right)^{-1} \cdot [\lambda \; 1] \cdot \left(\begin{bmatrix} \dot{\theta}_{ref} \\ \ddot{\theta}_{ref} \end{bmatrix} - \begin{bmatrix} 0 & 1 \\ 0 & -b/m \end{bmatrix} \begin{bmatrix} \theta \\ \dot{\theta} \end{bmatrix} - \begin{bmatrix} 0 \\ 1/m \end{bmatrix} [d] \right) \\ &= \begin{bmatrix} \ddot{\theta}_{ref} + \lambda(\dot{\theta}_{ref} - \dot{\theta}) & \dot{\theta} & 1 \end{bmatrix} \cdot \begin{bmatrix} m \\ b \\ d \end{bmatrix} \end{aligned} \tag{4.17}$$

Above, $\boldsymbol{P} = [p_1, p_2, p_3]^T = [m, b, d]^T$ is the parameter vector and $\boldsymbol{Y}(\dot{\boldsymbol{x}}_{ref}, \boldsymbol{x}) = [y_1, y_2, y_3]$ $= [\ddot{\theta}_{ref} + \lambda(\dot{\theta}_{ref} - \dot{\theta}), \dot{\theta}, 1]$ is the corresponding regressor vector. Correspondingly, $\hat{\boldsymbol{P}} = [\hat{m}, \hat{b}, \hat{d}]^T$ represents the set of parameter estimates. Substituting the expressions for σ, $\boldsymbol{Y}$, and $\hat{\boldsymbol{P}}$ into the general control law, derived in Eq. (4.13), yields the following expression for ASMC designed based on rigid body dynamics.

$$u_{smc} = K_s \sigma + \boldsymbol{Y}(\dot{\theta}_{ref}, \theta) \cdot \hat{\boldsymbol{P}} = K_s \sigma + \hat{m}[\ddot{\theta}_{ref} + \lambda(\dot{\theta}_{ref} - \dot{\theta})] + \hat{b}\dot{\theta} + \hat{d} \tag{4.18}$$

It is important to note that in precision motion control systems, the position trajectory is usually very smooth (at least C^2 continuous) and does not include a sufficient amount of excitation to estimate several parameters simultaneously [19]. Therefore, only the external disturbance estimate $\hat{d}$ is chosen as the online adapted parameter. The mass and viscous friction estimates ($\hat{m}$ and $\hat{b}$) are substituted from their nominal values obtained through parameter identification, as explained in Chapter 3. It is interesting to note that adapting for the external disturbance d also provides

robustness against variations in the drive dynamics up to a certain frequency, thereby accounting for the mismatch between actual and estimated inertia and viscous damping values.

Using the general parameter adaptation law given in Eq. (4.5)-(4.6), and assuming that the true external disturbance lies within known bounds: $d \in [d^-, d^+]$, the disturbance adaptation law assumes the following expression:

$$\dot{\hat{d}} = \rho\kappa\sigma = \rho\kappa[(\dot{\theta}_{ref} - \dot{\theta}) + \lambda(\theta_{ref} - \theta)] \quad , \quad \text{where}: \ \kappa = \begin{cases} 0 \ , \ if \ \hat{d} \le d^- \ \text{ and } \ \sigma \le 0 \\ 0 \ , \ if \ \hat{d} \ge d^+ \ \text{ and } \ \sigma \ge 0 \\ 1 \ , \ \text{otherwise} \end{cases} \tag{4.19}$$

If the disturbance adaptation bound κ is omitted from the equations, the ASMC law assumes the form of a PID controller with acceleration and velocity feedforward terms as shown in the following,

$$u_{smc} = \underbrace{K_{acc}\ddot{\theta}_{ref} + K_{vel}\dot{\theta}_{ref}}_{\substack{\text{Acceleration and Velocity} \\ \text{Feedforward}}} + \underbrace{K_p(\theta_{ref} - \theta) + K_i\int_0^t(\theta_{ref} - \theta)d\tau + K_d(\dot{\theta}_{ref} - \dot{\theta})}_{\text{Proportional + Integral + Derivative (PID) Control}} \tag{4.20}$$

$$\text{where}: \ K_{acc} = \hat{m}, \ K_{vel} = \hat{b}, \ K_p = K_s\lambda + \rho, \ K_i = \rho\lambda, \ K_d = K_s + \hat{m}\lambda - \hat{b}$$

As stated earlier, this control law will be used when validating a majority of the compensation algorithms developed in this thesis. In the proceeding sections and chapters, the tracking performance of this control law will be augmented with several other compensation techniques, such as notch filtering of the resonances, cancellation of the predictable friction characteristics, as well as the modeling and cancellation of torque ripples, lead errors, and elastic deformations. In addition, the concepts of applying active vibration damping will be explored, by either incorporating a simple cancellation strategy that works together with the rigid body based control law, or by incorporating the vibratory dynamics as part of the plant model when designing the ASMC.

4.4 Notch Filtering of Structural Resonances

The control signal can excite the structural vibrations of the ball screw, in particular the axial and torsional modes, when it has frequency content near their resonances. In order to avoid this, notch filters are designed to flatten out the open loop acceleration FRF's as much as possible. This helps to improve the stability margins and control bandwidth, by attenuating potential sharp resonances in the loop transfer function (i.e. $L = G_{plant}K_{feedback}$) in the vicinity of the crossover frequency (ω_c, where $|L(\omega_c)| \models 1$). Notch filtering has been successfully applied in earlier works as well, such as in

[19][62], to improve the stability margins and achieve further bandwidth increase in machine tool drives. The designed notch filters to attenuate the torsional and axial modes are presented in Sections 4.4.1 and 4.4.2.

4.4.1 Notch Filtering of Torsional Modes

For the first two torsional modes, two sets of notch filters are designed based on the frequency responses registered from Encoders 1 and 2. Each set of filters can be used when closing the position control loop with the corresponding encoder. The discrete-time expression for each notch filter has the form:

$$N(z) = K_n \frac{z^2 + n_1 z + n_2}{z^2 + d_1 z + d_2} \tag{4.21}$$

Above n_1, n_2, d_1, and d_2 are obtained from the tuned poles and zeros. The frequencies and damping ratios of each notch filter are tuned to attenuate the input signal around the resonance frequency and appropriately recover the gain afterwards, while resulting in an overall transfer function as flat as possible. The gain, K_n, is adjusted to yield a steady-state gain of unity. The actual values for n_1, n_2, d_1, d_2, K_n, as well as the corresponding frequency and damping ratios are summarized in Table 4.1. The relationship between the pole frequency and damping ratio (ω_d [rad/sec], ζ_d [ ]) and the

Table 4.1: Torsional notch filter parameters, using T_s = 1/20,000 sec for discretization.

	1st torsional resonance	**2nd torsional resonance**
Encoder 1	$N_{11}(z) = 1.026 \frac{z^2 - 1.999z + 0.999}{z^2 - 1.986z + 0.9719}$	$N_{12}(z) = 0.8624 \frac{z^2 - 1.998z + 0.999}{z^2 - 1.986z + 0.987}$
	Zeros: Frequency: ω_n = 444 [Hz] Damping ratio: ζ_n = 0.035	Zeros: Frequency: ω_n = 1096 [Hz] Damping ratio: ζ_n = 0.015
	Poles: Frequency: ω_d = 453 [Hz] Damping ratio: ζ_d = 1	Poles: Frequency: ω_d = 1021 [Hz] Damping ratio: ζ_d = 0.2
Encoder 2	$N_{21}(z) = 1.032 \frac{z^2 - 1.988z + 0.988}{z^2 - 1.973z + 0.973}$	$N_{22}(z) = 0.8411 \frac{z^2 - 1.997z + 0.998}{z^2 - 1.937z + 938}$
	Zeros: Frequency: ω_n = 432 [Hz] Damping ratio: ζ_n = 0.45	Zeros: Frequency: ω_n = 1096 [Hz] Damping ratio: ζ_n = 0.03
	Poles: Frequency: ω_d = 441 [Hz] Damping ratio: ζ_d = 1	Poles: Frequency: ω_d = 1021 [Hz] Damping ratio: ζ_d = 1

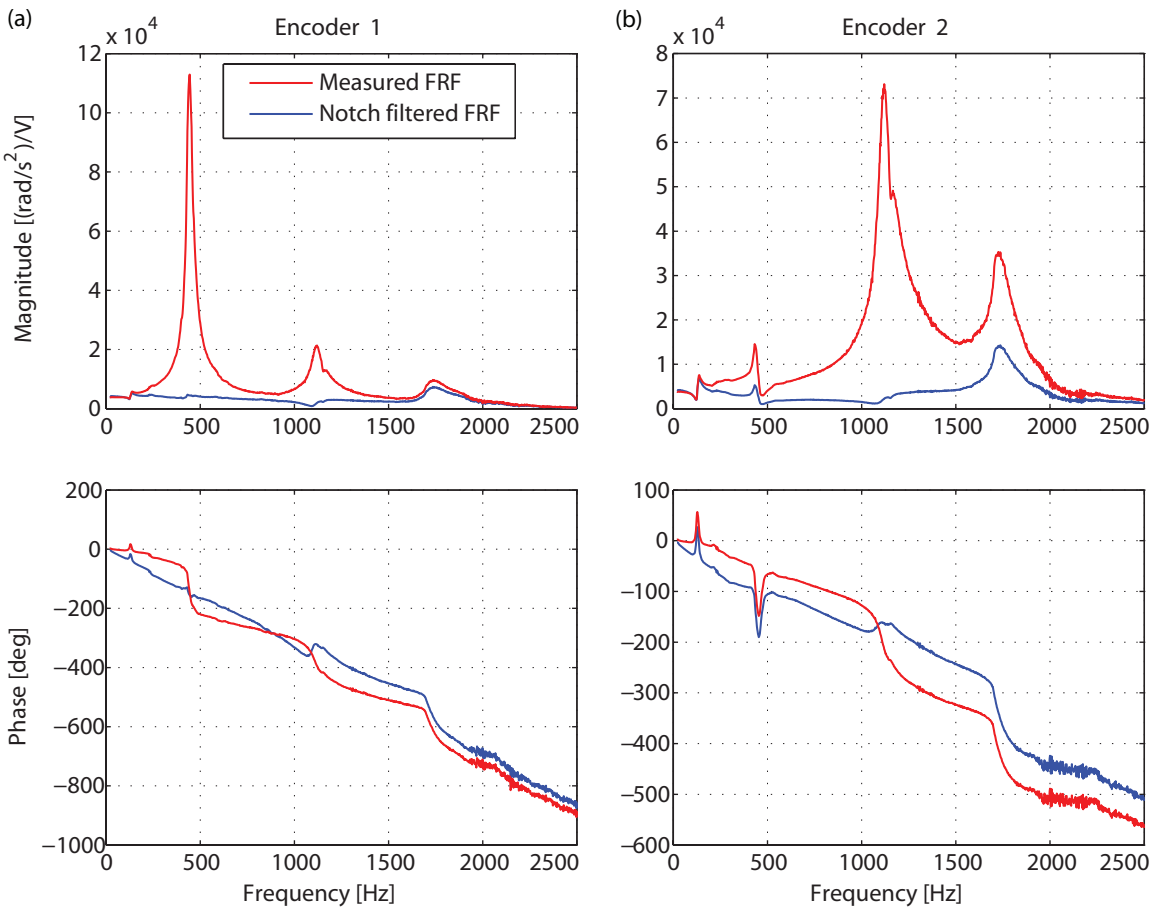

Figure 4.2: Original and notch-filtered torsional FRF's, measured from: (a) Encoder 1, (b) Encoder 2.

discrete-time denominator coefficients (d_1, d_2) can be expressed as [47]:

$$d_1 = -2\exp(-\zeta_d \omega_d T_s)\cos(\omega_d T_s \sqrt{1-\zeta_d^2}) \quad , \quad d_2 = \exp(-2\zeta_d \omega_d T_s) \tag{4.22}$$

where T_s [sec] is the sampling period. Similar expressions also hold for the numerator parameters. K_n is adjusted to yield unity d.c. gain:

$$N(z)\big|_{z=1} = 1 \Leftrightarrow K_n = \frac{1+d_1+d_2}{1+n_1+n_2} \tag{4.23}$$

By multiplying the experimentally measured torsional FRF's with the frequency response of the notch filters, it can be seen that the resultant FRF's achieve fairly flat gains up to about 1300 Hz, as shown in Figure 4.2. These notch filters are used to attenuate the excitation of the structural vibrations that can be caused by the ASMC, which was designed considering only rigid body dynamics.

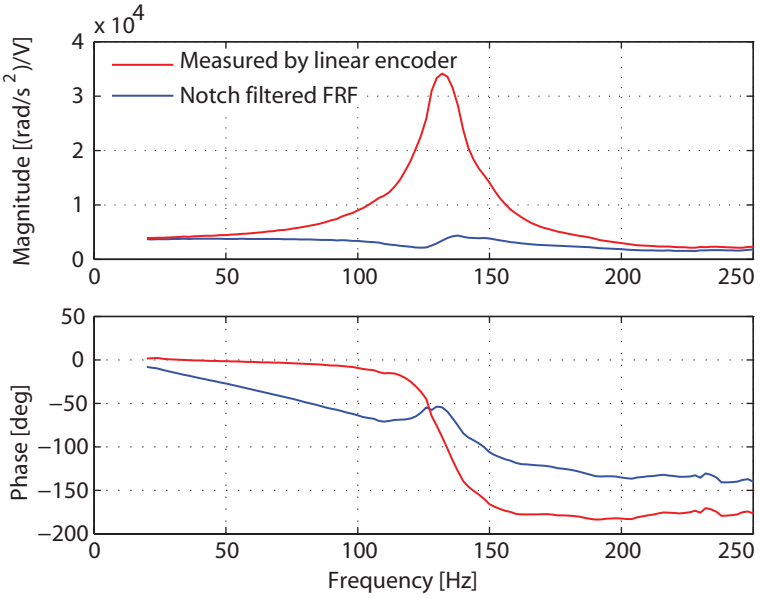

Figure 4.3: Original and notch filtered FRF of the 1st axial mode.

4.4.2 Notch Filtering of the 1st Axial Mode

When direct linear feedback is used from the table's translational motion, the first axial mode contributes a significant resonance at 132 Hz with nearly 10 times gain magnification. This resonance can be highly detrimental to the stability of the closed-loop system, unless it is either attenuated or explicitly considered in the controller design. Hence, another notch filter is designed to counteract the effect of this mode. The filter assumes the same structure as in Eq. (4.21), with the following discrete-time parameters.

$$N_{ax}(z) = 1.018\frac{z^2 - 1.994z + 0.996}{z^2 - 1.950z + 0.952} \tag{4.24}$$

The numerator frequency and damping ratios are ω_n=127.4 Hz and ζ_n=0.05, and the corresponding parameters for the denominator are ω_d=130 Hz and ζ_d=0.6. Similar to the notch filters designed for torsional modes, the sampling period is T_s = 1/20,000 sec. The open loop FRF of the axial mode, observed by linear encoder, is shown in Figure 4.3, before and after applying the notch filter. The graph verifies that the notch filter has been designed to successfully attenuate this mode.

4.5 Nonlinear Friction Compensation

During velocity direction change in the drive, friction changes discontinuously. Although the controller already has a built-in disturbance adaptation feature, it cannot immediately detect and

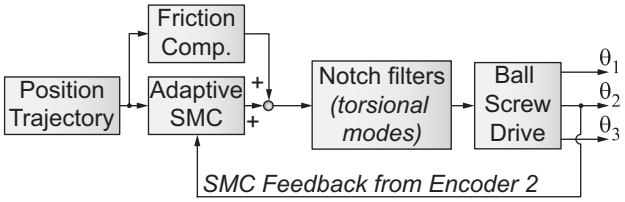

Figure 4.4: Designed ASMC with notch filtering and feedforward friction compensation (position feedback loop closed with Encoder 2).

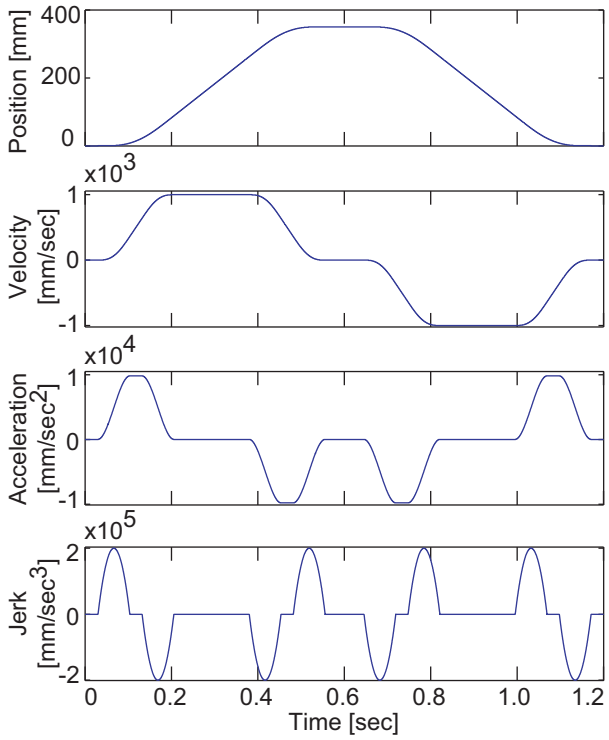

Figure 4.5: Commanded position trajectory.

compensate for sudden changes in the friction force. In fact, faulty estimation of the friction force during such a transient phase results in further deterioration of the tracking accuracy. In multi-axis machining, this can also result in the deterioration of the contouring (geometric tool positioning) accuracy. Hence, in order to avoid this problem, feedforward nonlinear friction compensation is applied.

The friction compensation signal is generated using the model in Eq. (3.9), by substituting the reference velocity $\dot{\theta}_{ref}$, and injecting it in feedforward as shown in Figure 4.4. Necessary scaling has been applied to account for the motor torque (K_t) and amplifier current (K_a) gains:

$$u_{fric} = \frac{\mathrm{sgn}(\dot{\theta}_{ref})}{K_a K_t}\left[T_s + T_d\left(1 - e^{-\left|\dot{\theta}_{ref}\right|/\Omega}\right)\right] \tag{4.25}$$

4.6 High Speed Tracking Tests

The ASMC designed for rigid body dynamics, together with notch filters and feedforward friction compensation, were tested in high speed tracking experiments. Two different cases were considered. Case 1 considers rotational position feedback from the ball screw. Case 2, on the other hand, uses direct position measurement from the table, obtained through the linear encoder. As an additional improvement upon the rotary feedback case, active damping of the first torsional mode is also investigated using a simple but effective vibration cancellation strategy. The advantages and disadvantages of both feedback configurations are discussed in the context of the tracking results. Both cases were tested using a jerk continuous trajectory, shown in Figure 4.5. This trajectory has 350 mm displacement and 1000 mm/sec feed. The rotary feedback case was tested with 1 g acceleration, whereas 0.5 was used in the linear feedback case. The maximum jerk value was 200,000 mm/sec^3.

4.6.1 Rotational Feedback

In this case, the position loop was closed using rotary Encoder 2, which is very close to the motor. This results in collocated control from the standpoint of the first axial and first torsional mode. At higher frequencies (i.e. 2nd torsional mode), the acceleration FRF measured from Encoder 2 lags 180° behind the actuation thereby loosing its collocated nature, as seen in Figure 3.13. Feedback from Encoder 2 has been preferred over Encoder 1, because it exhibits significantly lower phase lag,

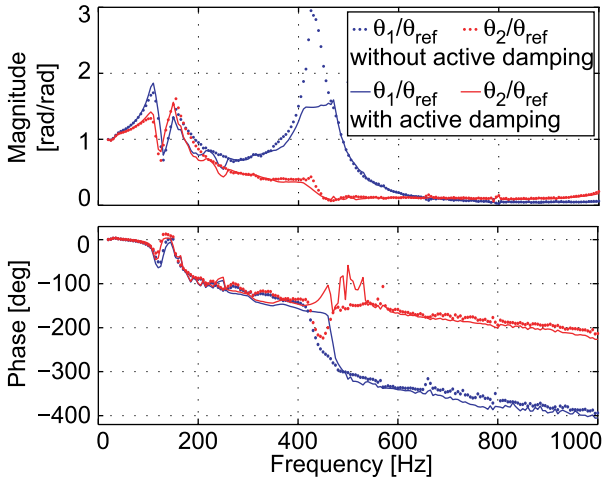

Figure 4.6: Closed loop tracking FRF's without and with active damping of the 1st torsional mode.

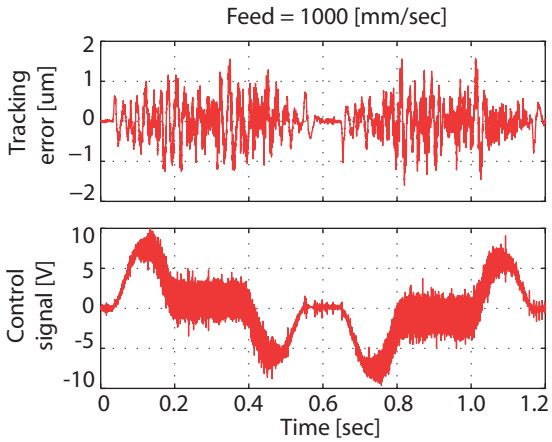

Figure 4.7: Experimental high speed tracking result for Adaptive SMC using rotary feedback, with notch filtering.

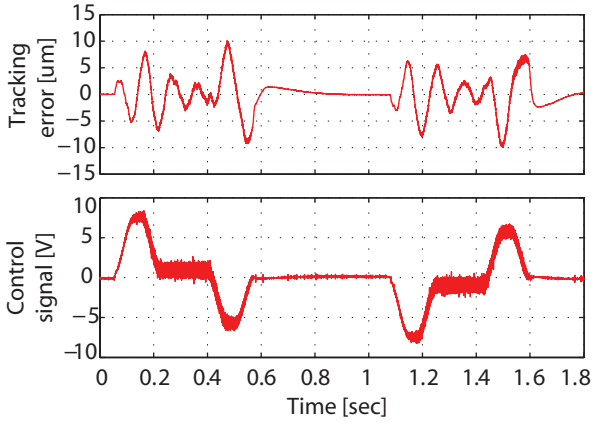

Figure 4.8: Experimental high speed tracking result for Adaptive SMC using rotary feedback, without notch filtering.

particularly up to the first torsional mode's frequency of 445 Hz, as seen in Figure 3.13. This enables higher control bandwidth to be achieved. On the other hand, the signal resolution of Encoder 2 (~10 nm) is significantly better than the resolution of Encoder 3 (305 nm). This results in a less noisy control signal and therefore better bandwidth. The implemented control scheme is shown in Figure 4.4.

By tuning the ASMC parameters to be λ = 1400 rad/sec (223 Hz), K_s = 0.15 V/(rad/sec), and ρ = 80 V/rad, an experimental command following bandwidth of 223 rad/sec has been achieved, as seen in Figure 4.6. The sampling frequency used is 20 kHz. Figure 4.7 shows the high speed tracking performance obtained. In order to interpret the tracking results in terms of the contribution to the linear positioning accuracy, the position unit has been changed to microns (um), using the ball screw pitch length (20 mm). As can be seen, the servo tracking error does not exceed 1.6 um. This

performance could be achieved after proper design of the ASMC, notch filters, and feedforward friction compensation. Without the notch filters, the sliding surface bandwidth could only be increased up to λ=450 rad/sec (72 Hz). This case resulted in a maximum tracking error of 10 um for the same trajectory, as can be seen in Figure 4.8. Although a high tracking accuracy was obtained with the rotary encoder feedback, this does not guarantee the accuracy of table motion. This is due to additional factors such as lead errors, elastic deformations, and backlash-like motion loss in the preloaded nut, which will be considered in more detail in later chapters.

One of the main ideas explored in this thesis is the use of active vibration control techniques to augment the stiffness and damping characteristics, and positioning bandwidth, of ball screw drives. To investigate the feasibility of realizing this on the experimental setup, a simple and effective torsional vibration cancellation strategy was implemented. This is an intuitive design based on the shape of the 1st torsional mode, which was identified in Chapter 3. Figure 3.9(a) shows this mode, which has a node close to the motor and Encoder 2 location, and maximum amplitude at the free end of the ball screw. This mode shape will be similar in all ball screw drives that are actuated in the traditional configuration, i.e. with the motor at one end and the other end being free to rotate. The idea in damping this mode is to cancel solely the high frequency motion in the vicinity of the 1st torsional resonance (445 Hz), by injecting appropriate torque inputs from the motor. The proposed strategy is shown in Figure 4.9. The "twist" on the ball screw is computed by subtracting the measurement of Encoder 2 from Encoder 1. The torsional vibrations are decoupled from the steady-state twist by applying high-pass filtering (HPF) at ω_c=390 Hz, which is just below the first torsional resonance. The cancellation signal is generated proportionally to the filtered position difference between the two encoders. This is done to counteract the vibration registered at the free end of the ball screw (Encoder 1) by commanding a similar motion close to the actuated end (Encoder 2). The cancellation signal is obtained as:

$$u_{damp} = K_p \frac{s^2}{(s+\omega_c)^2}[\theta_1 - \theta_2] \tag{4.26}$$

Considering the open loop acceleration response of the drive in Figure 3.10(b), the phase shift for the open loop FRF measured from Encoder 2 exceeds -180° after the second mode. This makes it difficult to dampen out the second and higher order torsional modes. The vibration cancellation signal is injected after the notch filters, in order to avoid attenuation by these filters, as shown in Figure 4.9. The overall control signal is obtained by combining the contribution of each component:

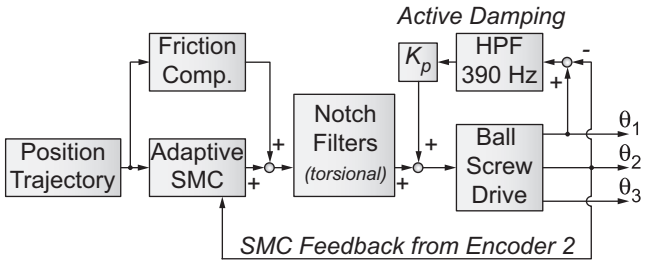

Figure 4.9: Proposed control strategy for active vibration suppression of the 1st torsional mode.

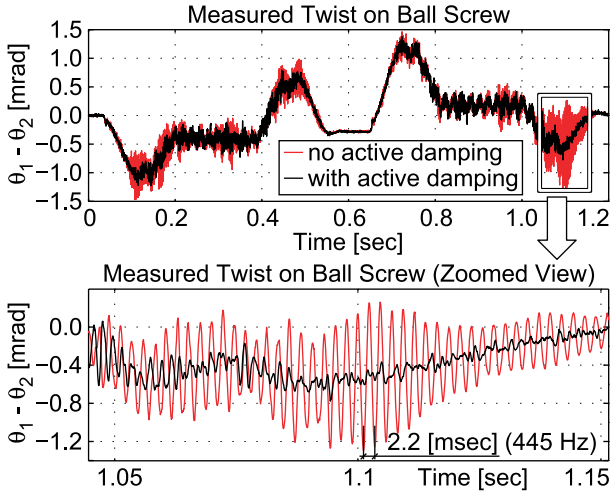

Figure 4.10: Contribution of active damping in attenuating ball screw torsional vibrations.

$$u = N(s) \cdot \lfloor u_{smc} + u_{fric} \rfloor + u_{damp} \tag{4.27}$$

Above, $N(s)$ represents the torsional notch filters, u_{fric} is the friction compensation signal, and u_{damp} is the vibration cancellation signal for the 1st torsional mode.

Figure 4.6 shows the experimentally measured tracking transfer functions through Encoders 1 and 2. As mentioned earlier, Encoder 2 is the principal feedback in closing the position loop. The difference between Encoders 1 and 2 is used in generating the vibration cancellation signal. Considering Figure 4.6, a positioning bandwidth of 223 Hz has been achieved in the tracking response measured through Encoder 2. The application of active damping does not seem to alter the closed loop dynamics registered from this encoder significantly. Considering the frequency response measured though Encoder 1, the contribution of active damping in reducing the first torsional resonance at 445 Hz to half of its magnitude can clearly be seen.

This result was also verified by monitoring the position difference (i.e. twist) between Encoders 1 and 2 during trajectory tracking experiments. Measurements of the ball screw twist recorded without

and with active damping are shown in Figure 4.10. As expected, the twist profile bears resemblance to the control signal (i.e. proportional to drive's torque) shown in Figure 4.7, which can be approximately constructed from a linear combination of the velocity and acceleration profiles in Figure 4.5. This indicates the presence of elastic deformation due to the actuation torque, which is addressed in more detail in Chapter 7. Following the quasi-static elastic twist, the largest motion component is the vibration registered at the first torsional frequency of 445 Hz, particularly when active damping is not used. With the application of active damping, these vibrations are significantly attenuated, resulting in smoother and more efficient motion of the ball screw mechanism.

One particular advantage of this vibration cancellation strategy is its robustness against changes in the drive's axial location. In frequency domain identification tests presented in Section 3.4.1 (Figure 3.14), it was seen that the natural frequencies and damping ratios of the torsional modes varied very little with changes in the axial position of the table and the excitation amplitude. This result was also confirmed in another study on a different feed drive system [20], indicating that axially transmitted reaction forces have only a minor influence on the torsional dynamics of the ball screw drive. Hence, the closed loop response achieved by modeling and cancelling out the torsional vibrations would not be significantly altered during the normal course of the drive's operation, particularly in the presence of axial position changes and external cutting and friction force disturbances. One drawback of this scheme, of course, is the requirement to use a second encoder at the free end of the ball screw.

Although the presented scheme was found to be effective in damping out the first torsional mode of the ball screw, it was observed to result only in negligible improvement in the final linear positioning accuracy of the table. This is because vibrations of the 1st axial mode at 132 Hz have a more dominant effect on the table motion than the torsional mode. The higher frequency (445 Hz) vibrations due to the torsional mode are already attenuated before they are transferred to the table. Hence, the final linear tracking accuracy does not improve significantly with active damping of the first torsional mode. Nevertheless, these results demonstrate the ability of the motor to excite or attenuate the structural vibrations of the ball screw up to a frequency of 450 Hz, which is sufficient for controlling the dynamics of the first axial mode, addressed in Chapter 6.

4.6.2 Using Linear Feedback

In this case, the position loop is closed using a linear encoder. This allows high steady-state accuracy to be achieved at the table level, since the linear encoder measurement directly represents the table position. However the bandwidth is limited due to the first axial mode at 132 Hz, which originates from the flexibility of the nut, ball screw, and fixed thrust bearing. This creates a non-collocated

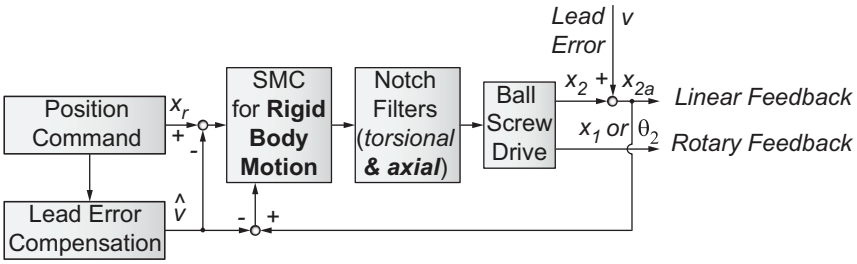

Figure 4.11: Designed ASMC with notch filtering of the torsional and axial modes and feedforward friction compensation (Linear encoder used for feedback).

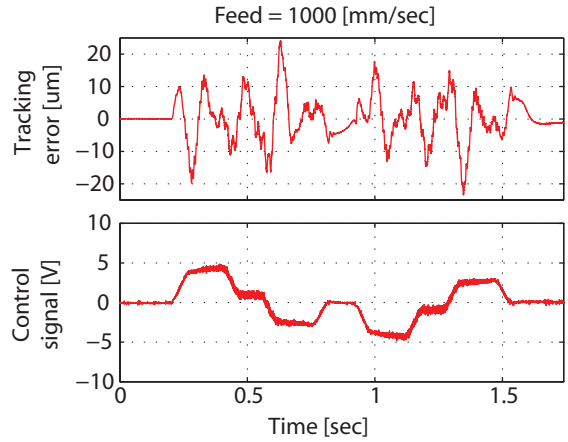

Figure 4.12: Experimental high speed tracking result for ASMC using linear feedback.

control situation, as the actuation and measurement are obtained from different points with significant dynamics of the torsional and axial vibrations in between. The first axial mode results in two problems associated with achieving high bandwidth control. The first one is the resonance peak in the feedback, which can be attenuated with a notch filter. The other problem, which is more severe, is the increased phase lag compared to feedback from the rotary encoder, which can be seen in Figure 3.16. The added phase lag prevents the achievement of a high crossover frequency, and therefore bandwidth.

Another problem associated with the ball screw motion transmission originates from the lead errors, which are caused by imperfections of the groove on the ball screw. These imperfections typically cause 2-3 um of additional positioning error, in the form of a sinusoidal function of ball screw rotation angle. These errors have been modeled and compensated in detail in Chapter 6 and Chapter 7. In the experimental result here, the lead error model that has been developed in Chapter 6 has been used to mitigate the effect of lead errors as much as possible, in order to observe the ideal tracking performance that can be realized with ASMC, notch filters, and feedforward friction compensation. The control configuration is shown in Figure 4.11. The details of the lead error cancellation strategy can be found in Section 6.3.

Because the frequency of the axial mode is relatively low, the sliding surface bandwidth λ could only be increased to 70 Hz. The values of K_s and ρ were tuned to be 0.08 V/(rad/sec) and 10 V/rad, respectively. To be consistent with the rotary feedback case, the position units in the control gains are expressed in terms of ball screw rotation angle (in radians). In this implementation, a sampling frequency of 8 kHz was used. The tracking result is shown in Figure 4.12, where the maximum error is around 24.1 um. The tracking accuracy could be improved further to 9.2 um, by increasing the sliding surface bandwidth, but this resulted in poor stability margins for the controller.

The control bandwidth limitation imposed by the 1st axial mode, which in turn affects the tracking accuracy, is clearly seen in this result. Later in this thesis, Chapter 6 will focus on overcoming this limitation by designing an ASMC that actively compensates for the axial vibrations of the ball screw, thereby achieving higher bandwidth and accuracy. In Chapter 7, an alternative technique will be investigated where the main position loop is closed using rotary collocated feedback (which achieves high bandwidth as demonstrated in Section 4.6.1), and linear encoder feedback is used only in the low frequency range for disturbance adaptation, to eliminate steady-state positioning errors. In addition, the influence of elastic deformations and lead errors will also be taken into account and compensated, in order to achieve a significant improvement in the final linear positioning accuracy of the ball screw drive system.

4.7 Limitations

Although ASMC with notch filtering was found promising, the controller performance depends on accurate knowledge of resonance modes (ω_n, ξ) and rigid body dynamic parameters (inertia, viscous damping, and disturbance bounds). Also, successful implementation of active vibration damping requires high sampling rates to detect the resonances of interest, and high resolution feedback to detect the corresponding vibration with minor displacements.

4.8 Conclusions

In this chapter, Adaptive Sliding Mode Control (ASMC) has been used to achieve high bandwidth control on a ball screw drive. The ASMC was designed based on rigid body dynamics. Feedforward friction compensation was added to improve the positioning accuracy at velocity reversals. Structural resonances were handled using notch filters, designed based on the FRF's identified in Chapter 3. The effectiveness of the control scheme was validated for rotary and linear feedback scenarios. Using rotary feedback resulted in higher controller bandwidth (223 Hz), which also contributes to higher servo stiffness. However, the final positioning accuracy of the table is not guaranteed, since the

motion delivery in a ball screw mechanism suffers from lead errors, elastic deformations, and nut hysteresis. When direct linear feedback was used, the bandwidth of the control system had to be significantly lower (113 Hz), due to the influence of the axial mode being seen in feedback loop. However, this configuration allows for the steady state positioning errors to be significantly reduced.

As validation of the feasibility of conducting structural control on the ball screw drive, a simple vibration cancellation technique for damping out the 1st torsional mode was also developed and successfully implemented. This damping technique results in smoother and more efficient motion, by reducing the magnitude of torsional vibrations excited at the first mode. However, its contribution to the linear positioning accuracy of the table was hardly noticeable.

Building on these results, in the proceeding chapters, the control law will be further developed to compensate for torque ripples, axial vibrations, lead errors, and elastic deformations, to achieve superior positioning performance on the ball screw drive.

Chapter 5
Modeling and Compensation of Torque Ripples

5.1 Introduction

In this chapter, the torque ripples in the ball screw drive are modeled and compensated in the control law. In Section 5.2, a ripple model is identified which comprises of the most significant harmonic components in the motor-felt disturbance, observed using through a Kalman filter. In Section 5.3, a feedforward compensation scheme is developed which utilizes the identified ripple model. Experimental results are presented in Section 5.4, that validate the tracking improvement obtained by pre-compensating for the torque ripples. The conclusions of the chapter are in Section 5.6.

5.2 Identification of Torque Ripples using a Kalman Filter

Torque ripples were observed through a Kalman filter as an equivalent disturbance at the drive's input. These observations were used to construct a model, which will be used in feedforward cancellation of the equivalent torque ripples in the drive system.

Figure 5.1 shows the disturbance observation scheme using a Kalman filter, which was also used in nonlinear friction identification in Section 3.3.4. The developed Kalman filter has three poles at 358 Hz with damping ratios of $\zeta_{1,2} = 0.5$ and $\zeta_3 = 1.0$. The control signal equivalent disturbance (d) is observed while jogging the axis back and forth at constant speeds. For each speed, the disturbance is broken down to an average value ($\bar{d}$), representing the control signal equivalent friction torque at that speed (i.e. $\bar{d} = T_{fric}/(K_a K_t)$), and an oscillatory component ($\tilde{d}$), which represents the sum of the torque ripples originating from both the motor and the drive mechanism. From the disturbance observations, the control signal equivalent torque ripple $\hat{\tilde{d}}$ [V] can be determined as:

$$\hat{\tilde{d}} = \hat{d} - \hat{\bar{d}} \tag{5.1}$$

As expected, the torque ripple ($\hat{\tilde{d}}$) is observed to have dominant harmonics at integer multiples of the motor rotation frequency. A sample case is shown in Figure 5.2 which was obtained by taking the FFT (Fast Fourier Transform) of the observed ripple signal, while the drive was traversing in the positive direction at a constant speed of 100 mm/sec. These dominant harmonics were consistently observed in tests that were conducted at different speeds.

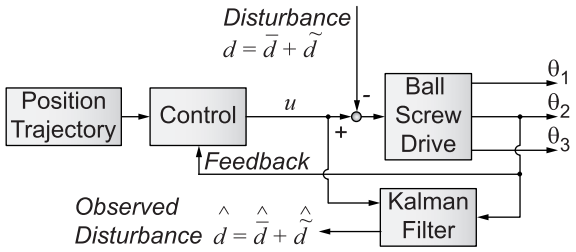

Figure 5.1: Disturbance observation using a Kalman filter.

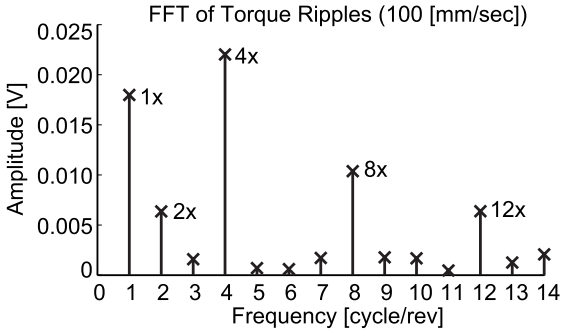

Figure 5.2: Torque ripple harmonics.

The 1× and 2× harmonics are attributed to the mechanical torque ripples which mainly originate from the coupling between the motor and ball screw, as they change each time the motor is detached from the drive and mounted back again. The 4×, 8×, and 12× harmonics originate from the motor, which was verified in additional tests conducted with the motor detached. Considering these five major harmonics (1×, 2×, 4×, 8×, 12×), the below ripple model has been proposed:

$$\tilde{d}_{\text{model}} = \sum_{i=1}^{5} A_i^{+/-} \sin(f_i \theta + \phi_i^{+/-}) \tag{5.2}$$

Above, $A_i^{+/-}$ [V] and $\phi_i^{+/-}$ [rad] represent the amplitude and phase shift of the i^{th} harmonic. The $(+/-)$ superscript indicates the direction of motion. f_i [cycle/rev] is the harmonic frequency with respect to the drive's full revolution (i.e. $f_1 = 1$, $f_2 = 2$, $f_3 = 4$, $f_4 = 8$, $f_5 = 12$ cycle/rev), and θ [rad] is the angular position of the drive.

The amplitude and phase values of the model were identified by applying Least Squares technique on the estimated torque ripple profiles ($\hat{\tilde{d}}$) [44]. Figure 5.3 shows the amplitude and phase values for the five harmonics, observed during forward and backward axis motions at different speeds. Readings in Figure 5.3(a) are arranged with respect to axis velocity. Readings in Figure 5.3(b) are arranged

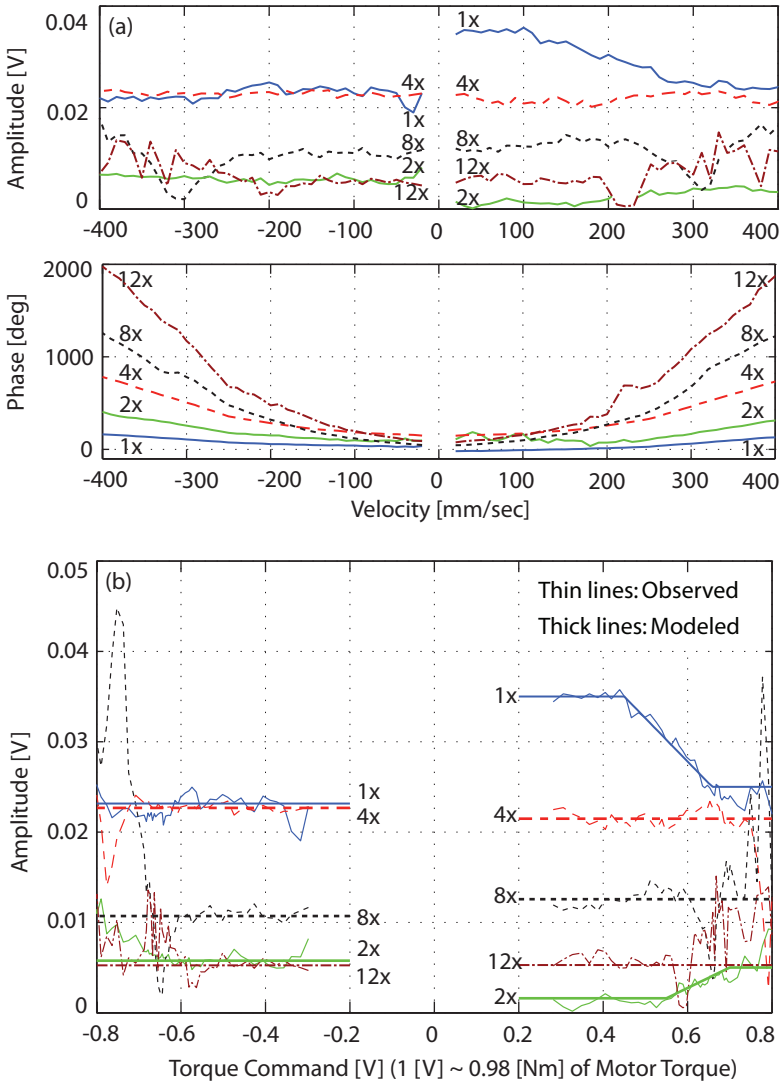

Figure 5.3: Observed and modeled torque ripple amplitude and phase shift varying with: (a) Axis velocity, (b) Torque command.

with respect to the torque command. The identified amplitudes become scattered at high speeds, where measurement and control signal noise corrupts the disturbance estimation.

As seen in Figure 5.3, the amplitudes of motor torque ripples (4×, 8×, and 12× harmonics) are nearly constant in forward and backward motions. The amplitudes of the mechanical torque ripples (1× and 2× harmonics) are almost constant during motion in the backward direction; but exhibit a linear variation as a function of the torque command in the forward direction. The physical reason behind this unsymmetrical behavior does not lend itself to a straightforward explanation. As indicated earlier, these harmonics are attributed to the coupling, which is a flexible disc (i.e. diaphragm) type coupling. This coupling transfers the motor torque through two sets of flexure plates. These plates

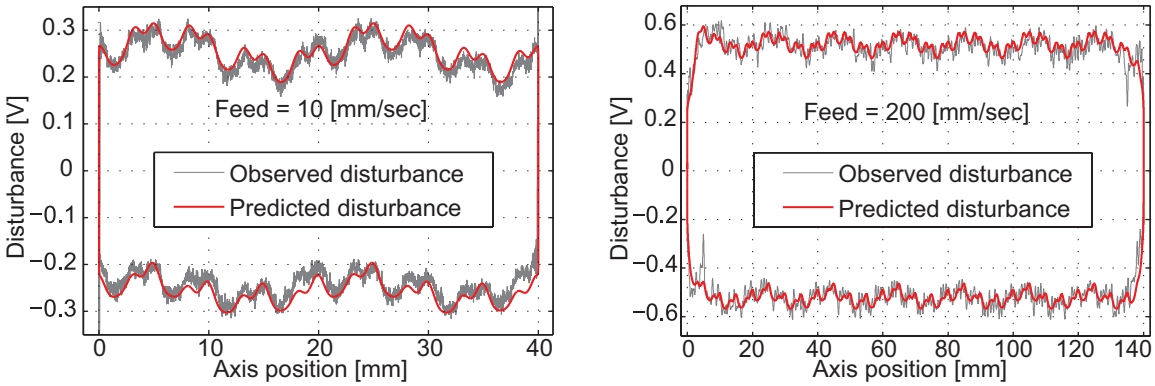

Figure 5.4: Modeled and observed disturbance at different axis velocities.

provide high torsional stiffness and absorb minor axis misalignments by undergoing repeated bending cycles, as the ball screw rotates. This results in the storage and release of energy, causing the observed torque ripples. When there are geometric imperfections in the flexural elements or in the coupling assembly, the coupling will not behave like an ideal spring, but will deliver additional parasitic motion to the drive mechanism. The unsymmetrical nature of the observed ripples may be attributed to such parasitic motion. However, this is not known for sure at the moment, and merits further research beyond this thesis.

In order to capture the observed ripple characteristic accurately, the proposed model uses a combination of constant and linearly varying amplitudes for the first two harmonics in the positive direction of motion:

$$A_i^+ = \begin{cases} a_{1i} & \text{if} \quad u \le u_{1i} \\ a_{1i} + m_i\,(u - u_{1i}) & \text{if} \quad u_{1i} < u < u_{2i} \\ a_{2i} & \text{if} \quad u \ge u_{2i} \end{cases} \quad \text{where} \quad i = 1,2 \tag{5.3}$$

In Eq. (5.3), u [V] is the torque command (i.e. control signal). For the 1st harmonic, a_{11}=0.035 V, a_{21}=0.025 V, m_1= –0.048, u_{11}=0.45 V, and u_{21}=0.659 V. For the 2nd harmonic, a_{12}=0.0016 V, a_{22}=0.005 V, m_2=0.0227 , u_{12}=0.55 V, and u_{22}=0.70 V. The remaining ripple amplitudes are constant and have been summarized in Table 5.1. The modeled amplitudes have been overlaid on top of the observations in Figure 5.3(b), which can be seen to be in good agreement.

Considering Figure 5.3(a), the observed phase lag associated with the harmonics increases with increasing axis velocity. In fact, the phase lag increase is steeper for higher frequency harmonics. This is due to the estimation phase lag inherent in the Kalman filter. Assuming that the torque ripples are position dependent, and always occur at the same location, the phase shift values (ϕ_i) were

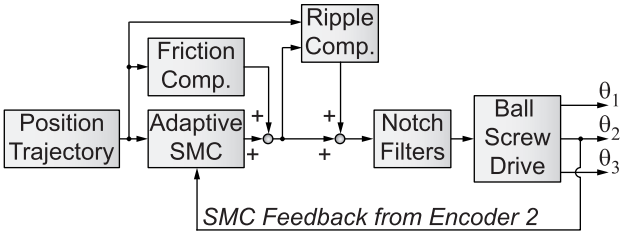

Figure 5.5: Adaptive SMC with torque ripple compensation block diagram.

identified by taking their lowest velocity values as an initial guess, and performing iterative adjustments until the overall ripple model in Eq. (5.2), combined with the friction model in Eq. (3.9), was successful in reconstructing the observed disturbance profile.

The developed ripple and friction models have been verified by reconstructing the estimated disturbance profiles, using the axis position and torque command data. Sample observed and predicted disturbance profiles are shown in Figure 5.4, where it can be seen that the developed friction and torque ripple models are successful in predicting the equivalent disturbance in the drive mechanism. There are minor discrepancies at the beginning and end of forward and backward motions, which are attributed to changes in the actual friction from time to time. In order to yield a cleaner signal for visual appeal, a slower Kalman filter has been used in generating the estimated disturbance profile in these figures ($\omega_{1,2,3} = 148$ Hz, $\zeta_{1,2} = 0.5$, $\zeta_3 = 1$).

The Kalman filter used in torque ripple observation has 3 poles at 358 Hz, which is high enough to capture the middle and low frequency harmonics with little phase lag. For example, considering that the ball screw has 20 mm lead, the 4× harmonic component will produce a 80 Hz torque disturbance if the table is traveling at 400 mm/sec speed (400 / 20 × 4 = 80 Hz). This is well below the Kalman filter pole frequency. However, for higher frequency harmonics (8×, 12×) the phase lag caused by the Kalman filter will be more evident as the frequency of these ripples approach and exceed the filter bandwidth, particularly at high travel speeds. Hence, as a final correction to the ripple model, minor

Table 5.1: Identified amplitude and phase values for torque ripple harmonics.

Harmonic [cycle/rev]	Amplitude [V]		Phase [deg]	
	Forward motion (A_i^+)	Backward motion(A_i^-)	Forward motion (ϕ_i^+)	Backward motion (ϕ_i^-)
1×	A_1^+ in Eq. (5.3)	0.0232	-10.0	10.0
2×	A_2^+ in Eq. (5.3)	0.0058	-45.5	-34.5
4×	0.0215	0.0227	78.5	68.0
8×	0.0126	0.0107	18.0	35.0
12×	0.0053	0.0052	50.0	60.0

adjustments were made to the phase shift values while the model was being used in feedforward cancellation of the actual torque ripples, as explained in Section 5.3. The Kalman filter was left active to observe the equivalent torque disturbance felt by the motor, after ripple cancellation. When the ripple model was adjusted to be in close agreement with the actual torque ripples, the disturbance profile estimated by the Kalman filter assumed a flat shape, corresponding only to the friction component. This was used as an indication that the phase shift parameters in the torque ripple model were tuned to represent the actual torque ripples as closely as possible. The final phase shift values have been summarized in Table 5.1.

5.3 Torque Ripple Compensation

The motor and mechanical torque ripples were compensated in feedforward using the model developed in Section 5.2. The ripple compensation has been implemented in conjunction with the Adaptive Sliding Mode Control (ASMC) scheme developed in Chapter 4. The implementation block diagram is shown in Figure 5.5. The ripple compensation, injected into the control signal, is computed by substituting the reference position value into Eq. (5.2) as follows:

$$u_{\text{ripple}} = \sum_{i=1}^{5} A_i^{+/-} \sin(f_i \theta_{ref} + \phi_i^{+/-}) \tag{5.4}$$

5.4 Experimental Tracking Results

The experimental accuracy achieved with the proposed ripple compensation scheme is shown in Figure 5.6. A jerk continuous trajectory with 350 mm displacement, 1000 mm/sec feed, 1 g acceleration, and 200,000 mm/sec^3 jerk was commanded, as shown in Figure 4.5. The control loop was closed at 8 kHz sampling frequency. At the time this algorithm was tested, the linear encoder had not yet been instrumented on the setup. Hence, the tracking error profiles were computed based on rotary position measurements. In order to interpret the tracking results in terms of the contribution to the linear positioning accuracy, the position unit has been changed to microns (um), using the ball screw pitch length (20 mm). As can be seen, the servo tracking error does not exceed 0.95 um., which is better than the tracking accuracy of 1.6 um, that was obtained for the same trajectory in Section 4.6.1.

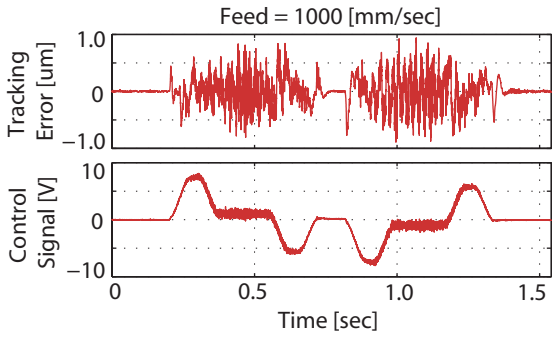

Figure 5.6: Experimental tracking result at 1000 mm/sec using ASMC with torque ripple compensation.

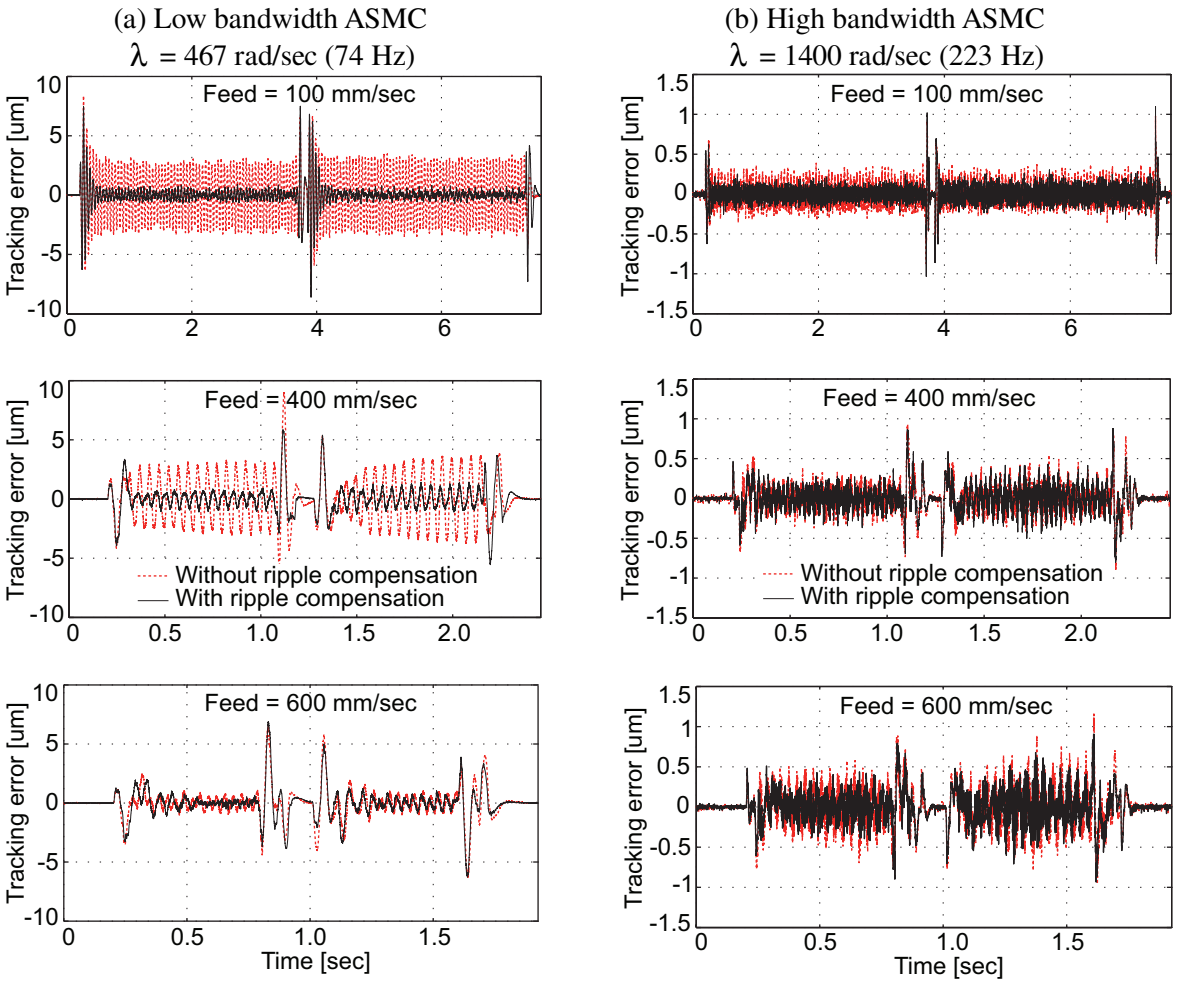

Figure 5.7: Experimental tracking performance without and with torque ripple compensation for: (a) Low bandwidth ASMC, (b) High bandwidth ASMC.

To further investigate the contribution of torque ripple compensation on the motion smoothness and accuracy, additional tests were conducted at different speeds: 100, 400, and 600 mm/sec, using different control bandwidths: λ = 1400 rad/sec (223 Hz) and λ = 467 rad/sec (74 Hz, i.e., 1/3rd of the original bandwidth). The K_s and ρ values for the 223 Hz design are presented in Section 4.6.1. Their values for the 74 Hz bandwidth controller are K_s = 0.05 V/(rad/sec) and ρ = 26.7 V/rad. A similar position trajectory, with different feedrate values, was used in the additional tracking tests. As can be seen in Figure 5.7, a considerable improvement in the tracking error is seen at low axis speeds, particularly with the low bandwidth controller. The contribution of torque ripple compensation is also noticeable in high bandwidth control cases and higher speeds. However, it becomes less significant due to the control signal assuming larger amplitudes with higher variance, in comparison to the torque ripple. Overall, the proposed compensation of torque ripples is observed to improve the smoothness and accuracy of the feed motion delivered by the ball screw drive system.

5.5 Limitations

The presented torque ripple compensation technique is model-based and is performed in feedforward. Hence, long-term deviations of actual torque ripples from their modeled value could limit the compensation scheme's performance. Also mechanical torque ripples (1× and 2× harmonics) could change if the motor and/or coupling are reinstalled. Hence, the ripple model needs to be updated from time to time to ensure that the compensation is accurate and successful.

5.6 Conclusions

In this chapter, the motor and mechanical torque ripples were modeled using Kalman filtering and successfully compensated in the Adaptive Sliding Mode Control scheme, developed in Chapter 4. The torque ripple modeling and compensation was realized at the motion control level, instead of the current loop, which allows the methodology to be applied on different types of feed drives in a generic manner. The compensation improves the smoothness and accuracy of the drive's motion, especially at low speeds and low control bandwidths. The tracking performance is also improved at high speeds and high control bandwidths, but this is less evident due to the control signal assuming larger magnitudes and becoming more sensitive to measurement noise under these conditions. With the principal feedback being obtained from rotary Encoder 2, a tracking accuracy equivalent to 0.95 um of table motion was obtained while traversing the axis at 1000 mm/sec with 1 g accelerations.

Although the torque ripple compensation strategy appears to be highly effective, one of its drawbacks is the high computational load required to compute several harmonic (sinusoidal)

functions in real-time. This can be simplified through the use of efficient mathematical algorithms or look-up tables, etc. In any case, with the rapidly increasing availability of computational power, implementation of the developed ripple compensation scheme should not be a major issue on new generation motion controllers.

Chapter 6
Active Compensation of Axial Vibrations

6.1 Introduction

In this chapter, the Adaptive Sliding Mode Controller design is extended for active compensation of the 1st axial mode. This is done with the intention of increasing the control bandwidth and drive stiffness, while at the same time delivering a higher positioning accuracy at the table level. Section 6.2 presents the ASMC design where the dynamics of the 1st axial mode are explicitly considered in the plant model. In Section 6.3, the lead errors arising from imperfections of the ball screw are modeled and removed from the loop by offsetting their effect from the commanded trajectory and position feedback signals. Effectiveness of the proposed strategy is demonstrated in high speed tracking experiments in Section 6.4, where a linear positioning accuracy of 2.6 um has been maintained while traversing at 1000 mm/sec feed with 0.5 g acceleration transients. Detailed stability analysis in the frequency domain, which implicitly considers the effect of other vibration (i.e. torsional) modes and dynamics that were neglected during the controller design, is performed in Section 6.5. The conclusions for the chapter are presented in Section 6.7.

6.2 ASMC Design for a Flexible Drive System

This dynamics of the 1st axial mode were measured and approximately identified in Section 3.4.2. In Section 6.2.1, a lumped model comprising of two masses, a spring, and a damper is used to capture this mode as part of the drive transfer function. Applying the general ASMC design rules that were presented in Section 4.2, a control law is designed in Section 6.2.2 which actively dampens out the 1st axial mode while achieving a high positioning bandwidth. Since the controller is designed in state space, a state trajectory generator is also developed in Section 6.2.3, which ensures that all commanded state variables are physically compatible with each other.

6.2.1 Drive Model Considering the First Axial Mode

To identify the 1st axial mode, the open loop Frequency Response Functions (FRF's) relating the motor torque command to the ball screw and table acceleration were measured as shown in Figure 6.1. To have consistency in units, the table displacement has been represented in terms of the equivalent ball screw angular motion, by making use of the pitch length (h_p = 20 mm $\Rightarrow$ 1

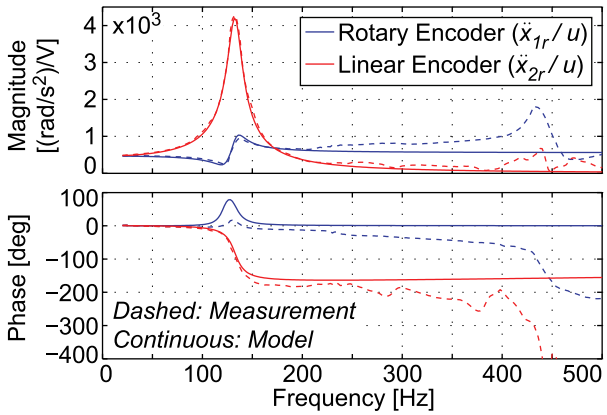

Figure 6.1: Open loop acceleration FRF's.

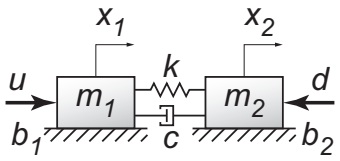

Figure 6.2: Flexible drive model used in controller design.

rad=3.1831 mm). The combined gain for the motor and amplifier, based on values identified in Chapter 3, is $K_a K_t$ = 0.98 Nm/V. As seen in the figure, the first axial mode is at 132 Hz and is very lightly damped (ζ = 0.056). When the position loop is closed using a linear encoder and this resonance is not compensated, it brings about a severe limitation in terms of the achievable control bandwidth. The second resonance occurs at around 445 Hz and is attributed to the 1st torsional mode, which was studied earlier in Chapter 3. Attenuation of this mode was presented earlier using active (Section 4.6.1) and a passive (Section 4.4.1) techniques, different from the approach presented here.

A two mass drive model, shown in Figure 6.2, was used in capturing the key dynamics of the ball screw drive including the 1st axial mode. In the figure, m_1 represents the inertia of the rotating components, such as the motor, the coupling, and the ball screw. m_2 represents the table inertia, which is subject to axial vibrations. b_1 and b_2 represent the viscous friction in the rotary bearings and linear guideways, respectively. k is the overall axial stiffness and c represents the damping induced in the preloaded nut. u is the motor torque command (i.e. control signal) and d represents external disturbances acting on the table, such as cutting forces and unmodeled nonlinear friction. x_1 and x_2 represent the ball screw rotational and table linear displacements, which are measured through the rotary Encoder 2 and the linear encoder, respectively.

The total inertia and viscous friction were identified in Chapter 3 using Least Squares parameter estimation. With knowledge of the drive's mass distribution (Table 3.1), the individual inertia values

were calculated to be m_1=1.858×10^{-3}, m_2=0.346×10^{-3} V/(rad/sec^2). b_1= 1.020×10^{-3}, and since the setup employs air guideways b_2=0 V/(rad/sec). On machines that have lubricated or roller guides, a nonzero value for b_2 would need to be identified.

There are several factors that influence the equivalent axial stiffness k. In particular, these are the individual stiffness values of the ball screw, preloaded nut, and thrust bearing. In addition, the preloaded nut serves as a special spring that couples different degrees of freedom together, especially in the torsional and axial directions. Detailed Finite Element studies have been conducted to analyze and simulate these effects [49][68][71], which require knowledge of the individual stiffness values. The damping, on the other hand, is difficult to predict analytically and is best identified by taking measurements from the real machine. In this study, the axial stiffness and damping were identified by matching the frequency response of the lumped model with the measured FRF's, as seen in Figure 6.1. The resulting values are k=202.21 V/rad and c=0.027 V/(rad/sec). It is seen that the model matches the drive's FRF closely up to 250 Hz. Above this frequency, additional dynamics attributed to the current loop and the 1st torsional mode become dominant, causing a variation from the model's frequency response. The drive model can be written in state space as:

$$\underbrace{\begin{bmatrix}\dot{x}_2\\ \ddot{x}_2\\ \dot{x}_1\\ \ddot{x}_1\end{bmatrix}}_{\dot{z}} = \underbrace{\left[\begin{array}{cc:cc} 0 & 1 & 0 & 0\\ \frac{-k}{m_2} & \frac{-c-b_2}{m_2} & \frac{k}{m_2} & \frac{c}{m_2}\\ 0 & 0 & 0 & 1\\ \hdashline \frac{k}{m_1} & \frac{c}{m_1} & \frac{-k}{m_1} & \frac{-c-b_1}{m_1}\end{array}\right]}_{\boldsymbol{A}} \underbrace{\begin{bmatrix}x_2\\ \dot{x}_2\\ x_1\\ \dot{x}_1\end{bmatrix}}_{z} + \underbrace{\begin{bmatrix}0\\0\\0\\ \frac{1}{m_1}\end{bmatrix}}_{\boldsymbol{B}}\underbrace{[u]}_{u} + \underbrace{\begin{bmatrix}0\\ \frac{-1}{m_2}\\0\\0\end{bmatrix}}_{\boldsymbol{W}}\underbrace{[d]}_{d}$$

$$= \left[\begin{array}{c:c} \boldsymbol{A}_{11} & \boldsymbol{A}_{12}\\ \hdashline \boldsymbol{A}_{21} & \boldsymbol{A}_{22}\end{array}\right]\begin{bmatrix}z_1\\ \hdashline z_2\end{bmatrix} + \begin{bmatrix}\boldsymbol{B}_1\\ \hdashline \boldsymbol{B}_2\end{bmatrix}[u] + \begin{bmatrix}\boldsymbol{W}_1\\ \hdashline \boldsymbol{W}_2\end{bmatrix}[d] \tag{6.1}$$

Above, the state vector z is divided into two parts. $z_2 = [\dot{x}_1]$ (velocity of m_1) is directly influenced by the input torque ($\boldsymbol{B}_2 = [1/m_1]$), whereas the remaining states $z_1 = [x_2 \quad \dot{x}_2 \quad x_1]^T$ are influenced indirectly ($\boldsymbol{B}_1 = \boldsymbol{0}_{3\times1}$), through the $\boldsymbol{A}_{12}z_2$ term. This separation is essential for formulating the sliding surface in the control law design.

6.2.2 ASMC Formulation

As stated in Section 4.2, the sliding surface selection is the first step in designing the ASMC. Here, this is achieved using the method of Equivalent Control [12], as explained in the following.

Considering at first only the regulation problem for the states in z_1 and ignoring the effect of external disturbances (i.e. $\boldsymbol{Wd} = \boldsymbol{0}$), the objective is to constrain the system states on to a stable sliding surface so that they eventually converge to zero. The sliding surface is defined as:

$$\sigma = \begin{bmatrix} s_1 & s_2 & s_3 & s_4 \end{bmatrix} \cdot \begin{bmatrix} x_2 \\ \dot{x}_2 \\ x_1 \\ \dot{x}_1 \end{bmatrix} = \boldsymbol{S}\boldsymbol{z} = \boldsymbol{S}_1 z_1 + \boldsymbol{S}_2 z_2 = 0 \tag{6.2}$$

where $\boldsymbol{S}_1 = [s_1 \quad s_2 \quad s_3]$ and $\boldsymbol{S}_2 = [s_4]$. When the states are on the sliding surface, $\sigma = 0$ should hold. Or in other words, the system states should satisfy $z_2 = -\boldsymbol{S}_2^{-1}\boldsymbol{S}_1 z_1$. Substituting this into the state transition expression for $\dot{z}_1$ (Eq. (6.1)) results in:

$$\dot{z}_1 = \boldsymbol{A}_{11} z_1 + \boldsymbol{A}_{12} z_2 = [\boldsymbol{A}_{11} - \boldsymbol{A}_{12}(\boldsymbol{S}_2^{-1}\boldsymbol{S}_1)] \cdot z_1 \tag{6.3}$$

The sliding surface parameters s_1, s_2, s_3, s_4 need to be determined so that the closed loop poles (i.e. eigenvalues of $[\boldsymbol{A}_{11} - \boldsymbol{A}_{12}(\boldsymbol{S}_2^{-1}\boldsymbol{S}_1)]$) can be assigned the desired natural frequency (λ, ω_n) and damping (ζ) values:

$$\text{eig}[\boldsymbol{A}_{11} - \boldsymbol{A}_{12}(\boldsymbol{S}_2^{-1}\boldsymbol{S}_1)] = \begin{cases} -\lambda \\ -\zeta\omega_n \pm j\omega_n\sqrt{1-\zeta^2} \end{cases} \tag{6.4}$$

This can be achieved using the standard pole placement design technique [48], by considering the similarity between Eq. (6.3) and the state feedback gain selection problem stated as: *Find* $\boldsymbol{K}$ *so that* $\dot{\boldsymbol{x}} = (\boldsymbol{A} - \boldsymbol{B}\boldsymbol{K})\boldsymbol{x}$ *has the desired eigenvalues*. Since there are 3 pole locations and 4 sliding surface parameters, the designer has to make a choice for one of the values in $\boldsymbol{S}$, which does not really affect the outcome. In this work, s_4 has been chosen as "1" for mathematical convenience. Since the design deals with trajectory tracking, the sliding surface is modified to consider the state tracking errors as,

$$\sigma = \boldsymbol{S}(z_r - z) = \underbrace{\begin{bmatrix} s_1 & s_2 & s_3 & 1 \end{bmatrix}}_{\boldsymbol{S}} \cdot \left\{ \begin{bmatrix} x_{2r} \\ \dot{x}_{2r} \\ x_{1r} \\ \dot{x}_{1r} \end{bmatrix} - \begin{bmatrix} x_2 \\ \dot{x}_2 \\ x_1 \\ \dot{x}_1 \end{bmatrix} \right\} \tag{6.5}$$

Above, z_r represents the reference state, comprising of position and velocity commands for m_2 and m_1, respectively.

The ASMC is designed by following the procedure set forth in [60] and [75], which was summarized in Section 4.2. Similar to the rigid body design case (Section 4.3) the external disturbance d is considered as the only unknown parameter, which needs to be adapted and cancelled out in the control law. The design is carried out by constructing the parameter-regressor expression in the form:

$$(\boldsymbol{SB})^{-1}\boldsymbol{S}(\dot{z}_r - \boldsymbol{A}\boldsymbol{z} - \boldsymbol{W}\boldsymbol{d}) = \boldsymbol{Y}(\dot{z}_r, z)\cdot\boldsymbol{P} \tag{6.6}$$

Above, $\boldsymbol{P}$ contains the unknown parameters and $\boldsymbol{Y}$ contains the corresponding regressors. Using the drive dynamics in Eq. (6.1) and the sliding surface definition in Eq. (6.5), the parameter-regressor expression is obtained as,

$$\boldsymbol{Y}(\dot{\boldsymbol{z}}_r, \boldsymbol{z})\cdot\boldsymbol{P} = \begin{bmatrix} y_1 & y_2 \end{bmatrix}\cdot\begin{bmatrix} 1 \\ d \end{bmatrix} = y_1 + y_2 d \tag{6.7}$$

where,

$$\left.\begin{aligned} y_1 &= m_1 s_1(\dot{x}_{2r} - \dot{x}_2) + m_1 s_3(\dot{x}_{1r} - \dot{x}_1) + m_1 s_2\left(\ddot{x}_{2r} + \frac{k}{m_2}x_2 + \frac{c+b_2}{m_2}\dot{x}_2 - \frac{k}{m_2}x_1 - \frac{c}{m_2}\dot{x}_1\right) \\ &\quad + m_1\left(\ddot{x}_{1r} - \frac{k}{m_1}x_2 - \frac{c}{m_1}\dot{x}_2 + \frac{k}{m_1}x_1 + \frac{c+b_1}{m_1}\dot{x}_1\right) \\ y_2 &= (m_1/m_2)s_2 \end{aligned}\right\} \tag{6.8}$$

As formulated before in Chapter 4, a Lyapunov function postulated as:

$$V = \frac{1}{2}\left[\sigma^T(\boldsymbol{SB})^{-1}\sigma + (\boldsymbol{P} - \hat{\boldsymbol{P}})^T\boldsymbol{\Gamma}(\boldsymbol{P} - \hat{\boldsymbol{P}})\right] \tag{6.9}$$

where $\boldsymbol{SB}$ is a positive definite symmetrical matrix and $\boldsymbol{\Gamma}$ is a diagonal matrix with positive entries. This function will be positive when the states are not on the sliding surface ($\sigma \neq 0$) or there is discrepancy between the actual and estimated system parameters (i.e. $\boldsymbol{P} \neq \hat{\boldsymbol{P}}$). It was shown in [75] that as long as the real and estimated parameters are within known bounds (i.e. $\boldsymbol{P}_{\min} \le \boldsymbol{P} \le \boldsymbol{P}_{\max}$ and $\boldsymbol{P}_{\min} \le \hat{\boldsymbol{P}} \le \boldsymbol{P}_{\max}$), a control law to stabilize the system (by achieving $\dot{V} < 0$) can be obtained as:

$$u_{smc} = K_s\sigma + \boldsymbol{Y}(\dot{z}_r, z)\cdot\hat{\boldsymbol{P}} = K_s\sigma + y_1 + y_2\hat{d} \tag{6.10}$$

In the control law, K_s is a positive feedback gain to push the state errors onto the sliding surface. Expressions for σ, y_1, and y_2 are given in Eq. (6.5) and (6.8). In the ideal case, where the actual

drive dynamics perfectly matches the model in Eq. (6.1), the disturbance adaptation would be implemented as [60], [75]:

$$\dot{\hat{d}} = y_2 \rho \kappa \sigma = \frac{m_1 s_2}{m_2} \rho \kappa \begin{bmatrix} s_1(x_{2r} - x_2) + s_2(\dot{x}_{2r} - \dot{x}_2) \\ + s_3(x_{1r} - x_1) + \dot{x}_{1r} - \dot{x}_1 \end{bmatrix} \tag{6.11}$$

Above, $\rho > 0$ is the adaptation gain and κ is a binary variable to switch the adaptation on and off in order to contain the disturbance estimate within specified bounds ($d_{\min} \le \hat{d} \le d_{\max}$), similar to the design in Section 4.3. In experimental trials, it was seen that this adaptation law, which uses feedback from both rotary and linear encoders, was not successful in achieving zero steady-state error in the final linear position. This is attributed to the imperfections in the drive's rotary to linear motion delivery, which exhibits discrepancies in the order of a few microns from the ideal model in Eq. (6.1). In order to alleviate this problem, a simpler disturbance adaptation was applied. This adaptation law uses a first order sliding surface derived considering only rigid body dynamics, observed through the linear encoder ($\sigma' = \dot{x}_{2r} - \dot{x}_2 + \lambda(x_{2r} - x_2)$). Applying this adaptation law produced much better results in terms of the final linear positioning accuracy:

$$\dot{\hat{d}} = y_2 \rho \kappa \sigma' = \frac{m_1 s_2}{m_2} \rho \kappa \left[\dot{x}_{2r} - \dot{x}_2 + \lambda(x_{2r} - x_2) \right] \tag{6.12}$$

6.2.3 State Trajectory Generation

One final requirement is the generation of state command trajectories. Since the primary objective is to have the table position (x_2) track the given motion commands (x_R), x_{2r} is chosen as:

$$x_{2r} = x_R \tag{6.13}$$

On the other hand, the ball screw rotary position (x_1) has to be offset in order to account for the axial deformations that occur during accelerations and decelerations of the drive, or when external forces are applied on the table. Writing the equation of motion for m_2,

$$m_2 \ddot{x}_2 = k(x_1 - x_2) + c(\dot{x}_1 - \dot{x}_2) - b_2 \dot{x}_2 - d \tag{6.14}$$

and assuming that $x_2 \cong x_{2r}$ and $d \cong \hat{d}$, the position command for m_1 is obtained as:

$$x_{1r} = \frac{1}{cs + k} \left[m_2 \underbrace{s^2 x_{2r}}_{\ddot{x}_{2r}} + (c + b_2) \underbrace{s x_{2r}}_{\dot{x}_{2r}} + k x_{2r} + \hat{d} \right] \tag{6.15}$$

It should be noted that the control law in Eq. (6.10) requires the computation of acceleration commands $\ddot{x}_{1r}$ and $\ddot{x}_{2r}$ while constructing the y_1 term given by Eq. (6.8). Estimation of $\ddot{x}_{1r}$ requires the original command trajectory x_R to be differentiated four times with respect to time and then low-pass filtered at a cut-off frequency of k/c (Eq. (6.15)). It is therefore necessary that a jerk continuous trajectory similar to the one in Figure 4.5 be used, in order to avoid delivering a discontinuous control signal that would excite the structural modes of the drive. In the digital implementation, numerical differentiation and integration were carried out using Euler's approximation technique ($s \cong (z-1)/(T_s z)$). A sampling frequency of 17 kHz was used, which was found to be sufficient in achieving successful vibration control on the ball screw drive.

6.3 Modeling and Compensation of Lead Errors

Using linear feedback, it is possible to detect and eliminate the positioning errors that originate from imperfections of the drive mechanism, in steady-state. The lead error is a good example of this. However, when the axis is in motion, the lead error takes the form of a sinusoidal gain variation that continuously offsets the drive's true position. In this work, for the sake of convenience in modeling and compensation, the effect of this gain variation is approximated as an output disturbance. At high speeds, the control law cannot immediately detect and compensate for the lead error, which results in the deterioration of tracking accuracy. In order to alleviate this problem, a model-based compensation strategy has been used. The lead errors were measured by moving the axis back and forth at low speeds (~10 mm/sec), to minimize the effect of elastic deformations, and estimated by taking the difference between the linear and rotary encoder readings. Measurement for 10 back and forth movements is shown in Figure 6.3. It was seen that these errors remained reasonably consistent when the measurements were taken at different times under similar conditions. Defining the ideal and actual linear positions as x_2 and x_{2a} respectively, the lead error v is expressed as:

$$v = x_{2a} - x_2 \tag{6.16}$$

For the ball screw setup, the below model was found to be adequate in describing the lead errors:

$$\hat{v}(x) = A\sin\left(\frac{2\pi}{h_p}x + \phi\right) + mx + n \tag{6.17}$$

Above, $\hat{v}$ [mm] is the modeled lead error and x [mm] is the nominal axis position. Using Least Squares [44], the model parameters were identified as $A = 1.960\times10^{-3}$ mm, $\phi = 2.0627$ rad. $h_p = 20$ mm. In the range $x < 125$ mm, $m = 0$ and $n = -0.833\times10^{-3}$ mm. For $125 \le x < 220$ mm, $m =$

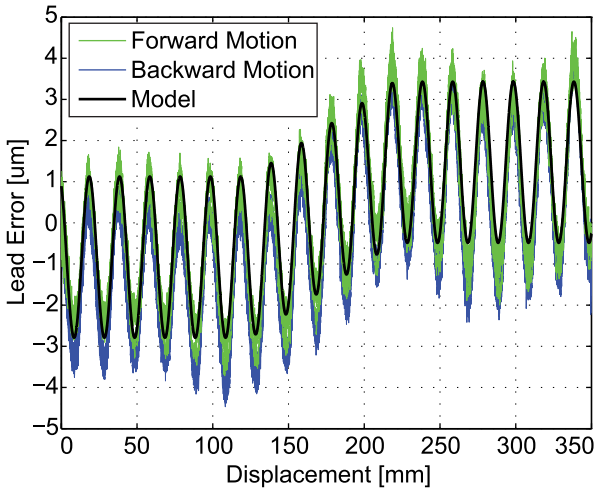

Figure 6.3: Measured and modeled lead error profiles.

2.4262×10^{-5}, $n=-3.866\text{e}\times10^{-3}$ mm. When $x \geq 220$, $m=0$, $n=1.472\times10^{-3}$ mm. While implementing this model in the control law, the displacement units were changed to radians, in order to remain consistent with the controller formulation developed in Section 6.2.

The concept of lead error compensation is illustrated with a simple example in Figure 6.4, where the effect of lead error v is removed from the loop by subtracting its predicted value $\hat{v}$ from the commanded and measured axis positions (x_r and x_a respectively). In this case, the final axis position x_a can be expressed as:

$$x_a = \underbrace{\frac{GK_{ff}}{1+GK_{fb}} \cdot x_r}_{\text{Tracking}} - \underbrace{\frac{G}{1+GK_{fb}} \cdot d}_{\text{Disturbance}} + \underbrace{\frac{1}{1+GK_{fb}} \cdot v}_{\substack{\text{Lead Error} \\ \text{Transmission}}} - \underbrace{\frac{G(K_{ff}-K_{fb})}{1+GK_{fb}} \cdot \hat{v}}_{\substack{\text{Lead Error} \\ \text{Compensation}}} \tag{6.18}$$

In a well designed controller, the tracking transfer function will be close to unity in the frequency range of most motion commands (i.e. $GK_{ff} \cong 1+GK_{fb}$). Assuming that the identified model represents the actual lead error with sufficient closeness (i.e. $\hat{v} \cong v$), it can be verified that the compensation term in Eq. (6.18) will cancel out the effect of lead errors transmitted into the servo loop, thus mitigating their effect on the dynamic performance of the drive. It can also be verified that this compensation strategy will produce the same outcome with the dual feedback control law developed in Section 6.2. LE compensation for dual control feedback is illustrated in Figure 6.5. In this case, the final axis position x_a can be expressed as:

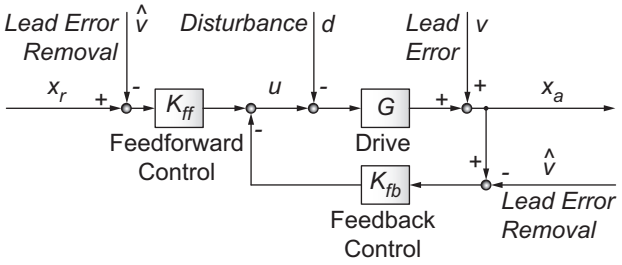

Figure 6.4: Removal of lead errors from the control loop for single axial feedback case.

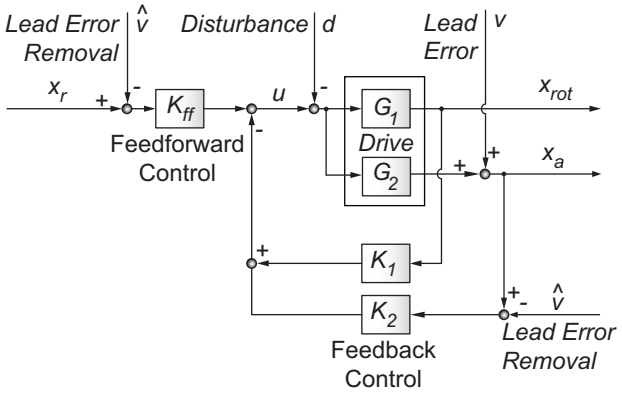

Figure 6.5: Removal of lead errors from the control loop for dual (rotary-axial) feedback case.

$$x_a = \underbrace{\frac{G_2 K_{ff}}{1+L} \cdot x_r}_{\text{Tracking}} - \underbrace{\frac{G_2}{1+L} \cdot d}_{\text{Disturbance}} + \underbrace{\frac{1+K_1 G_1}{1+L} \cdot v}_{\substack{\text{Lead Error} \\ \text{Transmission}}} + \underbrace{\frac{K_2 G_2 - K_{ff} G_2}{1+L} \cdot \hat{v}}_{\substack{\text{Lead Error} \\ \text{Compensation}}} \tag{6.19}$$

Above, $L = K_1 G_2 + K_2 G_2$. Similar to the previous case, it is assumed that $G_2 K_{ff} \cong 1 + K_1 G_1 + K_2 G_2$ and $\hat{v} \cong v$ hold, resulting in the compensation term to cancel out the lead errors transmission term.

The overall control scheme is shown in Figure 6.6. Control of rigid body motion and the 1st axial vibration mode is achieved using adaptive sliding mode control. The sliding surface was designed to yield high tracking accuracy and good disturbance rejection, while attenuating vibrations of the 1st axial mode as much as possible and avoiding the excitation of unmodeled dynamics at higher frequencies. Following trials on the experimental setup, it was seen that placing the real pole at λ =1131 rad/sec (180 Hz), and the complex conjugate poles at ω_n = 628 rad/sec (100 Hz) with ζ = 0.35 damping realized these goals. Although the damping is not very high, it is six times higher than the open loop damping of 5.6%, and is achieved through feedback control. It was observed that further increasing the pole frequencies or the damping ratio caused the control signal to become too

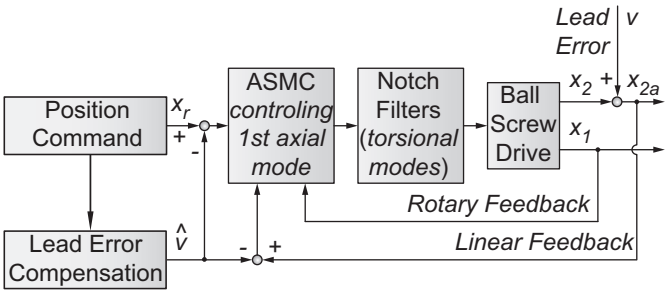

Figure 6.6: Mode compensating ASMC structure.

aggressive at high frequencies, which led to undesirable vibrations. The feedback and disturbance adaptation gains were tuned to be $K_s = 0.005$ V/(rad/sec) and $\rho = 3.3937$ V/rad.

The lead errors were compensated using the model in Eq. (6.17). Considering that this model has first order discontinuity at transition points $x =$ 125 and 220 mm, the compensation signal was low-pass filtered at 250 Hz in order to mitigate the effect of this discontinuity on the drive's performance. Notch filters were also incorporated into the control scheme, in order to avoid excitation of the 1st and 2nd torsional resonances as earlier reported in Section 4.4.1. This made vibration control of the 1st axial mode possible.

6.4 Experimental Results

The proposed control scheme has been evaluated in frequency response and high speed tracking experiments conducted on the ball screw drive. In frequency response tests, the mode compensating controller has been compared to an alternative design consisting of notch filtering the 1st axial mode and using an ASMC designed only for rigid body dynamics. This controller was implemented earlier in Section 4.6.2, where the loop was closed using only linear encoder feedback. In this case, the sliding surface bandwidth could be increased only up to $\lambda =$ 440 rad/sec (70 Hz). The sampling frequency in both implementations was 17 kHz.

6.4.1 Frequency Response Measurements

Experimentally measured FRF's comparing the tracking performance of the two controllers are shown in Figure 6.7. It can be seen that the mode compensating controller has wider usable frequency range, where the gain drops below -3 db after 208 Hz. The -3 db drop occurs at 113 Hz for the rigid body based ASMC, which indicates a two-fold bandwidth difference. In addition, the gain of the mode compensating ASMC (MC-ASMC) is closer to unity and its phase lag is considerably lower (less than 30°) up to 170 Hz, indicating a more favorable tracking performance.

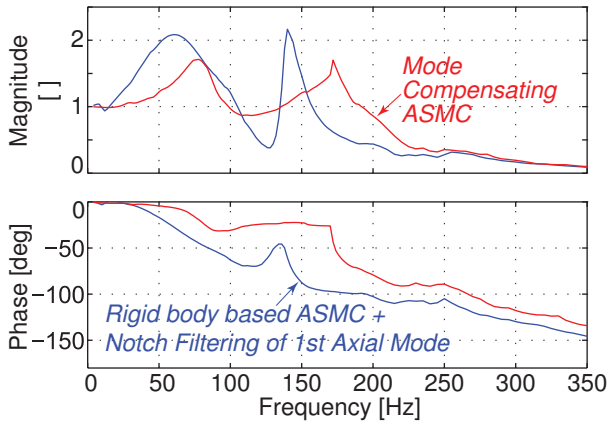

Figure 6.7: Experimental FRF's for linear positioning.

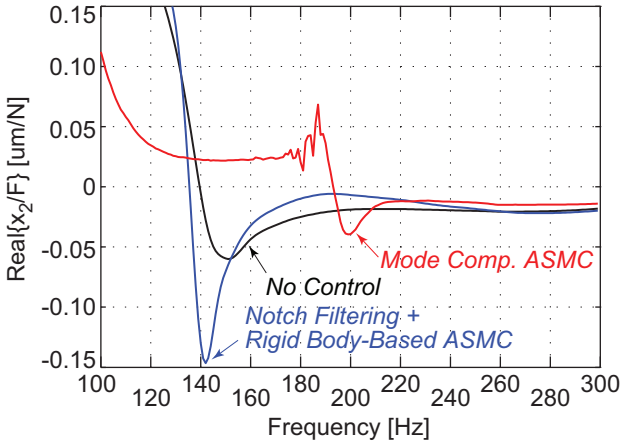

Figure 6.8: Disturbance transfer functions measured by hammer tests.

Disturbance transfer functions were measured by impact hammer testing, in order to compare the cutting force sensitivity of the mode compensating controller with the rigid body based ASMC. Figure 6.8 shows the real component of the measured disturbance transfer functions around the 1st axial resonance. Negative real values with larger magnitude, for this transfer function, indicate higher susceptibility to chatter vibrations during machining [3]. In the case with no control, the minimum real component of the disturbance transfer function is -0.06 um/N. Rigid body based ASMC with notch filtering worsens the sensitivity around the axial mode, resulting in a minimum real component equal to -0.150 um/N. The mode compensating ASMC yields the least sensitive case, with the minimum real component of the dynamic compliance reducing to -0.040 um/N. This makes this controller more favorable in terms of reducing the ball screw drive's susceptibility to chatter vibrations, by injecting additional damping around the first axial resonance frequency.

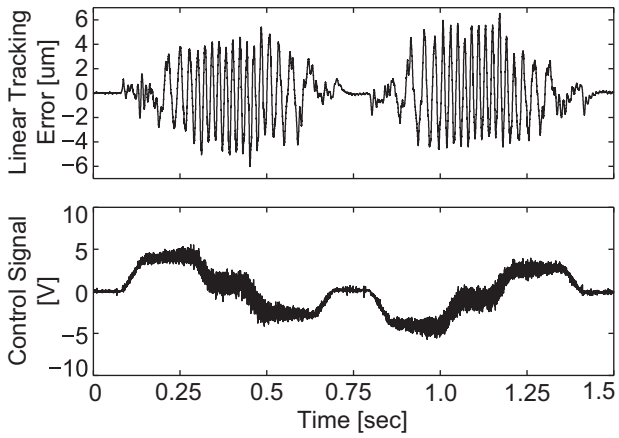

Figure 6.9: Tracking performance of MC-ASMC without lead error correction.

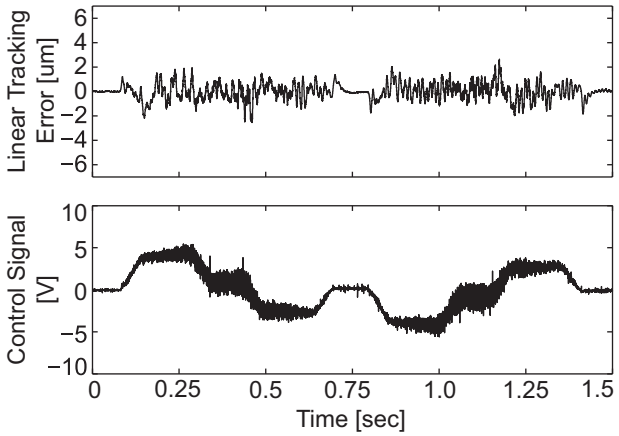

Figure 6.10: Tracking performance of MC-ASMC with lead error correction.

6.4.2 High Speed Tracking Results

The performance of the mode compensating ASMC was verified in high speed tracking experiments. Earlier in Section 4.6.2, it was seen that for a jerk continuous trajectory with 350 mm displacement, 1000 mm/sec feed, 5000 mm/sec^2 acceleration, and 100,000 mm/sec^3 jerk, the rigid body based ASMC with notch filtering could only achieve a linear tracking accuracy around 24 um. By increasing the sampling frequency to 17 kHz and tuning this controller further, it was possible to bring the tracking error down to 9.2 um. However, this over tuning resulted in distortions in the command following FRF, with magnitudes reaching as high as 4.6. This is highly undesirable in terms of the tracking accuracy. Also, it is an indication of poor robustness margins due to severe peaks in the sensitivity and complementary sensitivity functions [58].

The tracking performance of the mode compensating ASMC (MC-ASMC) was evaluated without and with lead error compensation. Results of these tests are shown in Figure 6.9 and Figure 6.10.

When lead error compensation is not used, a linear tracking accuracy of 6.5 um is maintained, as seen in Figure 6.9. This is better than the accuracy achieved with rigid body based ASMC and notch filtering of the 1st axial mode. Furthermore, the closed loop frequency response is not distorted due to over tuning. The effect of lead errors can clearly be seen in the tracking error profile, as if a sinusoidal disturbance is being applied at the drive's output. When lead error compensation is enabled (Figure 6.10) the tracking error is further reduced to 2.6 um, indicating an overall improvement in the drive's dynamic accuracy, which is achieved with the proposed controller design.

6.5 Stability Analysis

The results of obtained with the mode compensating ASMC are highly promising in terms of augmenting the positioning accuracy and dynamic stiffness of ball screw drives. However, one drawback with this controller is its complexity, which requires the designer to select 3 pole locations for the sliding surface (using λ, ω_n, ζ), and to tune two controller gains (K_s and ρ). During experimental implementation of the controller, it was seen that the selection of these parameters was not a trivial task. If the model pole locations or feedback gain are not determined correctly, this may result in overly aggressive control signals, which can excite the unmodeled dynamics (such as torsional or higher order axial modes etc.), and cause instability. In the controller design, although the first axial mode was considered in the plant model, and therefore the Lypunov stability analysis, the influence of torsional modes and current loop dynamics were not taken into account. These dynamics can lead to instability due to the additional phase lag and gain amplification (i.e. resonances) they contribute to the loop dynamics. These factors have to be carefully considered in selecting the mode compensating ASMC parameters. Therefore, in this section, a stability analysis of the mode compensating ASMC is conducted. In the analysis, Nyquist's stability criterion has been used. The presented approach can be used as a tuning tool to aid in the selection of controller parameters to yield certain phase and gain margins, and/or sensitivity peak values. Since lead error compensation is realized only in feedforward, its effect is not included into the stability analysis.

The block diagram for the mode compensating ASMC system can be represented as shown in Figure 6.11(a), with a feedforward filter ($K_{ff}(s)$) and two feedback filters ($K_1(s)$ and $K_2(s)$) which generate the control signal (u_{smc}) based on the position command (x_{2r}), rotary encoder reading (x_1), and linear encoder measurement (x_2), in the mentioned order. Although the plant (drive system) has one input and two outputs, the analysis can been simplified by combining both feedback channels into a single loop, since there is only one control input. This is done by applying the block

diagram manipulation shown in Figure 6.11(b), where the feedback filters are shifted to be right after the plant outputs. The resulting feedback control signal can be expressed as:

$$u_{fbk} = \underbrace{(K_1 G_1 + K_2 G_2)}_{L:\text{Loop Transfer Function}} \quad (K_{ff} x_{2r} - u_{fbk}) \Rightarrow (1+L) u_{fbk} = L K_{ff} x_{2r} \tag{6.20}$$

The stability of the closed loop system can be analyzed by inspecting the Nyquist plot for the loop transfer function:

$$L = K_1 G_1 + K_2 G_2 \tag{6.21}$$

Assuming that the feedforward filter $K_{ff}(s)$ and the inverse of the filters $(1/K_1(s),\ 1/K_2(s))$ are stable, the stability of the system depends on the stability of $(1+L(s))^{-1}$.

In computing the loop transfer function frequency response, the plant related terms G_1 and G_2 were obtained by multiplying the experimentally measured open loop position FRF's with the dynamics of the notch filters that were designed for the torsional modes. The drive's acceleration response, relating the control input to the rotary and linear accelerations, was shown in Figure 3.16. The position FRF's were constructed by multiplying these graphs with $1/(j\omega)^2$. The notch filters, on the other hand, have been described in Section 4.4.1. Here, the notch filters have been slightly retuned and the discrete-time parameters were updated to accommodate the new sampling frequency of 17 kHz. Using experimentally recorded FRF's for the plant, as done here, allows for the influence of additional dynamics, such as the torsional modes or the current loop, to be realistically incorporated into the stability analysis.

According to the block diagram in Figure 6.11(a), u_{smc} can be expressed as:

$$u_{smc} = K_{ff}(s) x_{2r} - K_1(s) x_1 - K_2(s) x_2 \tag{6.22}$$

The control law for u_{smc}, given in Eq. (6.10), can be transformed to the structure in Eq. (6.22) by substituting the expressions for σ from Eq. (6.5), $\hat{d}$ from Eq. (6.12), y_1 and y_2 from Eq. (6.8), and x_{1r} from Eq. (6.15). Organizing the terms yields the following expressions for $K_{ff}(s)$, $K_1(s)$, and $K_2(s)$:

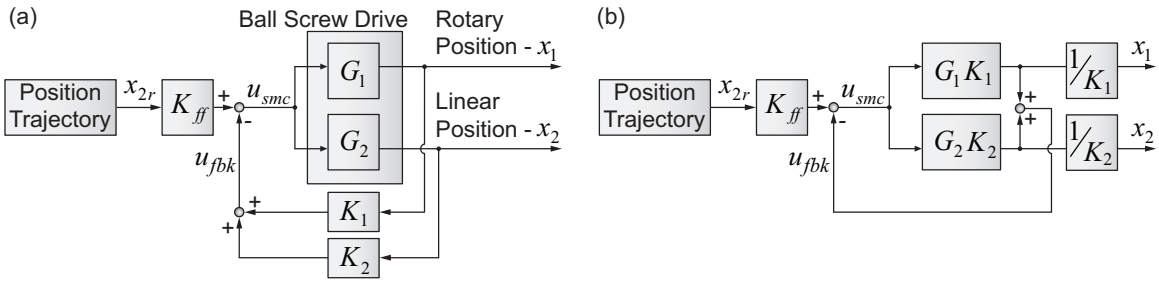

Figure 6.11: MC-ASMC block diagram: (a) Feedforward and feedback transfer functions, (b) Rearranged to obtain the loop transfer function.

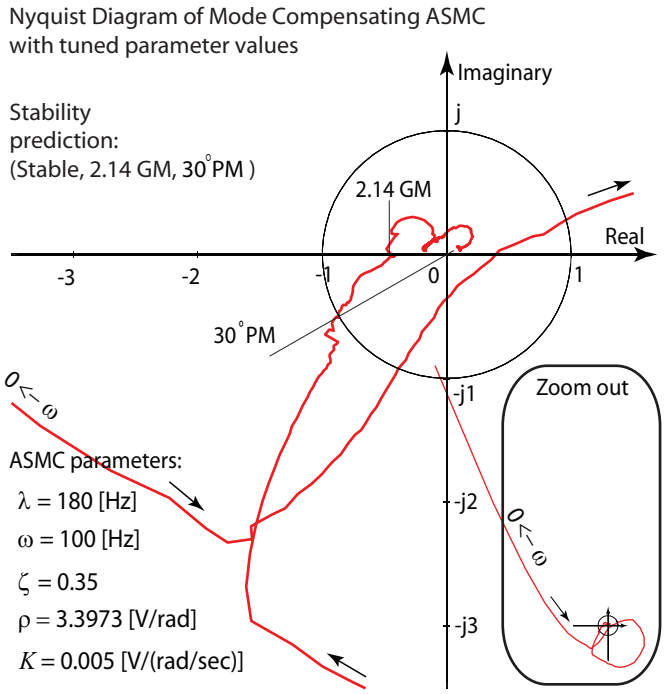

Figure 6.12: Nyquist diagram of mode compensating ASMC used in tracking experiments.

$$K_{ff}(s) = \frac{\alpha_0 s^5 + \alpha_1 s^4 + \alpha_2 s^3 + \alpha_3 s^2 + \alpha_4 s + \alpha_5}{m_2^2 s(cs+k)},$$
$$K_1(s) = \beta_0 s + \beta_1,\ K_2(s) = \frac{\gamma_0 s^3 + \gamma_1 s^2 + \gamma_2 s + \gamma_3}{m_2^2 s(cs+k)} \tag{6.23}$$

The coefficients were determined using the Matlab's Symbolic Math Toolbox [63] as follows:

$$
\left.
\begin{aligned}
\alpha_0 &= m_1 m_2^3 \\
\alpha_1 &= m_2^2\{m_1[b_2+c(s_2+1)+m_2 s_3]+K_s m_2\} \\
\alpha_2 &= K_s m_2^2[m_2 s_3+c(1+s_2)+b_2]+\rho m_1^2 m_2 s_2+m_1 m_2^2[b_2 s_3+c(s_1+s_3)+k(1+s_2)] \\
\alpha_3 &= m_2^2\{K_s[(b_2+c)s_3+cs_1+k(1+s_2)]+m_1 k(s_3+s_1)\}+\rho K_s m_1 m_2 s_2+\rho m_1^2[m_2(\lambda+s_3)+cs_2]s_2 \\
\alpha_4 &= K_s m_2^2 k(s_1+s_3)+\rho K_s m_1 m_2 s_2(s_3+\lambda)+\rho m_1^2[\lambda(m_2 s_3+cs_2)+ks_2]s_2 \\
\alpha_5 &= \rho\lambda m_1(m_1 k s_2+K_s m_2 s_3)s_2 \\
\\
\beta_0 &= K_s - b_1 + m_1(s_3 + s_2 c/m_2) - c \\
\beta_1 &= K_s s_3 + (m_1 s_2 / m_2 - 1)k \\
\\
\gamma_0 &= m_2^2[m_1 s_1 + K_s s_2 + c]c + m_1 m_2[m_1\rho - c(b_2 + c)]s_2 \\
\gamma_1 &= m_2^2[k(m_1 s_1 + K_s s_2 + 2c) + K_s c s_1] + m_1 m_2\{\rho[m_1(s_3+\lambda)+K_s]\ldots \\
&\quad - k(b_2 + 2c)\}s_2 + \rho m_1^2 c s_2^2 \\
\gamma_2 &= m_2^2 k(K_s s_1 + k) + m_1 m_2\{\rho[K_s(\lambda + s_3) + \lambda m_1 s_3] - k^2\}s_2 + \rho m_1^2(k+\lambda c)s_2^2 \\
\gamma_3 &= \rho\lambda m_1(m_1 k s_2+K_s m_2 s_3)s_2
\end{aligned}
\right\} \qquad (6.24)
$$

The frequency response of the control filters was calculated by substituting $s \to j\omega$ inside the expressions for $K_1(s)$ and $K_2(s)$ in Eq. (6.23) and (6.24). The loop transfer function $L(j\omega)$ was computed by numerically combining the controller and plant dynamics using Eq. (6.21). The Nyquist plot for the MC-ASMC used in tracking experiments is shown in Figure 6.12, which verifies the stability of the designed controller with a gain margin of 2.14 and a phase margin of 30°.

In order to validate the performed stability analysis, more tracking tests were conducted with different sets of control parameters, resulting in marginally stable to unstable cases. As shown in Figure 6.13 through Figure 6.16, both the Nyquist diagrams and the tracking profiles are in close agreement on the stability of the closed loop system. This is true even in borderline cases where the Nyquist plot passes very close to the -1 point. When the Nyquist plot predicts instability, this is also validated experimentally in the form of severely large and oscillatory tracking errors and highly aggressive control signals. Overall, the experimental results indicate that the developed stability analysis can be used reliably in predicting the outcome of the MC-ASMC parameter selection.

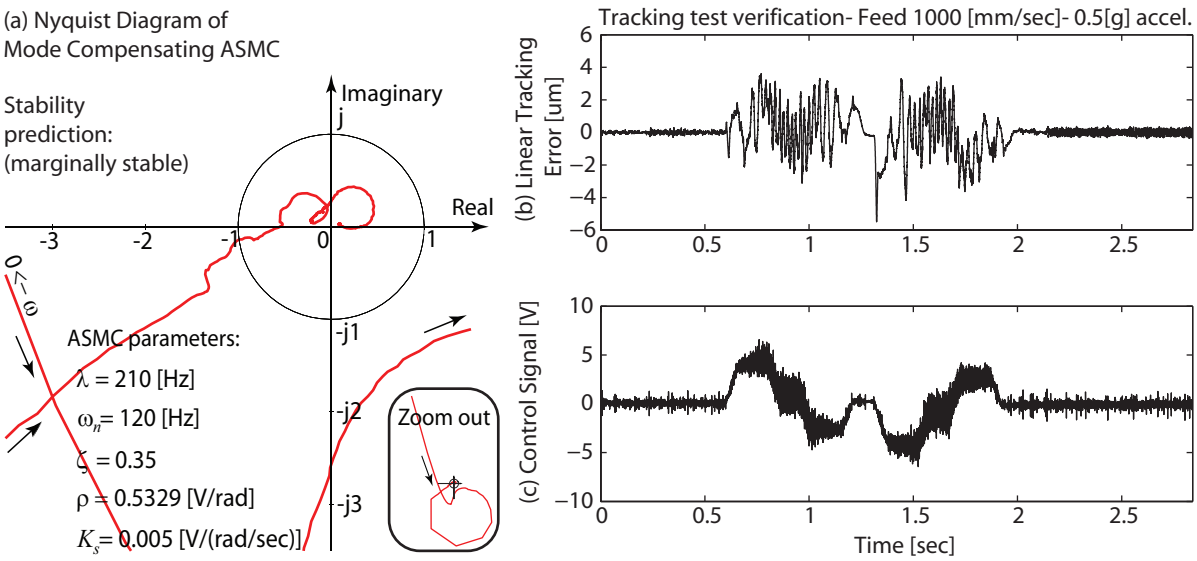

Figure 6.13: Stability of MC-ASMC: Marginally stable case. (a) Nyquist prediction, (b) Tracking error, (c) Control signal.

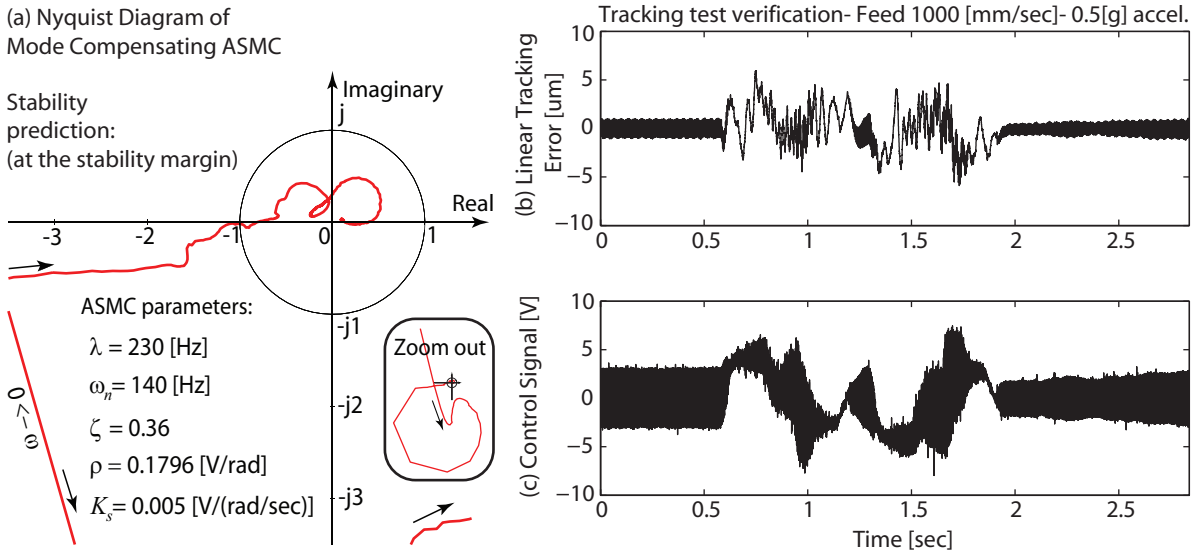

Figure 6.14: Stability of MC-ASMC: At the stability margin. (a) Nyquist prediction, (b) Tracking error, (c) Control signal.

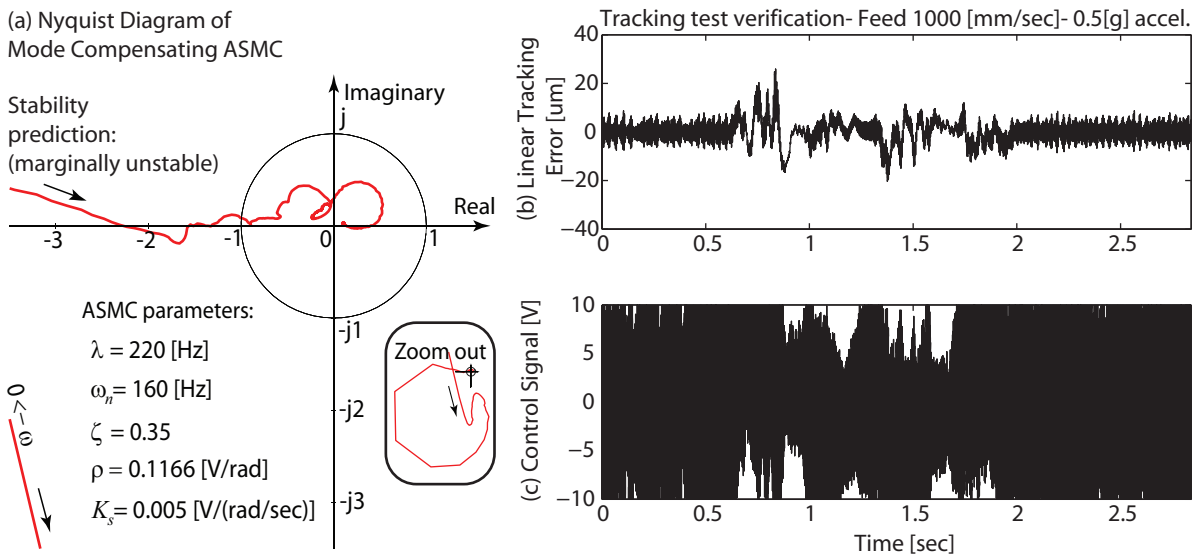

Figure 6.15: Stability of MC–ASMC: Marginally unstable case. (a) Nyquist prediction, (b) Tracking Error, (c) Control Signal.

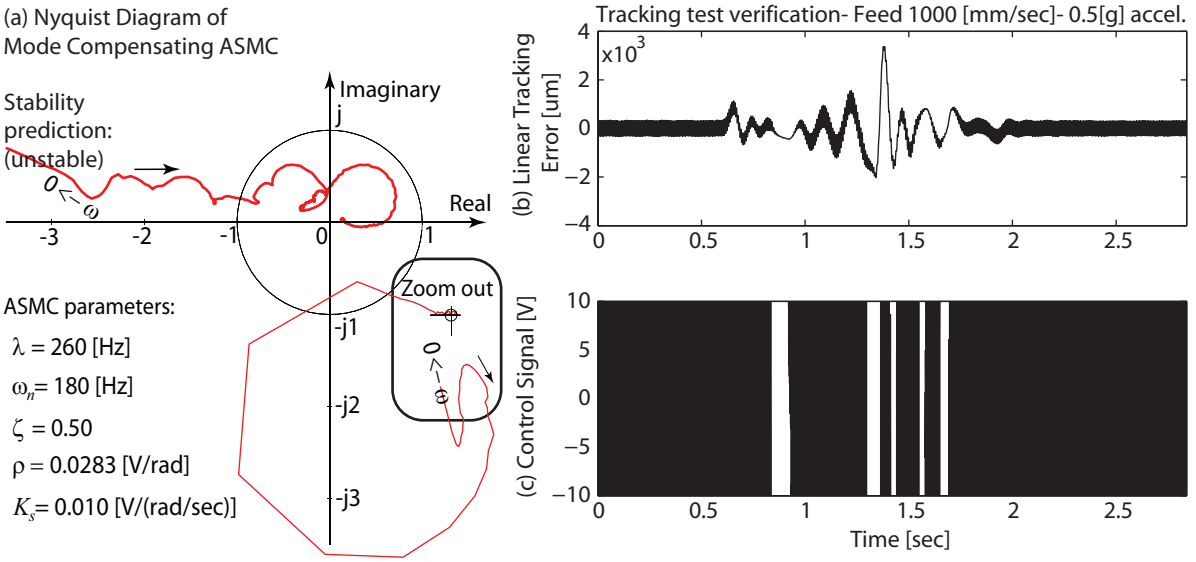

Figure 6.16: Stability of MC-ASMC: Unstable case. (a) Nyquist prediction, (b) Tracking error, (c) Control signal.

6.6 Limitations

The presented mode compensating ASMC was found to be very effective in suppressing the 1st axial mode of the high speed ball screw drive. However, its limitations also need to be mentioned. It requires elaborate tuning of more control parameters, compared to the rigid body-based design. Also, high resolution feedback from both rotary and linear encoders are required, as well as a high sampling frequency. Since the dynamics of the 1st axial mode are incorporated into the plant model in the

controller design, large deviations of the actual dynamics from the nominal model may limit the controller performance or even cause instability. Hence, the controller needs to be tuned considering an envelope of possible frequency response characteristics for the drive system. Finally, the two-mass lumped model captures only the phase lag originating from the 1st axial mode. Additional phase lag due to the amplifier dynamics and other resonance modes will limit the achievable control bandwidth. Hence, these points need to be kept in mind when implementing the mode compensating ASMC on ball screw drives.

6.7 Conclusions

This chapter has presented a new approach in controlling ball screw drives through the application of active vibration damping using Adaptive Sliding Mode Control. It is shown that the mode compensating ASMC is capable of achieving significantly higher positioning bandwidth and dynamic stiffness, compared to the traditional practice of notch filtering the axial vibration inside the control loop. The mode compensating ASMC (MC-ASMC) can be practically implemented in real-time using a rotary and linear position feedback configuration, which is available on most drive systems. Since the state variables are the rotary and linear position and velocity, there is no need to construct an elaborate state observer. This decreases the computational load and makes the control law favorable for real-time implementation.

Lead errors, which originate from the imperfections of the ball screw, have also been modeled and compensated in feedforward. It can be expected that as the thermal state of the ball screw changes, the lead error cancellation will become less accurate. However, this issue has been kept outside the scope of this thesis. The main reason for lead error compensation in this chapter was to investigate the ideal tracking performance that could be achieved with MC-ASMC, if the motion transmission in the ball screw was near-perfect.

Overall with the MC-ASMC, an experimental command following bandwidth of 208 Hz has been verified, which is several-fold higher than typical positioning bandwidths (30-50 Hz) achieved on ball screw drives. After the implementation of lead error compensation, a tracking accuracy of 2.6 um has been maintained while traversing the axis at 1000 mm/sec feed with 0.5 g accelerations. Through impact hammer tests, it is also shown that the MC-ASMC helps to improve the dynamic stiffness around the axial mode, rather than to degrade it, which is what happens when the notch filter based rigid body ASMC is used.

Although the MC-ASMC yields highly promising results, tuning its gains is not a trivial task. There are several parameters that need to be selected. Also, the additional dynamics which were not

considered in the plant model (i.e. the current loop and torsional modes) can have a major impact on the closed loop stability. Hence, a stability analysis has been conducted using Nyquist's Theorem, which combines experimentally recorded FRF's of the ball screw with the frequency response of the feedback control filters. It is shown that this analysis can be reliably used in stability predictions and in parameter selection when tuning the mode compensating ASMC.

Chapter 7
Modeling and Compensation of Elastic Deformations

7.1 Introduction

In Chapter 6, a technique was developed to handle the axial vibrations, allowing high positioning accuracy to be achieved using rotary and linear position feedback in the control law. In this chapter, a different approach is taken to achieve the same purpose. Rather than trying to implement active vibration suppression, the quasi-static elastic deformations of the ball screw are modeled and compensated. Both feedforward and feedback techniques are investigated. Essentially, the compensation considers the low frequency portion of the axial dynamics that were identified in Chapter 6. Although, the feedforward method is simpler to implement, it is shown that the feedback approach yields higher robustness against dynamic variations and disturbances on the load side. This is because the feedback approach continuously monitors the real-time control signal, and implicitly estimates any additional elastic deformation that is caused by such perturbations. The proposed ED compensation strategies substantially improve the linear positioning accuracy of ball screw drives that are controlled using only rotary feedback. These methodologies also yield a performance improvement in ball screw drives with combined rotary and linear position feedback, by forcing the controller to react faster to compensate for the drive's anticipated elastic deformations.

In the two proposed techniques, the ED is estimated by dividing the torque transmitted to the table with the equivalent axial stiffness of the drive. The position loop is closed using rotary feedback from Encoder 2, which has smaller phase lag compared to the position measurements from the linear encoder (Figure 3.16). Also this feedback channel is influenced less by the 1st axial mode. This enables a high control bandwidth to be achieved using the rigid body based ASMC in conjunction with notch filters for the torsional modes. The rotary position commands are offset to account for the anticipated elastic deformation, so that the final linear position of the table is realized correctly.

Alongside ED compensation, lead errors (LE) are also modeled and compensated in the control signal. ED and LE compensation is implemented in conjunction with ASMC, which fulfills the basic servo function. The ASMC is designed to utilize either only rotary feedback, or combined rotary and linear position feedback, in order to achieve a high command following bandwidth and as well as high linear positioning accuracy. The methodology developed in this chapter can also be applied on feed drive systems which only have a rotary encoder mounted on the motor.

The remainder of this chapter is organized as follows. The ED and LE models are developed in Section 7.2. Feedforward and feedback ED compensation strategies are presented in Section 7.3 and Section 7.4, respectively. In Section 7.4.4, stability analysis is performed to ensure that the adequate gain and phase margins are still maintained when applying ED compensation in feedback. Experimental results demonstrating the effectiveness of the proposed ED and LE compensation strategy are presented in Section 7.5, and the conclusions for this chapter are presented in Section 7.6.

7.2 Modeling of Elastic Deformations and Lead Errors

There are several factors which influence the rotary to linear motion transmission in ball screw drives. One of the dominant factors is the elastic deformation, which is studied in this chapter. Occurring simultaneously with elastic deformations are lead errors arising from manufacturing imperfections of the ball screw [59], motion loss in the preloaded nut which is observed as nut backlash [11], and thermal expansion errors [26] which originate from the temperature rise due to contact friction in the ball screw-nut interface. Due to their complex and nonlinear nature, thermal deformations have been kept outside the scope of this work. Various studies have been conducted in the literature to model and compensate for their effects [13][26]. Lead errors and backlash, on the other hand, exhibit a reasonably consistent behavior and are easier to take into account in the controller design, as done in the work presented here.

7.2.1 Lead Errors and Backlash

The lead error (LE) model presented in Chapter 6 is developed further here, by considering the positive and negative directions of motion which account for the backlash-like effect observed in the preloaded nut. Lead errors, backlash, and elastic deformations exhibit themselves in a combined manner, causing the majority of the discrepancy observed between the rotational motion of the screw, and linear motion of the nut.

A schematic representation of the ball screw setup is shown in Figure 7.1(a). The rotary position measurement is registered from Encoder 2, denoted with x_{rot} [mm]. Rotary readings have been scaled to correspond to the equivalent table motion, by making use of the ball screw pitch length (i.e. 1 rev = 2π rad = 20 mm). The table position measurement is obtained from the linear encoder, shown with x_{lin} [mm]. During slow movements at a constant speed, the discrepancy between rotary and linear readings is accounted to the combined effect of lead errors, nut backlash, and a small amount of elastic deformation that would occur in order to counteract the sliding friction in the linear guideways. As mentioned earlier, the effect of thermal deformations have been kept outside the scope

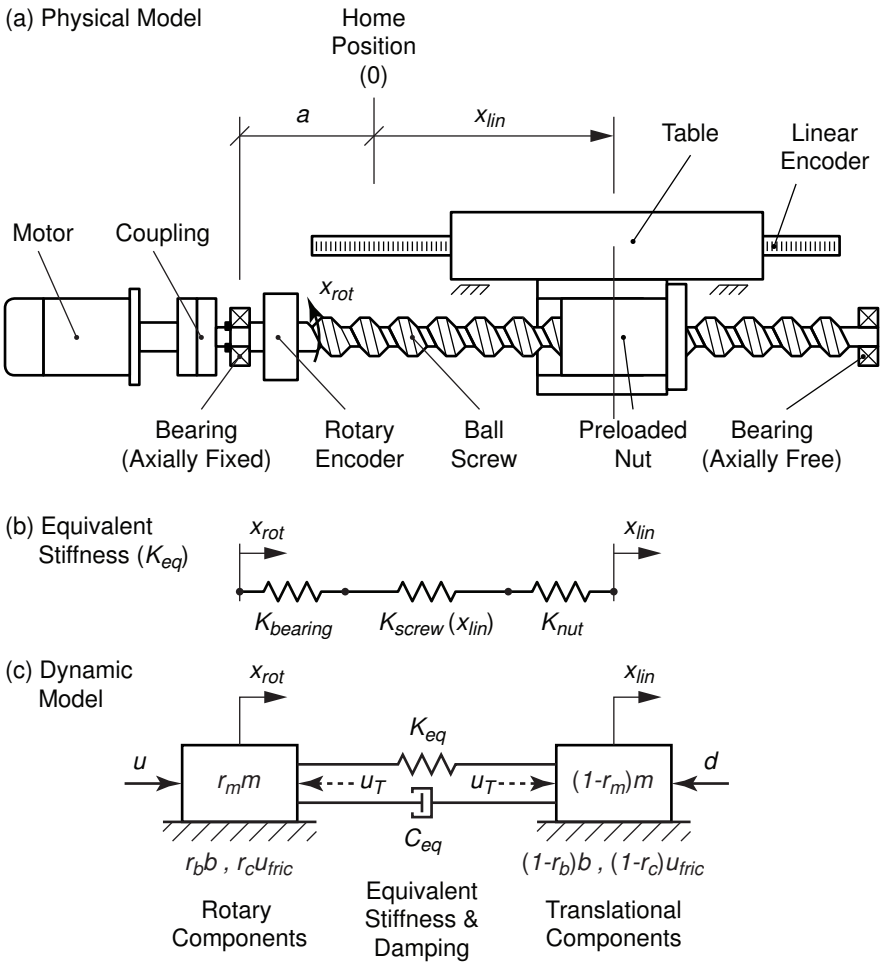

Figure 7.1: Schematic of ball screw for modeling elastic deformations.

of this study. In either case, during slow movements the temperature rise due to nut friction, and therefore the thermal expansion of the ball screw, will be minimal. On the other hand, since the setup uses air bushings the effect of elastic deformation due to sliding friction on the load side can also be neglected. In conventional drives with lubricated or roller guideways, this effect can be incorporated into the elastic deformation model during the parameter identification process, which is explained in Section 7.4.2.

The lead error model is constructed by jogging the drive back and forth at a moderately low speed and logging the difference between the linear and rotary encoder readings. In the setup, which has air guideways and a maximum travel velocity of 1000 mm/sec, it was found that performing the jogging at 80 mm/sec was sufficiently slow for obtaining a good measurement of the lead error. On a conventional machine tool, this measurement can be realized in a lower speed range, such as 10-50 mm/sec. The lead error (LE) is estimated as:

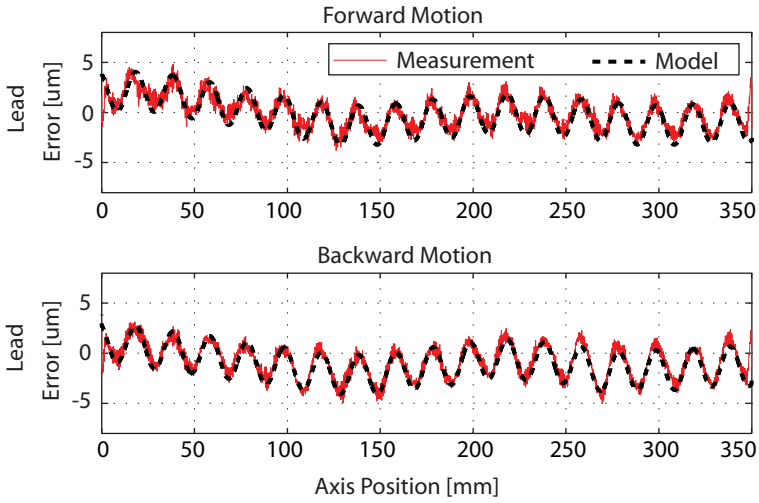

Figure 7.2: Measured and modeled lead errors.

$$LE = x_{lin} - x_{rot} \tag{7.1}$$

The LE was observed to exhibit a repeating sinusoidal pattern with a position dependent offset, as shown in Figure 7.2. Its overall shape is captured with the below model:

$$LE(x) = A\sin(\frac{2\pi}{h_p}x + \phi) + c_0 x + c_1 \tag{7.2}$$

Above, x [mm] represents the nominal axis position. A [mm] is the magnitude of the lead error, h_p = 20 mm is the ball screw pitch, and ϕ helps to adjust the position phasing. Using Least Squares technique [44], the amplitude and phase values were identified to be A =1.987 um, and ϕ =2.079 rad. If necessary, the parameters A and ϕ can be made to be position dependent in order to reflect the variability of lead along long ball screw drives. c_0 and c_1 are linear interpolation parameters for adjusting the position dependent offset. They are calculated from a look-up table comprising of average offset values to be applied for each revolution of the ball screw, as summarized in Table 5.1. Considering the data in the table, it can be seen that there is on average 0.75 um difference between the offsets in the forward and backward directions, which captures the motion loss (i.e. backlash effect) in the preloaded nut.

In the control scheme, the predicted lead error values are used to offset the trajectory commands in order to realize the linear motion of the table correctly. To avoid causing unwanted feedback loops, the nominal axis position x in Eq. (7.2) is replaced by the commanded position value x_r when implementing the lead error compensation. Due to the piecewise linear approximation of the lead offsets, the lead error estimate calculated using Eq. (7.2) is only C^0 (i.e. position) continuous. Most

Table 7.1: Experimental data used in constructing the lead error offset look-up table.

Nominal Position x [mm]	-9	11	31	51	71	91	111	131	151
Forward Motion Average Lead Error $LE(x)$ [um]	2.105	2.105	2.028	1.289	0.638	0.094	-0.761	-1.296	-1.247
Backward Motion Average Lead Error $LE(x)$ [um]	1.060	1.060	0.312	-0.045	-0.644	-1.215	-1.736	-2.160	-2.058

. . .

Nominal Position x [mm]	171	191	211	231	251	271	291	311	331	351
Forward Motion Average Lead Error $LE(x)$ [um]	0.771	-0.505	-0.062	-0.219	-0.494	-0.880	-1.262	-1.237	-0.999	-0.999
Backward Motion Average Lead Error $LE(x)$ [um]	1.556	-1.105	-0.511	-0.768	-1.037	-1.899	-1.677	-1.674	-1.304	-1.304

CNC controllers use feedforward dynamic compensation in order to achieve accurate command tracking, which requires the position commands to be differentiated with respect to time. In order to avoid severe discontinuities in the control signal due to this differentiation, the lead error compensation values were passed through a 1st order low-pass filter with a cutoff frequency of 80 Hz, which provided sufficient smoothening before applying the corrected trajectory commands to the axis controller.

7.2.2 Elastic Deformations

There are several factors that influence the equivalent axial stiffness of a ball screw drive. In particular, this stiffness originates from the stiffness characteristics of the ball screw, the preloaded nut, and the thrust bearing(s). In addition, the preloaded nut serves as a special spring that couples different degrees of freedom together, especially in the torsional and axial directions of motion. Detailed Finite Element and hybrid simulation studies have been conducted to analyze and simulate these effects through rigorous theoretical analyses [49][68][71]. In order to employ these methods successfully, a profound understanding of the Finite Element theory, dynamic model reduction, and advanced simulation techniques is required. Also, detailed knowledge of the individual component stiffness and inertia values are needed, which may be difficult to measure on existing machine tool drives.

For an elastic deformation model to be used in the CNC for real-time compensation, it needs to be as simple and intuitive as possible, and its parameters should be easy to identify or tune. In the following, such a model is developed for predicting the equivalent axial elastic deformation in ball screw drives. The model successfully captures the position dependent stiffness behavior.

Considering the schematic representation of the ball screw drive in Figure 7.1(a), the actuation torque that is transmitted to the table passes through the screw's active length, shown as $a + x_{lin}$, where a is the distance between the fixed bearing location and the axis "home position", and x_{lin} is the table linear position referenced according to the drive's home position. There are three main components that contribute to the stiffness of the ball screw within its active length. These are the axially fixed bearing, the screw itself, and the ball screw-nut interface. The stiffness of these elements are represented with three springs connected in series, as shown in Figure 7.1(b). $K_{bearing}$ represents the bearing stiffness, and K_{nut} represents the equivalent axial stiffness at the preloaded nut interface. K_{screw} represents the equivalent stiffness contributed by the screw itself. The coupling between the torsional and axial deformations, and the effect of torsional winding and unwinding of the screw on its axial length, are also considered to be lumped into these parameters. It should be noted that $K_{screw}(x_{lin})$ is dependent on the axial position of the table (x_{lin}) along the ball screw. Hence, the equivalent axial stiffness K_{eq} which transmits the actuation torque to the table is expressed as:

$$\frac{1}{K_{eq}} = \frac{1}{K_{bearing}} + \frac{1}{K_{screw}(x_{lin})} + \frac{1}{K_{nut}} \tag{7.3}$$

Considering that the ball screw has a uniform outer diameter along its threaded length, the screw's equivalent axial stiffness can be expressed in the form:

$$K_{screw}(x_{lin}) = \frac{K}{a + x_{lin}} \tag{7.4}$$

Above, $1/K$ is the unit flexibility per active length of the ball screw. By substituting Eq. (7.4) into Eq. (7.3), the drive's equivalent axial flexibility (i.e. inverse of stiffness), can be expressed as follows:

$$\frac{1}{K_{eq}} = \underbrace{\frac{K_{bearing} + K_{nut}}{K_{bearing} K_{nut}} + \frac{a}{K}}_{p_1} + \underbrace{\frac{1}{K}}_{p_2} x_{lin} = p_1 + p_2 x_{lin} \tag{7.5}$$

In the above model, the parameters p_1 and p_2 are experimentally identified. The transmission of motion through the equivalent stiffness chain, from the rotating components of the drive mechanism

to the translating components (i.e. nut and table assembly) is depicted with a simplified dynamic model, which is shown in Figure 7.1(c). This is similar to the model used to capture the axial vibrations in Chapter 6. The model parameters have been normalized in terms of the control signal u [V], which corresponds to the actuation torque. The total mass (m), viscous damping (b), and nonlinear Coulomb friction (u_{fric}) characteristics were identified earlier in Chapter 3. r_m is the mass distribution ratio for the rotational components and has to satisfy $0 < r_m < 1$. Intuitively, since the actuation is transmitted from the rotating elements to the translating components, $r_m m$ represents the total inertia of the rotating components (i.e. motor, coupling, bearings, and ball screw.), and $(1-r_m)m$ represents the total inertia of the translating components (i.e. table and nut assembly). Similarly, the total viscous friction has been distributed between the rotational and translational sides of the drive mechanism as $r_b b$ and $(1-r_b)b$ respectively, where $0 \le r_b \le 1$. The Coulomb friction has also been distributed between the rotational and translational parts of the drive with the factor $r_c \in [0, 1]$. This approximation assumes that the Coulomb friction characteristics on the rotating and translating sides have the same function shape. Although this approximation will not always exactly hold, the steady-state (high velocity) Coulomb friction values will still be captured correctly, which allows the elastic deformation model to be reasonably accurate for real-time trajectory correction. The actuation torque that is transmitted to the table through the equivalent axial stiffness (K_{eq}) and damping (C_{eq}) elements has been denoted with u_T. The equivalent damping coefficient C_{eq} represents primarily the energy dissipation in the nut interface. Although this parameter is important when the axial vibrations of the ball screw are of concern, it does not have too much practical significance in predicting the elastic deformation of the drive mechanism, which is more quasi-static in nature compared to the structural vibrations. Lastly, d represents the effect of external disturbances including cutting forces, and the lumped effect of changes in the dynamic parameters (like table mass and guideway friction) on the load side. Ultimately, these effects would need to be detected and accounted for in the elastic deformation model in real-time. The elastic deformation is estimated by dividing the transmitted torque by the equivalent axial stiffness,

$$ED = \frac{u_T}{K_{eq}} \tag{7.6}$$

The u_T term, which represents the transmitted actuation torque that causes the elastic deformation, can be calculated in two different ways leading to two different approaches that are developed in the

following sections. These are the feedforward (open loop) approach and the feedback (closed-loop) technique.

7.3 Elastic Deformation Compensation in Feedforward

In the feedforward (open loop) elastic deformation compensation strategy [33], the control signal equivalent torque (u_T) transmitted through the nut is computed by considering the nominal torque required to actuate the translating components of the ball screw mechanism:

$$u_T = (1 - r_m)m\ddot{x}_r + (1 - r_b)b\dot{x}_r + (1 - r_c)u_{fric} \tag{7.7}$$

The control signal applied for feedforward friction compensation (u_{fric}) is also purely in open loop. The ED value is computed by dividing the transmitted torque estimate (u_T from Eq. (7.7)) with the equivalent axial stiffness (K_{eq} from Eq. (7.5)), resulting in:

$$ED = [(1 - r_m)m\ddot{x}_r + (1 - r_b)b\dot{x}_r + (1 - r_c)u_{fric}](p_1 + p_2 x_r) \tag{7.8}$$

The realized compensation is shown in Figure 7.3. The ED estimate is combined with the predicted lead error (LE) value in generating the corrected rotational position command (x_{cr}):

$$x_{cr} = x_r + ED - LE \tag{7.9}$$

This trajectory is fed to the rigid body based ASMC, developed in Chapter 4, in which the position loop is closed with Encoder 2. If direct linear position measurement (x_{lin}) is also available, the same control law is used with the following modification for the disturbance adaptation law:

$$\dot{\hat{d}} = \rho\kappa\sigma_{lin} = \rho\kappa[\dot{x}_r - \dot{x}_{lin} + \lambda(x_r - x_{lin})] \tag{7.10}$$

This case is depicted with the dotted linear feedback line in Figure 7.3.

Although the feedforward compensation technique is simple to implement, it can be expected that its accuracy will deteriorate when there are external disturbances (i.e. cutting forces), or changes on the load side of the drive, such as mass or guideway friction variations. This robustness issue is confirmed in the tracking experiments conducted in Section 7.5. In order to address these problems, the following feedback strategy was developed for ED compensation.

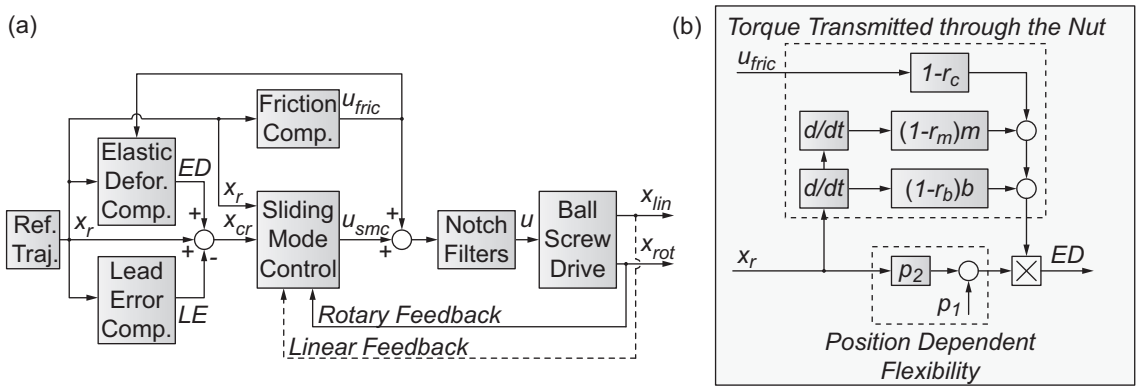

Figure 7.3: Feedforward (open loop) elastic deformation compensation.

7.4 Elastic Deformation Compensation in Feedback

The feedback approach uses the real-time control signal to estimate the elastic deformation, which gives it its robustness against external disturbances and load parameter variations. However, this creates a secondary feedback loop in the control system, which brings new stability implications. Also, the real-time control signal is noisy and needs to be smoothened out before it can be used for on-line trajectory correction. To resolve these issues, adequate filtering needs to be applied when implementing the feedback ED compensation technique.

In the following, formulation of the feedback based ED estimation is presented in Section 7.4.1. Experimental identification of the ED model parameters is explained in Section 7.4.2. Integration of the compensation scheme into the servo control system is explained in Section 7.4.3, and stability analysis is conducted in Section 7.4.4.

7.4.1 Formulation of Feedback ED Compensation

In the feedback (closed-loop) ED compensation strategy [34], the control signal equivalent torque (u_T) transmitted through the nut is calculated using the real-time control signal, u. The transmitted torque is obtained by writing the equation of motion for the first mass, representing the rotating components, in Figure 7.1(c),

$$\left.\begin{aligned} m\ddot{x} = \sum force \quad &\Rightarrow \quad r_m m\ddot{x}_{rot} = u - u_T - r_m b\dot{x}_{rot} - r_c u_{fric} \\ &\Rightarrow \quad u_T = u - (r_m m\ddot{x}_{rot} + r_b b\dot{x}_{rot} + r_c u_{fric}) \end{aligned}\right\} \tag{7.11}$$

Substituting $1/K_{eq}$ from Eq. (7.5) and u_T from Eq. (7.11) into Eq. (7.6) yields the ED model,

$$ED = u_T / K_{eq} = [u - (r_m m\ddot{x}_{rot} + r_b b\dot{x}_{rot} + r_c u_{fric})](p_1 + p_2 x_{lin}) \quad (7.12)$$

In the above model, the elastic deformation is computed using the value of the real-time feedback control signal u. A well designed servo controller will typically have integral action, or some kind of disturbance adaptation scheme, which will detect and counteract the effect of the external disturbance, represented in Figure 7.1 with d. Hence, by making use of the feedback control signal, which already accounts for unmodeled external disturbances, robustness is achieved in the ED estimate against cutting forces and dynamic variations on the load side, which will also be perceived as equivalent disturbances. This ED estimate is then used to offset the position commands so that the final linear movement of the table is realized correctly. In practical implementation, the rotary and linear position, velocity, and acceleration terms ($x_{lin}, \dot{x}_{rot}, \ddot{x}_{rot}$) are replaced by the commanded position, velocity, and acceleration values ($x_r, \dot{x}_r, \ddot{x}_r$), in order to avoid generating additional feedback loops which can cause stability problems. Using commanded position values also results in less noisy ED estimates, as opposed to using direct encoder measurements.

The model in Eq. (7.12) assumes that the rotational dynamics of the ball screw (inertia, viscous, and Coulomb friction) do not change much over the daily operation of the machine tool, which is a reasonable assumption. Accurate knowledge of these parameters is crucial for the feedback based ED compensation scheme to be successful. Assuming that the overall rigid body mass (m), viscous damping (b), and Coulomb friction (u_{fric}) values are known, the ED model has 5 parameters (r_m, r_b, r_c, p_1, p_2), which need to be identified experimentally. During the lifetime of a machine, it is evident that the viscous and Coulomb friction acting on the rotary components, as well as the axial stiffness of the ball screw mechanism, will gradually change. Hence, the ED model parameters would need to be updated during scheduled maintenance cycles of the machine tool, typically when the CNC servo parameters are also re-tuned. Tuning of the ED compensation parameters is presented in the following subsection with an example, which corresponds to the identification procedure that was applied on the ball screw setup.

7.4.2 ED Model Identification

The parameter identification is carried out using data captured from rotary and linear encoders during a trajectory tracking experiment. If the drive does not have a linear encoder, a laser interferometer can also be used. The trajectory used in this section is shown in Figure 4.5, where 350 mm of displacement is commanded at 1000 mm/sec speed, with 0.5 g acceleration and 100,000 mm/sec^3 jerk transients. The minimum and maximum displacement values are x=0 and x=350 mm. Maximum

acceleration magnitudes can be observed when the drive travels through x=5…65 and x=285…345 mm. The maximum velocity occurs in the region x=120…230 mm. Different sections of this trajectory allow the effect of different model parameters to be observed in predicting the elastic deformation.

During parameter tuning, the combined effect of the modeled lead error and the elastic deformation ($LE-ED$) is overlaid on top of the experimentally observed difference between linear and rotary encoder readings (x_{lin} - x_{rot}), as shown in Figure 7.4. This is done because the effect of lead errors and backlash, which are captured in the LE model, exhibit themselves together with the effect of elastic deformations in measurements gathered this way. When the torque transmitted to the table has a positive sign, the elastic deformation will be negative due to compression of the ball screw. Hence, the ED prediction obtained from Eq. (7.12) is subtracted rather than adding it on top of the LE value computed using Eq. (7.2).

Of the five parameters, the inertia ratio r_m in most cases can be computed analytically, which is the approach followed here. The control signal equivalent total inertia value was identified as $m=2.204\times10^{-3}$ V/(rad/sec^2). The analytically computed inertia for the rotating components is $m_{rot}=1.858\times10^{-3}$ V/(rad/sec^2). Hence r_m is calculated to be $r_m=m_{rot}/m=0.84$. If an inertia estimate for the rotating components is not available, it can be calculated with sufficient closeness by conducting two identification experiments, one with the motor detached and the second one with the motor attached to the ball screw mechanism, and making use of the catalog rated (or analytically computed) inertia values for the motor, the coupling, the gears (if there are any), and the ball screw [3].

The drive's flexibility parameters p_1 and p_2 are tuned at extreme values of the motion stroke. When the drive is at its home position (x=0), the axial flexibility and therefore the elastic deformation is dominated by p_1, since $1/K_{eq}\cong p_1$. Hence, this parameter is tuned by minimizing the discrepancy between observed and predicted values of the elastic deformation around $x\cong0$ mm, as seen in Figure 7.4(a-b). Once p_1 is determined, p_2 is tuned to match the elastic deformation at the end of the motion stroke, i.e. at $x\cong350$ mm, where its maximum effect will be observed as seen in Figure 7.4(b-c).

The tuning of the viscous friction ratio r_b is realized by matching the predicted elastic deformation with the observed values in the maximum velocity region, as depicted in Figure 7.4(d). Similarly, the

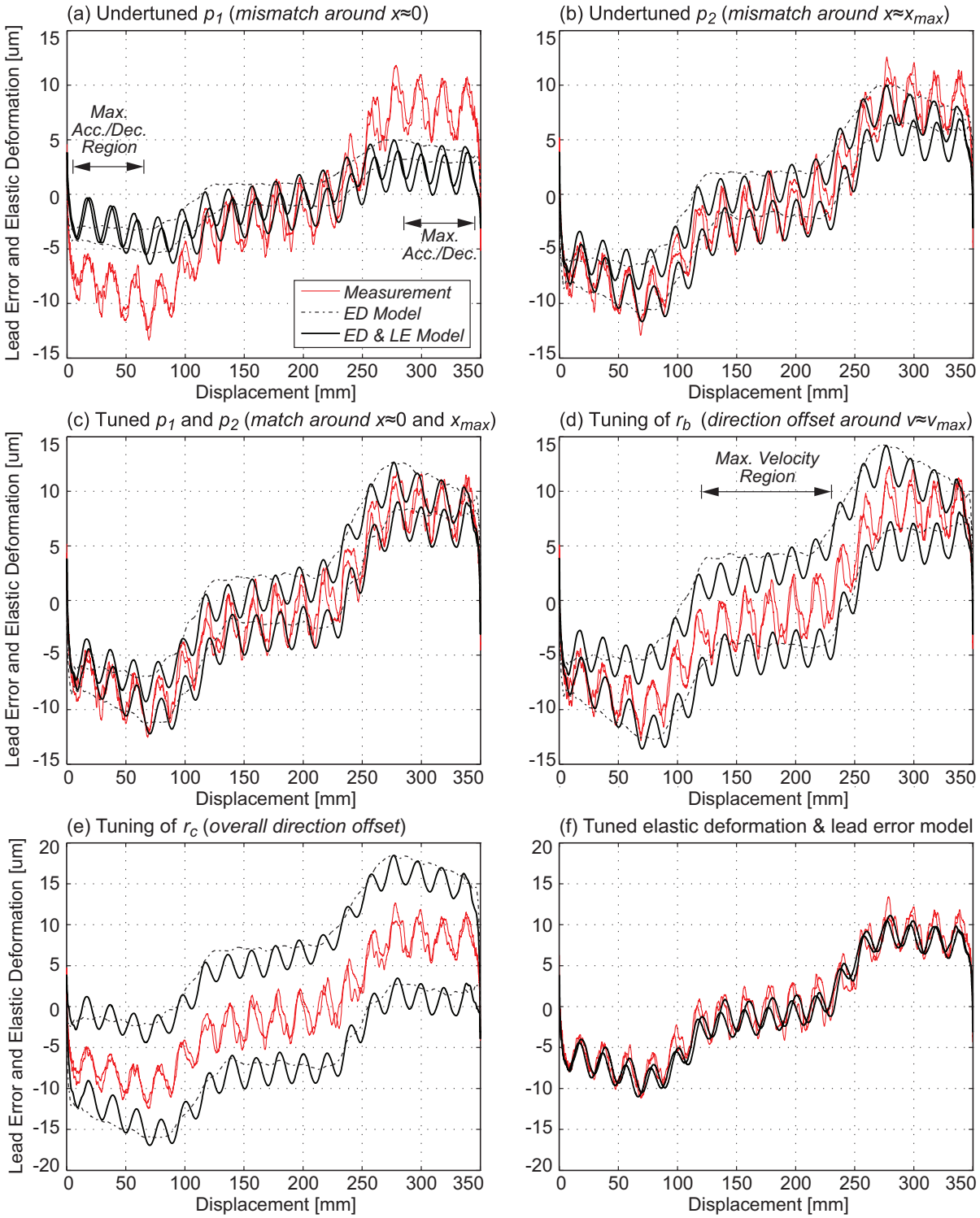

Figure 7.4: Tuning of elastic deformation model parameters.

Coulomb friction ratio r_c is tuned by matching the overall offset for the elastic deformation in the positive and negative directions throughout the motion stroke, as seen in Figure 7.4(e). The tuning of the parameters is iterated until the combined ED and LE model accurately predicts the difference between the drive's rotary and linear position readings, as seen in Figure 7.4(f). Using the above approach, the ED model parameters for the setup were identified to be $p_1 = 5.432 \times 10^{-3}$ rad/V, $p_2 = 1.626 \times 10^{-5}$ 1/V, $r_m = 0.84$, $r_b = 0.8$, $r_c = 1.0$. In order to stay consistent with the model developed earlier in this thesis, the displacement unit has been represented in terms of the ball screw's rotational motion in radians when applying the model in compensation.

7.4.3 Integration into the Control Scheme

In this section, the lead error and elastic deformation models are integrated into the control law. Although the LE and ED compensation techniques have been implemented in conjunction with rigid body based ASMC, these compensation ideas are generic and can also be applied alongside other control techniques, like PID or P-PI position-velocity cascade.

Figure 7.5(a) shows the proposed integration of closed loop elastic deformation compensation into the servo control scheme. The original command trajectory x_r is modified to account for the anticipated lead errors (LE) and elastic deformations (ED), and the corrected position command x_{cr} is utilized by the servo control law, which is the same as in the feedforward compensation scheme in Section 7.3. Again, feedforward friction compensation is applied using the model derived in Eq. (4.25), to improve the tracking accuracy at motion reversals. The ASMC and friction compensation signals are combined together ($u^* = u_{smc} + u_{fric}$) and passed through the notch filters which are designed to avoid exciting the 1st and 2nd torsional resonances, as explained in Section 4.4. The control law can use either only rotary feedback, or a combination of rotary and linear feedback, depending on which ever is available.

As before, the lead error compensation is realized in feedforward using the commanded position values (x_r) rather than actual measurements (x) in Eq. (7.2). This avoids creating additional feedback loops in the control system. Under controlled laboratory conditions, the lead errors do not exhibit a significant variation during the drive's operation. Hence the feedforward approach was found to be successful. On a production machine tool, the lead error model would have to be calibrated after the ball screw warms up to its thermal steady state condition. Another option is to use

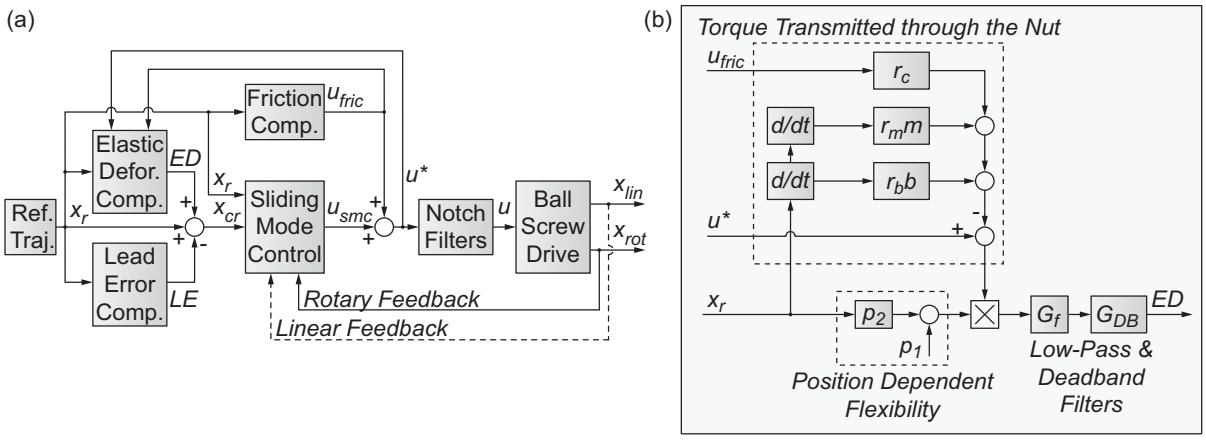

Figure 7.5: Feedback (closed-loop) elastic deformation compensation.

an adaptive lead error compensation technique, which is being investigated in another project at the Precision Controls Laboratory.

The elastic deformation compensation also makes use of the commanded position values rather than measurements. Hence, the occurrences of x_{lin}, $\dot{x}_{rot}$ and $\ddot{x}_{rot}$ in Eq. (7.12) are replaced by x_r, $\dot{x}_r$, and $\ddot{x}_r$, respectively. However, the actual value of the control signal $u*$, computed by the servo control law (ASMC) and the feedforward friction compensation blocks, is used directly in the place of u in Eq. (7.12). The reasoning behind using the actual control signal rather than an estimate computed using only feedforward terms (such as $u_{ffwd} = m\ddot{x}_r + b\dot{x}_r + u_{fric}(\dot{x}_r)$) is that a well designed servo controller with integral action will detect and compensate for any dynamic changes and external disturbances that occur within its active frequency range (i.e. bandwidth). In other words, if the inertia or friction parameters vary or there are cutting forces acting on the drive, the feedback control signal will change accordingly to accommodate the new torque demand caused by such perturbations. Under the assumption that the rotational dynamics of the drive do not change much, the additional torque demand will be accounted to the factors on the load side, which are implicitly captured in the $u*$ term. Hence, using $u*$ in the elastic deformation estimate provides robustness against variations in the table mass and guideway friction, as well as cutting force disturbances. Instead of using $u*$, it is also possible to use the control signal u, right after the notch filters. However, since the filters' attenuation frequencies are very high (445 and 1080 Hz), doing so would not change the result significantly.

A detailed view of the closed-loop elastic deformation estimation scheme is shown in Figure 7.5(b). The torque transmitted through the nut (u_T) is computed in the top section of the block diagram, per Eq. (7.11). Note that the $u*$ term enters the computation with a positive sign,

establishing a positive feedback loop that is used to estimate the instantaneous elastic deformation. This loop needs to be implemented carefully, in order to not jeopardize the stability of the overall system. The calculation of u_T uses the parameters of the rotating components ($r_m m$, $r_b b$, $r_c u_{fric}$), which are assumed to be known with sufficient closeness. The position dependent flexibility term ($p_1 + p_2 x$) is constructed at the bottom of the block diagram and multiplied with the transmitted torque estimate. Two additional blocks are also incorporated, in order to condition the elastic deformation estimate (ED) for utilization in trajectory correction. First of all, a low-pass filter G_f is introduced, which slows down the ED estimation relative to the position loop servo response. This filter is required in order to ensure that the secondary positive feedback loop, established for ED estimation, does not jeopardize the stability of the overall system. The low-pass filter also smoothens out the ED estimates, which are noisy in nature due to the actual value of the control signal $u*$ being used. By trial and error, it was seen that a 6th order filter in the form:

$$G_f = \left[\frac{2\pi f_c}{s + 2\pi f_c} \right]^6 \tag{7.13}$$

resulted in acceptable separation between the elastic deformation correction and position regulation loops. The cut-off frequency parameter f_c [Hz] is tuned iteratively using a combination of stability analysis techniques and tracking experiments. It was found that using high values for f_c resulted in the elastic deformation to be estimated and compensated faster in the control loop. This improved the drive's linear positioning accuracy, but reduced the stability margins for the overall system. In extreme cases when f_c was made too high, this led to the instability of the control loop. Using lower values for f_c, on the other hand, resulted in slower ED estimates and lower tracking accuracy. Following trial and error, it was determined that a cut-off frequency of 80 Hz led to both successful ED compensation and acceptable stability margins on the ball screw setup. The selection of the filter order and cut-off frequency, using Nyquist stability analyses, is explained in detail in Section 7.4.4.

During experimental implementation of ED compensation, it was found that a deadband filter was also necessary in order to prevent the closed loop system from going into limit cycles when stationary (zero velocity) position commands were applied. The stability analysis in Section 7.4.4, based on linearity assumptions, was not able to predict this limit cycle which occurred only during static position commands. It is believed that these limit cycles originate from the interaction between the drive's and controller's dynamics, and the nonlinear stick-slip friction acting on the ball screw rotary components. For the time being, it was found that a deadband filter, which turned the ED

compensation off during very small velocity commands, was successful in eliminating these limit cycles. The deadband filter used (G_{DB}) has the following expression:

$$G_{DB} = \begin{cases} 0 & \text{when} \quad -v_{\min} < \dot{x}_{cr} < v_{\min} \\ 1 & \text{otherwise} \end{cases} \tag{7.14}$$

By trial and error, setting the $v_{\min}$ value to 10 mm/sec was observed to yield satisfactory results. Considering the real-time implementation of closed-loop ED compensation shown in Figure 7.5(b), the elastic deformation estimate is obtained as:

$$ED = G_{DB}G_f \cdot (u_T / K_{eq}) = G_{DB}G_f[u^* - (r_m m\ddot{x}_r + r_b b\dot{x}_r + r_c u_{fric})](p_1 + p_2 x_r) \tag{7.15}$$

The lead error and elastic deformation estimates are then used to correct the trajectory command as,

$$x_{cr} = x_r + ED - LE \tag{7.16}$$

in order to realize the drive's instantaneous linear position as originally intended (i.e. $x_{lin} \cong x_r$).

As indicated in Section 7.3, the rigid body based ASMC has been used together with notch filters to fulfill the basic servo function. Cases involving only rotary feedback, as well as combined rotary and linear feedback, have been investigated. In the latter, linear position measurements were used only for disturbance adaptation, which ensured that they would be active only in the low frequency range. It was found that incorporating additional linear position feedback helped to eliminate the translational errors in steady-state, and improved the drive's positioning accuracy. In tuning the ASMC, the sliding surface bandwidth could be increased up to λ=1200 rad/sec ($\cong$ 190 Hz). By conducting analytical stability analyses and experimental tracking tests, the other parameters were tuned to be K_s=0.1 V/(rad/sec) and ρ=25 V/rad, which led to accurate position tracking and acceptable stability margins. The computer implementation sampling frequency was 8 kHz.

7.4.4 Stability Analysis

Frequency domain stability analysis was conducted to ensure that the closed-loop ED compensation does not jeopardize safe operation of the feed drive system. This analysis is also useful for tuning the ASMC and the low-pass filter in ED compensation. The analysis is conducted using Nyquist's stability theory, which requires the derivation of the loop transfer function. The analysis here assumes that only rotary position measurements are used in the feedback control law. A similar procedure, like the one presented in Section 6.5, can also be used to analyze the stability with combined linear and rotary feedback.

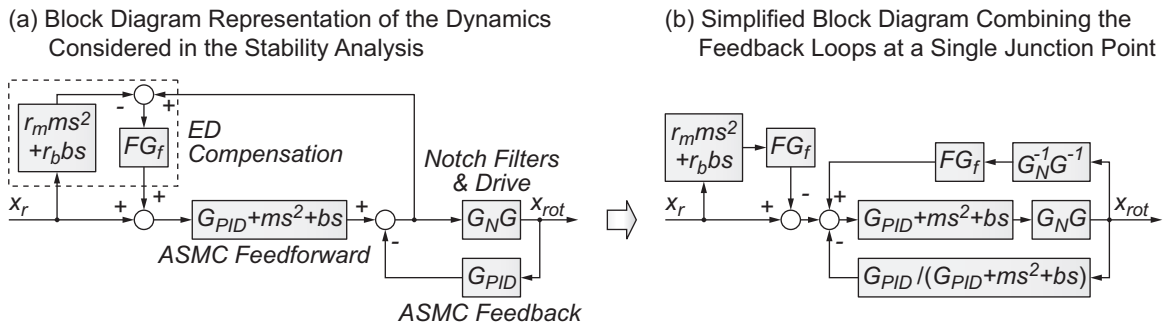

Figure 7.6: Derivation of the loop transfer function for Nyquist stability analysis.

A block-by-block representation of the dynamics that affect the stability of the control system is shown in Figure 7.6(a). In the figure, G represents the drive's rotary position transfer function (i.e. $G = x_{rot}(s)/u(s)$). $G_N(s)$ represents the notch filters. As indicated in Section 4.3, the rigid body based ASMC can be rewritten as a PID controller with feedforward velocity and acceleration command terms, in the form:

$$u_{smc} = \underbrace{K_{acc}\ddot{\theta}_{ref} + K_{vel}\dot{\theta}_{ref}}_{\substack{\text{Acceleration and Velocity} \\ \text{Feedforward}}} + \underbrace{K_p(\theta_{ref} - \theta) + K_i\int_0^t(\theta_{ref} - \theta)d\tau + K_d(\dot{\theta}_{ref} - \dot{\theta})}_{\text{Proportional + Integral + Derivative (PID) Control}} \qquad (7.17)$$

$$\text{where : } K_{acc} = \hat{m},\ \ K_{vel} = \hat{b},\ \ K_p = K_s\lambda + \rho,\ \ K_i = \rho\lambda,\ \ K_d = K_s + \hat{m}\lambda - \hat{b}$$

The feedforward terms can be represented in the Laplace domain as $(ms^2 + bs)\cdot x_{cr}(s)$. The PID terms correspond to $G_{PID}(s)\cdot(x_{cr}(s) - x_{rot}(s)) = (K_p + K_i/s + K_d s)\cdot(x_{cr}(s) - x_{rot}(s))$. In Figure 7.6(a), the PID and feedforward terms have been represented with the "ASMC Feedforward" and "ASMC Feedback" blocks.

It was shown in Eq. (7.5) that the drive's equivalent axial flexibility varies as a function of the drive's position (i.e. $1/K_{eq} = p_1 + p_2 x$), which brings an inherent nonlinearity to the closed-loop system. In order to simplify the analysis, this flexibility is approximated with single nominal value ($F = p_1 + p_2 x^*$), computed at one particular position of the drive (x^*). To evaluate the effect of position dependency, the flexibility values will later be calculated for different axis locations and considered in the stability analysis, thus yielding an envelope of Nyquist plots which correspond to different axis positions. In Figure 7.6(a), G_f corresponds to the low-pass filter used in the closed-loop elastic deformation compensation, which was given in Eq. (7.13).

The effects of lead error cancellation and friction compensation enter the control loop in a purely feedforward manner, and do not affect the feedback stability. Hence, they are not considered in the

analysis. Due to its nonlinear nature, the deadband filter has been left out of the analysis as well. This is not an overly constraining simplification, because this filter is only used to turn the ED compensation off when the position commands are stationary. When this happens, the drive does not experience significant elastic deformation, anyway. The remaining terms used to construct the ED estimate in Eq. (7.15) are represented with the blocks that contain the expressions ($r_m ms^2 + r_b bs$) and (FG_f) in Figure 7.6(a).

By applying block diagram algebra, the schematic in Figure 7.6(a) can be simplified into the form in Figure 7.6(b), where the two feedback channels close the loop at the same junction point. The trailing feedforward component $1-(r_m ms^2 + r_b bs)FG_f$ does not affect the stability, as long as the low-pass filter G_f has stable poles ($f_c > 0$). The dynamics of the two feedback loops can be combined into a single transfer function which closes the loop with a negative sign:

$$H(s) = \frac{G_{PID}}{G_{PID} + ms^2 + bs} - FG_f G_N^{-1} G^{-1} \tag{7.18}$$

The dynamics in the forward path of the loop are,

$$D(s) = GG_N (G_{PID} + ms^2 + bs) \tag{7.19}$$

The loop transfer function $L(s)$ is obtained by multiplying $D(s)$ with $H(s)$:

$$\left.\begin{aligned} L(s) = D(s)H(s) &= GG_N (G_{PID} + ms^2 + bs)[\frac{G_{PID}}{G_{PID} + ms^2 + bs} - FG_f G_N^{-1} G^{-1}] \\ \Rightarrow L(s) &= GG_N G_{PID} - FG_f (G_{PID} + ms^2 + bs) \end{aligned}\right\} \tag{7.20}$$

The stability analysis is conducted by evaluating the Nyquist plots for the loop transfer function, calculated at different values of the drive position. In computing the frequency response of $L(s)$, the frequency response of the drive transfer function (G) is directly substituted from the experimentally measured data. The frequency response of the remaining terms, which are part of the digital control law (i.e. G_N, G_{PID}, $ms^2 + bs$, and G_f), are computed analytically. The contribution of each term is then combined using complex arithmetic. The Nyquist plots generated this way are shown in Figure 7.7.

Figure 7.7(a) investigates the effect of the low-pass filter order, and Figure 7.7(b) the cut-off frequency, on the overall system stability. The shaded zones represent the Nyquist curve envelopes

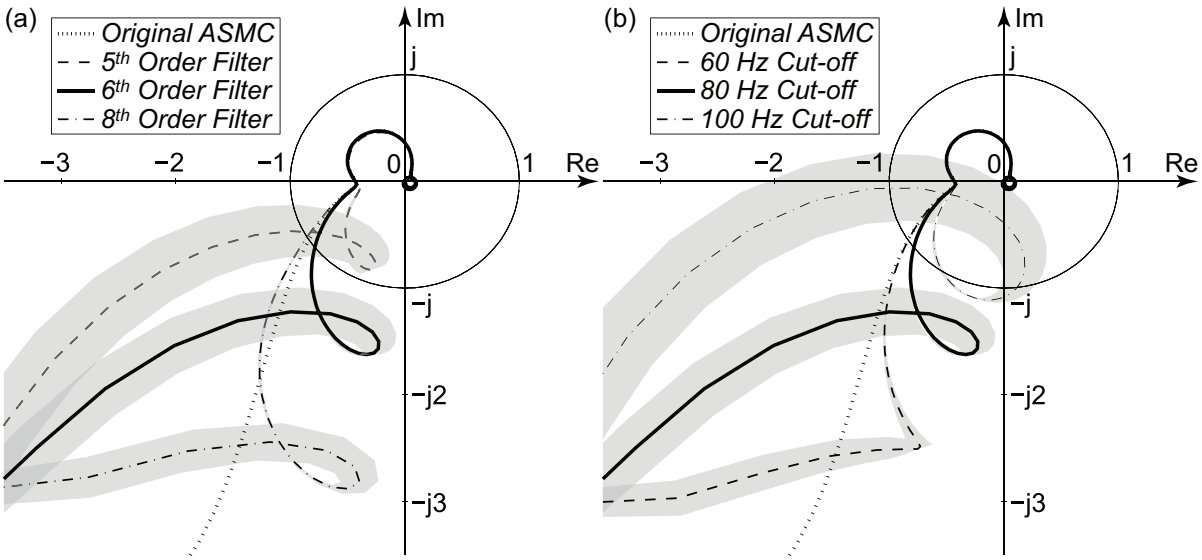

Figure 7.7: Variation of loop stability with the choice of ED compensation filter: (a) Effect of filter order, (b) Effect of corner frequency. Shaded regions indicate the influence of position dependent drive flexibility.

obtained by varying the drive's position, and therefore the axial flexibility, between the extreme values of 0 and 350 mm. The upper boundaries of the shaded regions correspond to the case where the drive is at its furthest position, which yields the highest value for the axial flexibility parameter F. Since this term acts as a positive feedback gain, these cases result in the lowest stability margins. The lower boundaries corresponds to the case where x=0 mm, and the middle (nominal) curves are obtained by considering the nut location to be at the center of its travel range, which is 175 mm.

Considering Figure 7.7(a), when no ED compensation is used (i.e. the "Original ASMC" case), the adaptive sliding mode controlled system has a gain margin of GM = 2.3 and a phase margin of PM = 31°. When a 5^{th} order low-pass filter with 80 Hz corner frequency is used to smoothen the ED compensation values, the phase margin for the nominal case (i.e. mid drive position) drops to PM = 27°. However, the situation gets worse when the drive is at its extreme end position (350 mm) in which PM becomes only 12°, which is not acceptable for safe machine tool operation. When the low-pass filter order is increased to six (as represented in Eq. (7.13)), the region in the Nyquist plot that exhibits a significant position dependent behavior occurs outside the unit circle. Neither the gain, nor the phase margins suffer from the ED compensation loop. In fact the PM increases slightly, to 36°. In tracking experiments, it was observed that the 6^{th} order filter allowed the ED compensation loop to react quickly enough to correct for the drive's final linear position. When the filter order is increased to 8, the stability margins are still retained. However, the tracking results obtained with the 8^{th} order filter were visibly worse, due to the slower reaction time in the ED compensation. Hence, 6^{th} order

filtering was found to be the most adequate for smoothening the ED estimates for real-time compensation.

The effect of filter corner frequency is shown in Figure 7.7(b). In this case, the filter order has been set to 6 and the value of f_c is varied between 60 to 100 Hz. When the corner frequency is at 100 Hz, the closed-loop system is barely stable for the nominal drive position (PM=4°), and unstable when the drive is at its extreme end. This indicates that the ED compensation loop is too fast and that it interferes with the basic servo function of the ASMC. The loop stability is recovered when the cut-off frequency is decreased to 80 Hz. Using a lower cut-off (60 Hz) does not affect the stability margins, as the variations in the Nyquist plot occur outside the unit circle. However, the ED compensation becomes more sluggish, resulting in less improvement in the final positioning accuracy of the drive. Hence, for the balls screw setup and the given ASMC design, a 6th order low-pass filter with 80 Hz cut-off frequency was found to be the most suitable.

The above stability analysis has focused mainly on the selection of the low-pass filter, which acts as a frequency dependent weight to ensure that the ED compensation loop, with positive feedback, does not jeopardize the stability of the overall servo system. The same framework can also be used in tuning the ASMC parameters (λ, K_s, ρ), or ensuring that the notch filters in the loop have been designed correctly.

7.5 High Speed Tracking Results

In order to evaluate the performance of the developed compensation techniques, tracking tests were performed on the ball screw setup. A jerk continuous trajectory, similar to the one shown in Figure 4.5, was used with 350 mm of displacement, 1000 mm/sec feed rate, 0.5 g acceleration, and 100,000 mm/sec^3 jerk transients. Six different cases were investigated. The first set of experiments (Cases 1-3) focused on using only rotary feedback for controls, in which the benefit of applying ED compensation is the most significant. The second set of tests (Cases 4-6) considered the availability of both rotary and linear feedback. These tests investigate whether the proposed ED compensation technique can provide a further improvement in the ball screw drive's linear positioning accuracy, beyond the performance that is already achieved by just incorporating direct linear position feedback. To evaluate the robustness of each implementation against load changes, the experiments were conducted for both nominal table mass, and 130% increased table mass conditions. The controller parameters were left unchanged. The mass increase was realized by attaching a 43.5 kg weight to the table.

7.5.1 Using only Rotary Feedback

In Cases 1-3, the control loop was closed using rotary feedback and the linear encoder was used only to monitor the table's true position. The tracking results are shown in Figure 7.8 to Figure 7.13. The maximum and RMS values of tracking error are summarized in the first three rows of Table 7.2. The RMS error values were computed by considering the movement (i.e. nonzero velocity) portions in the command trajectory. The tracking error was evaluated using the original position commands and linear encoder measurements ($e = x_r - x_{lin}$).

In Case 1, no ED or LE compensation is used. Although the servo controller is successful in tightly controlling the rotary motion of the ball screw, the tracking error estimate (which is based on linear encoder measurements) indicates the presence of significant elastic deformations and lead errors. Considering Figure 7.8, the dominance of elastic deformation is confirmed by the fact that the shape of the tracking error profile closely resembles that of the control signal (i.e. actuation torque). The maximum and RMS values of linear positioning error are 15.9 and 9.017 um, respectively. When the additional weight is added to the table, as see in Figure 7.9, the ED becomes more severe resulting in a maximum error of 28.6 um. The RMS value also increases to 15.952 um.

In Case 2, the open loop compensation strategy outlined in Section 7.3 is applied. This is done in order to facilitate a comparison with the closed loop scheme tested later in Case 3. As seen in Figure 7.10, the application of feedforward ED and LE compensation reduces the tracking error noticeably, from a maximum value of 15.9 down to 5.4 um. However, when the table mass changes, the prediction accuracy of the ED model degrades, as can seen at the bottom of Figure 7.11. Due to the faulty compensation, and also the use of the incorrect total inertia value in the ASMC law, the

Table 7.2: Summary of maximum and RMS (root mean square) tracking error values.

Case	Nominal Table Mass		130% Increased Table Mass	
	Max. Error [um]	RMS Error [um]	Max. Error [um]	RMS Error [um]
Only Rotary Feedback				
No compensation	15.9	9.017	28.6	15.952
Open loop compensation	5.4	1.660	15.4	8.718
Closed-loop compensation (proposed)	4.1	1.494	10.6	2.825
Combined Rotary and Linear Feedback				
No compensation	6.5	2.332	11.7	3.476
Only lead error compensation	6.2	1.580	9.8	2.950
Closed-loop compensation (proposed)	3.8	1.360	8.3	2.572

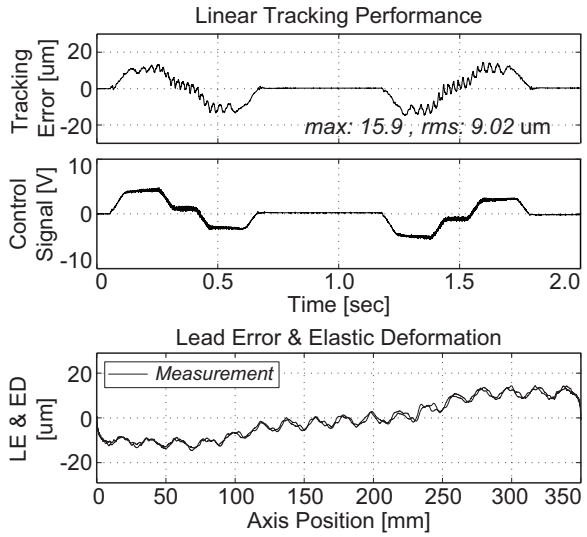

Figure 7.8: No ED or LE compensation, only rotary feedback, nominal table mass.

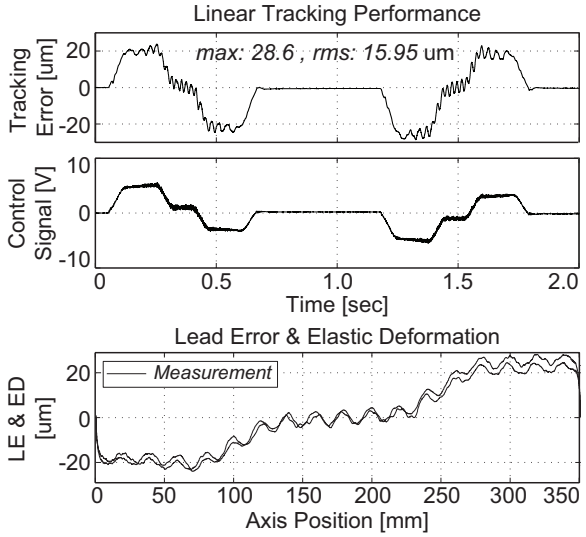

Figure 7.9: No ED or LE compensation, only rotary feedback, 130% increased table mass.

maximum and RMS values of linear tracking error increase to 15.4 and 8.718 um, respectively.

The sensitivity of the open loop compensation scheme to changes in the load mass is explained by the fact that the ED estimate is calculated assuming accurate knowledge of the dynamic parameters (i.e. mass, friction, etc.) on the load side, as can be seen in Eq. (7.8). As this experiment demonstrates, the performance improvement gained with the open loop approach will deteriorate when the table mass changes due to part loading or unloading. Similarly, also when there are cutting forces acting on the table.

In Case 3, the closed-loop compensation technique is implemented. Under nominal mass conditions (Figure 7.12), this technique performs slightly better than the open loop approach yielding maximum and RMS tracking error values of 4.1 um and 1.494 um, respectively. When the table mass is increased (Figure 7.13), the closed-loop compensation technique is able to detect this effect by monitoring the feedback control signal, and produces a more accurate estimate of the combined elastic deformation and lead error profile, as can be seen at the bottom of Figure 7.13. Hence, this compensation scheme is more effective and robust, compared to the open loop approach, and the linear tracking errors are smaller. The maximum value of the tracking error is 10.6 um (31% less) and the RMS value is 2.825 um (68% smaller).

The results obtained for the increased table mass are in general worse than those obtained for nominal mass conditions. This overall degradation is due to the mismatch between the actual and modeled values of total inertia, which results in faulty feedforward compensation of inertial forces in

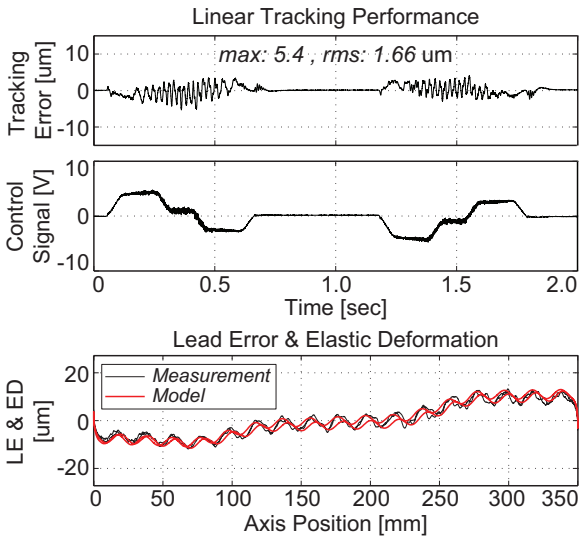

Figure 7.10: Feedforward (open loop) ED and LE compensation, only rotary feedback, nominal table mass.

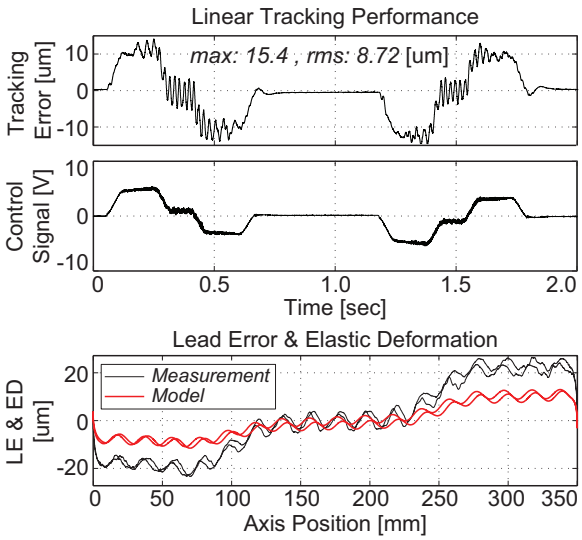

Figure 7.11: Feedforward (open loop) ED and LE compensation, only rotary feedback, 130% increased table mass.

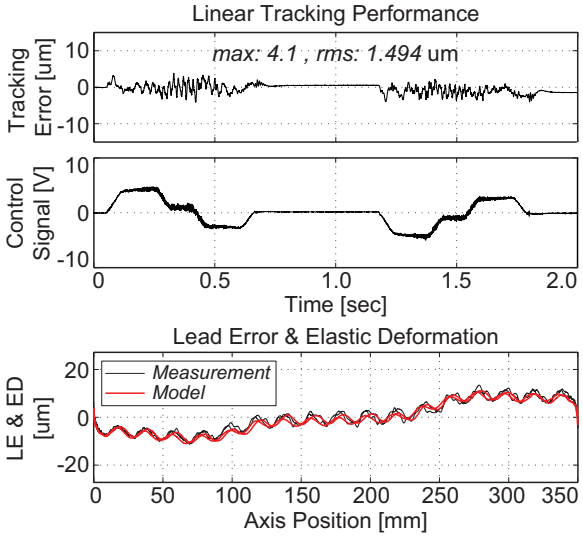

Figure 7.12: LE and feedback (closed-loop) ED compensation, only rotary feedback, nominal table mass.

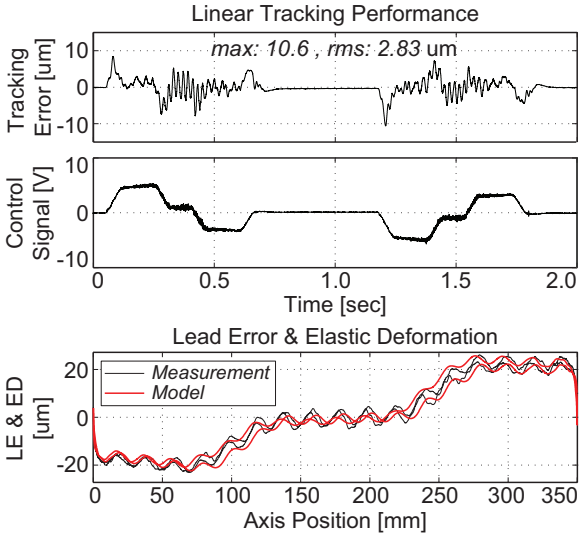

Figure 7.13: LE and feedback (closed-loop) ED compensation, only rotary feedback, 130% increased table mass.

the adaptive sliding mode control law (i.e. the $K_{acc}\ddot{\theta}_r = \hat{m}\ddot{\theta}_r$ term in Eq. (7.17)). In spite of the significant variation on the load side, the closed-loop technique is still fairly successful in estimating and correcting for the actual elastic deformation, as seen in Figure 7.13.

Among the results obtained in Cases 1-3, it can be inferred that the closed-loop compensation strategy yields the best linear positioning accuracy when only rotary feedback is available, and is the most robust against changes in the drive parameters.

7.5.2 Using Combined Rotary and Linear Feedback

In Cases 4-6, the control loop was closed using both rotary and linear feedback. As explained in Section 7.3, rotary position measurements were used as the principal feedback, in order to achieve tight control over a wide frequency range. Linear encoder measurements were used only in the disturbance adaptation law. This helped to improve the steady-state positioning accuracy of the table. This configuration is somewhat similar to the P-PI position-velocity cascade control structure used in most machine tools, where the velocity loop is closed using rotary feedback for high stiffness, and the position loop is closed using a linear encoder which helps to mitigate the effects of backlash, lead errors, and elastic deformations in steady-state. The objective in the proceeding experiments is to evaluate whether the developed closed-loop compensation strategy yields a further improvement in the positioning accuracy of a ball screw drive, which already has rotational and linear position feedback. The experiments were conducted in a similar manner to those in Section 7.5.1. The tracking performance was evaluated using the original command positions and linear encoder measurements ($e = x_r - x_{lin}$). The results are presented in Figure 7.14 through Figure 7.19. The maximum and RMS values of tracking error have been summarized in the last three rows of Table 7.2.

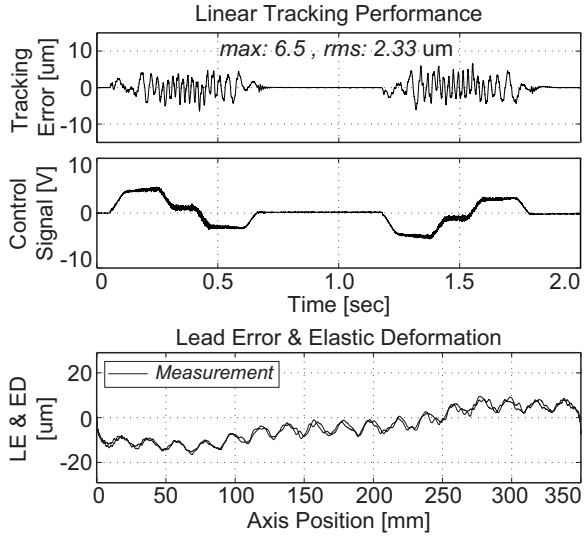

Figure 7.14: No ED or LE compensation, combined rotary and linear feedback, nominal table mass.

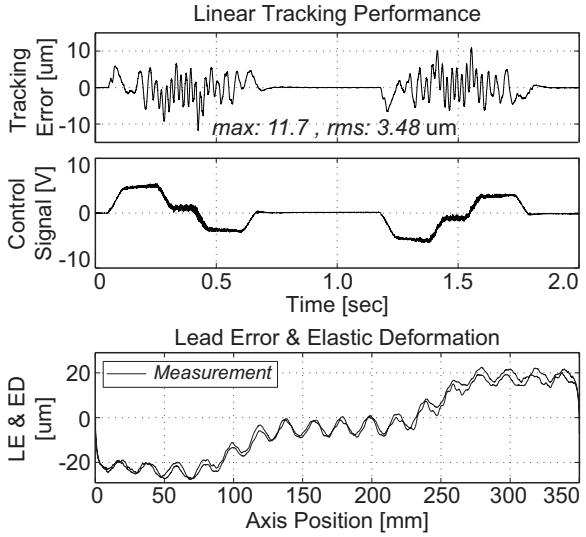

Figure 7.15: No ED or LE compensation, combined rotary and linear feedback, 130% increased table mass.

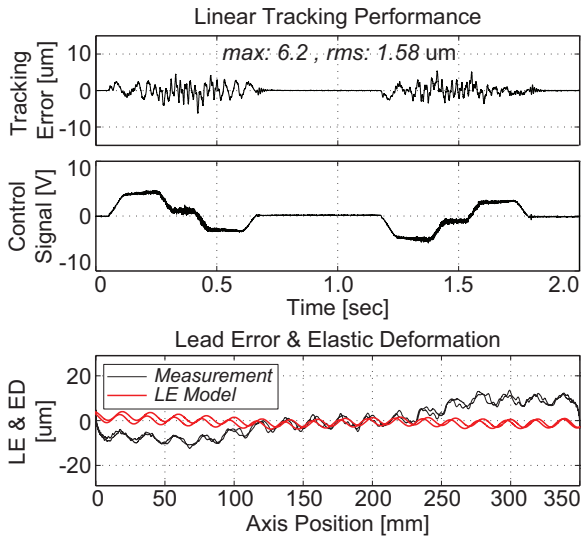

Figure 7.16: Only LE compensation, combined rotary and linear feedback, nominal table mass, max. er.: 6.2 um, rms: 1.58 um.

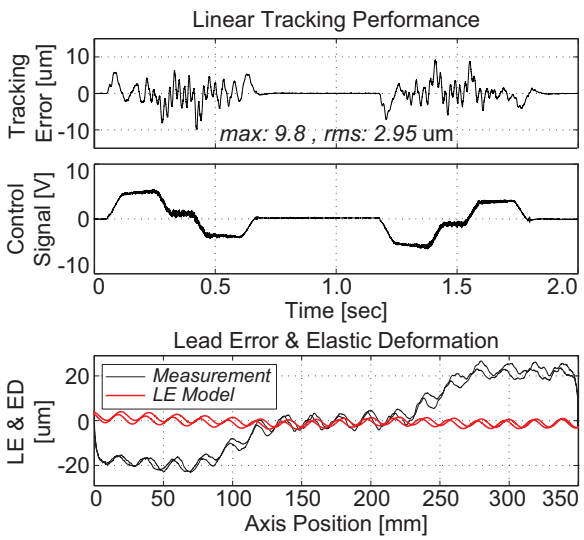

Figure 7.17: Only LE compensation, combined rotary and linear feedback, 130% increased table mass, max. er.: 9.8 um, rms: 2.95 um.

In Case 4, neither lead error nor elastic deformation compensation is applied. In this case, the effect of elastic deformation is gradually corrected in the feedback loop, using direct linear position measurements. This correction is not instantaneous, but quick enough to avoid a visible offset in the average value of the tracking error. The lead errors, on the other hand, enter the feedback loop along with linear position measurements and are amplified inside the control loop. Although the actual lead error amplitude is only around 1.987 um, as reported in Section 7.2.1, the amplitude of fluctuations in the tracking error profile caused by the lead errors is around 4-5 um, as a result of the mentioned amplification in the feedback loop. For the nominal table mass (Figure 7.14), the maximum and RMS values of linear positioning error are 6.5 and 2.332 um, respectively. When the table mass is increased by 130% (Figure 7.15), the maximum and RMS values of linear tracking error increase to 11.7 and 3.476 um, respectively. This confirms the observation that the main reason behind the performance degradation is the mismatch between the nominal value of inertia used in the ASMC design, and its actual value. This problem can be corrected, if necessary, by allowing for on-line adaptation of the mass parameter in the sliding mode control law derived in Section 4.3. Alternatively, short identification experiments can also be incorporated into the operation of the drive between long G-code cycles, in order to update the model parameters [17].

It is interesting to note that the positioning accuracy obtained in this case, using combined linear and rotary feedback but no LE or ED compensation, is slightly worse than the accuracy obtained using only rotary feedback together with LE and closed-loop ED compensation (Case 3). This holds

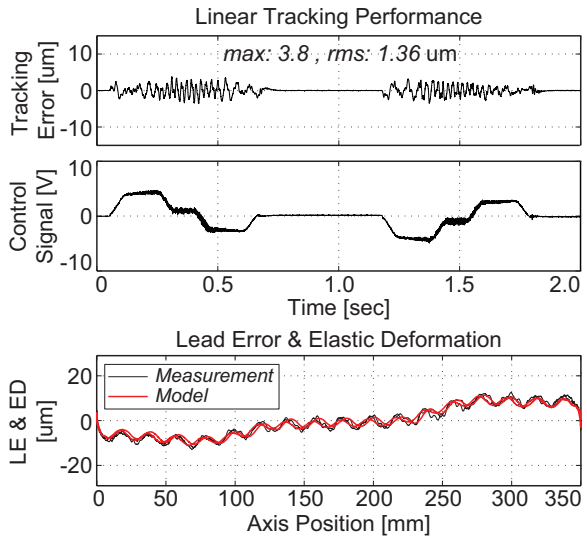

Figure 7.18: LE and feedback (closed-loop) ED compensation, combined rotary and linear feedback, nominal table mass.

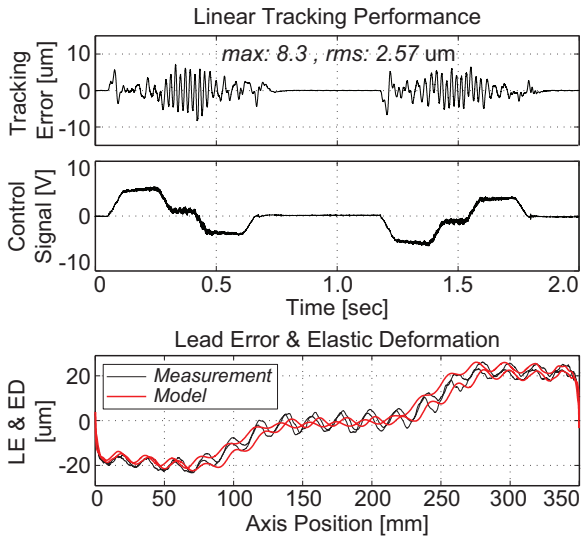

Figure 7.19: LE and feedback (closed-loop) ED compensation, combined rotary and linear feedback, 130% increased table mass.

for both nominal and increased table mass cases. However, this observation applies only from the standpoint of elastic deformations and lead errors. In the presence of thermal expansion of the ball screw, which is usually inevitable, using direct linear feedback will typically yield more accurate positioning results.

In Case 5, only lead error compensation is used. As mentioned earlier, when a linear encoder is used for direct position measurement, the lead error enters the feedback loop in the form of a sinusoidal output disturbance. If the ball screw's rotational frequency is in the vicinity of one of the peaks in the complementary sensitivity (i.e. measurement noise) transfer function, then the effect of lead errors will become amplified. Even if the control system is designed to avoid such closed-loop resonances, the feedback control law cannot immediately compensate for rapid fluctuations in the axis position caused by lead errors. Subtraction of the anticipated lead error from command trajectory is an effective way of mitigating this problem. In order to assess the performance improvement realized by closed-loop ED compensation, separately from the contribution of LE cancellation, in this intermediate step only LE compensation is applied in conjunction with the dual feedback configuration.

The tracking results are shown in Figure 7.16 and Figure 7.17. In the nominal mass case, the largest value of the tracking error drops from 6.5 to 6.2 um, indicating the dominance of elastic deformation transients, which are not instantaneously corrected in the control law. The contribution of lead error compensation can be observed from the drop in the RMS value of tracking error, from 2.332 to 1.580

um. As seen in the tracking error profile, the fluctuations due to lead errors are somewhat smaller, compared to those in Figure 7.14 (i.e. Case 4). Looking at the bottom of the figure, it is seen that the lead error model predicts only the sinusoidal component of the discrepancy between the rotary and linear encoder measurements. With the table mass increased, the maximum and RMS values of tracking error also increase to 9.8 and 2.950 um, which are better than those reported in Case 4 with no LE compensation.

In the last case (Case 6), both LE and closed-loop ED compensation have been applied together with rotary and linear feedback in the servo loop. The experimental tracking results are shown in Figure 7.18 and Figure 7.19. Under nominal inertia conditions, this implementation yields the highest dynamic accuracy among all other cases. The tracking error does not exceed 3.8 um, which is a 39% improvement over the results obtained with only LE compensation. The reduction in the RMS value of tracking error is more modest (14%), since this value is influenced primarily by the lead errors which were already compensated in Case 5. The overall performance improvement is accounted to the closed-loop ED compensation mechanism, which was designed to explicitly estimate and cancel out the drive's elastic deformation, on top of the ASMC's regular servo function. Considering the tracking results obtained for increased table mass, it is seen that the closed-loop ED compensation still yields the best results in terms of maximum and RMS tracking error, which were recorded to be 8.3 and 2.572 um respectively. These results are also the best ones among all of the cases that were tested.

As confirmed in the experimental results, the developed closed-loop ED compensation strategy improves the final positioning accuracy of ball screw drives beyond the performance that is already achieved by just incorporating additional linear position feedback. As seen in Figure 7.13 and Figure 7.19, the elastic deformation and lead error model accurately predicts the discrepancy between the drive's rotary and linear motions, even in the presence of table inertia changes, which validates the robustness of the technique. It can also be inferred that the closed-loop ED compensation strategy will be robust against machining forces and changes in the linear guideway friction, which would be perceived as equivalent external disturbances similar to the effect of inertia variation. These effect would be implicitly taken into account in the elastic deformation model. In fact, viscous friction and average cutting forces, which are functions of velocity and feed, typically exhibit a slower variation compared to inertial forces which depend on acceleration, and are therefore easier to detect and account for in the control law and the ED compensation scheme. Currently, the ball screw drive is undergoing a retrofit so that the robustness of the ED compensation scheme can be verified in machining experiments.

7.6 Limitations

The presented closed-loop ED compensation technique is an efficient and effective approach for improving the linear positioning accuracy of ball screw drives, in particular for less expensive feed drives with only rotational feedback. Iterative tuning of the ED model is not trivial and requires some expert knowledge. Although the scheme is robust against deformations caused by disturbances and dynamic parameter changes, the compensation is realized with a small delay due to the response time of integral action in the feedback control signal, which compensates for the equivalent additional disturbance. Another limitation is the requirement for accurate partial information about the drive system, namely the rotational inertia, viscous damping, and Coulomb friction values.

7.7 Conclusions

This chapter has presented two techniques to compensate for the elastic deformations in ball screw drives. The feedforward approach is simple to implement but suffers in robustness when there are parameter variations (or force disturbances) on the load side of the drive. The feedback approach, on the other hand, is more robust, even when there are significant variations in the table inertia.

The overall methodology is based on a simple and intuitive physical model, which captures the drive's elastic deformation characteristics with reasonable accuracy. The parameters of the model were identified by matching the predicted discrepancy between the rotary and linear motions of the drive mechanism. Due to the utilization of the actual control signal in the closed-loop compensation scheme, the effect of external disturbances and load changes are implicitly accounted for and compensated. In order to improve the tracking accuracy further, the effect of lead errors has also been modeled and incorporated into the compensation scheme. Stability implications of conducting ED compensation in closed-loop, which adds a secondary positive feedback loop, were analyzed and tuning guidelines established, in order to maintain safe operation of the feed drive system. Experimental tracking results indicate that the closed-loop strategy always achieves an improvement in the drive's linear positioning accuracy, both for only rotary feedback, as well as combined rotary and linear feedback configurations.

In the experiments conducted so far, only the effect of load inertia variation was investigated. The ball screw is currently being retrofitted with guideway covers, in order to validate the developed compensation algorithms in machining tests.

Chapter 8
Conclusions

8.1 Conclusions

This thesis has studied new control techniques to achieve higher dynamic accuracy and stiffness in high-speed ball screw drives. After detailed identification of the drive's dynamics, high bandwidth and accurate tracking controllers were developed using Adaptive Sliding Mode Control (ASMC) theory. New compensation techniques were also developed for the torque ripples and elastic deformations. As the first major contribution in this thesis, the 1st axial mode of vibration was actively dampened out by including the dynamics of this mode into the controller design. As the second major contribution, a robust strategy was developed which compensates for the elastic deformations and lead errors, thus resulting in accurate positioning of the table using only rotary encoder feedback.

A precision ball screw was designed and built for this study. Detailed dynamic modeling and identification tasks were performed, considering the rigid body dynamics, nonlinear friction, torque ripples, axial and torsional vibrations, lead errors, and elastic deformations. Various techniques were used in the model building stage, such as Least Squares parameter identification, Finite Element modeling, Kalman filtering, and experimental frequency response measurements. Consequently, motion control laws capable of achieving high control bandwidth, good tracking accuracy, and decent disturbance rejection characteristics, were developed based on the identified dynamics. The contributions are summarized as follows:

As the first attempt in achieving high control bandwidth, an Adaptive Sliding Mode Controller (ASMC) was designed based on the rigid body dynamics of the drive. Feedforward friction compensation was added to improve the accuracy at velocity reversals. Notch filters were used to handle the structural resonances. A bandwidth of 223 Hz was realized in controlling the rotational motion of the ball screw, resulting in servo accuracy equivalent to 1.6 um, while the table was traveling at 1000mm/sec with 1 g acceleration transients. Also, a simple vibration cancellation technique for damping out the 1st torsional mode was developed and successfully implemented. This technique results in smoother and more efficient motion, by reducing the magnitude of vibrations excited at the 1st torsional mode.

The motor and mechanical torque ripples were modeled using Kalman filtering and were compensated in conjunction with the ASMC scheme. This was realized at the motion control level, instead of the current loop, allowing the methodology to be applied on different types of drives in a generic manner. The compensation improved the smoothness and accuracy of the drive's motion, especially at low speeds and low control bandwidths. Improvement was still observed at high speeds and high control bandwidths, but was less evident due to the control signal assuming larger magnitudes and becoming more sensitive to measurement noise. Still using the rotary encoder as the principal feedback, the tracking accuracy was further improved to 0.95 um.

As one of the main contributions in this thesis, a new control algorithm was developed based on Adaptive Sliding Mode Control, which actively dampens out the vibrations of the 1st axial mode and achieves superior command following accuracy in the drive's translational motion. It was shown that this "mode compensating" ASMC (MC-ASMC) is capable of achieving a significantly higher positioning bandwidth and dynamic stiffness, compared to the traditional practice of notch filtering the axial vibration inside the control loop. The MC-ASMC can be practically implemented in real-time using rotary and linear position measurements, which are available on most drive systems. Since the state variables are only rotary and linear position and velocity, there is no need to construct an elaborate state observer. This decreases the computational load and makes the control law favorable for real-time implementation. In this scheme, lead errors which originate from imperfections of the ball screw, were also modeled and compensated in feedforward.

After tuning the MC-ASMC, an experimental command following bandwidth of 208 Hz was achieved, which is several-fold higher than typical positioning bandwidths (30-50 Hz) realized on ball screw drives. Through impact hammer tests, it was shown that the MC-ASMC helps to improve the dynamic stiffness around the axial mode, which also contributes to making the drive system more immune against chatter vibrations. Stability analysis was performed, demonstrating decent phase and gain margins (2.14, 30°), and a linear tracking accuracy of 2.6 um was obtained at 1000 mm/sec feed and 0.5 g accelerations. The stability analysis, which was verified with further tracking experiments, can be used in parameter selection for the MC-ASMC.

Another major contribution in this thesis was the development of a novel feedback control strategy for compensating for the elastic deformations (ED) in ball screw drives. Due to the utilization of the real-time control signal in ED estimation, the compensation technique is robust against the effect of external disturbances and load side parameter variations. The proposed strategy establishes a secondary positive feedback loop, similar to the positive "joint torque feedback" technique known in the literature. Stability issues are addressed by incorporating a high-order low-pass and a deadband

filter in the ED compensation loop. Nyquist stability analysis was performed to predict the stability of the overall system. This control technique also demonstrates decent gain and phase margins while achieving a high linear positioning accuracy of 4.1 um at 1000 mm/sec feed and 0.5 g acceleration. This performance was obtained with only rotary encoder feedback in the control law, making the developed ED compensation algorithm highly favorable for low-cost CNC machines that are not equipped with linear scales. This compensation technique also resulted in an improvement in the dynamic accuracy when it was implemented in conjunction with both rotary and linear feedback devices.

8.2 Future Research Conclusions

The developed control algorithms can be implemented independently on different drives of a multi-axis machine. By improving the individual tracking accuracy in each axis, it can be expected that the overall contouring accuracy will also improve. Further experiments to verify this on a multi-axis CNC machine tool are considered as future work.

In addition, the control algorithms still need to be validated in machining experiments. Preparations for such experiments are currently underway, which require the retrofit to the ball screw drive with guideway covers so that it can be used in cutting operations.

A stability analysis was developed for the MC-ASMC. However, the parameter selection for this controller is still not a trivial task. New tuning guidelines need to be investigated, in order to make the MC-ASMC more practical for safe implementation on industrial machines.

In the MC-ASMC and closed-loop ED compensation strategies, a simplified lumped model was used to describe the axial vibrations and drive flexibility. This model can be improved further by complementing it with Finite Element analyses and additional frequency response measurements. This would allow the representation of additional modes, as they reflect on the axial dynamics of the drive, to be considered and compensated in the control law. Although compensation at high frequencies beyond 500 Hz appears impractical on the current setup, as better motors and amplifiers that deliver higher actuation bandwidths become available, achieving higher positioning bandwidth will become even more relevant, particularly in mechanical actuation systems such as ball screw drives.

Bibliography

[1] Allotta B., Angioli F., Rinchi, M., 2001, "Constraints Identification for Vibration Control of Time-Varying Boundary Conditions Systems", Proceedings of the 2001 IEEE/ASME International Conference on Advanced Intelligent Mechatronics (AIM), Vol. 1, pp. 606-611.

[2] Altintas Y., Erkorkmaz K., Zhu W.H., 2000, "Sliding Mode Controller Design for High Speed Drives", Annals of CIRP, Vol. 49, No. 1, pp. 265-270.

[3] Altintas Y., 2000, Manufacturing Automation: Metal Cutting Mechanics, Machine Tool Vibrations, and CNC Design, Cambridge University Press.

[4] ANSYS Elements User's Guide, 2004, ANSYS, Inc.

[5] Armstrong H.B., Dupont P., Canudas D.W.C., 1994, "A survey of Models, Analysis Tools and Compensation Methods for the Control of Machines with Friction", Automatica, Vol. 30, No. 7, pp. 1083-1138.

[6] Astrom K.J., Wittenmark B., 1997, Computer-Controlled System: Theory and Design, Third Edition, Prentice-Hall Inc., NJ.

[7] Bolton H.R., Ashen R.A., 1984, "Influence of Motor Design and Feed-Current Waveform on Torque Ripple in Brushless DC Drives", IEE Proceedings B on Electric Power Applications, Vol. 131, No. 3, pp. 82-90.

[8] Chen Y., Tlusty J., 1995, "Effect of Low-Friction Guideways and Lead-Screw Flexibility on Dynamics of High-Speed Machines", Annals of the CIRP, Vol. 44, pp. 353-356.

[9] Chiu G.T.-C., Tomizuka M., 2001, "Contouring control of machine tool feed drive systems: a task coordinate frame approach", IEEE Transactions on Control Systems Technology, Vol. 9, No. 1, pp. 130-139.

[10] Control System Toolbox User's Guide, 1999, The MathWorks Inc.

[11] Cuttino J.F., Dow T.A., Knight B.F., 1997, "Analytical and experimental identification of nonlinearities in a single-nut preloaded ball screw", Transactions of ASME, Journal of Mechanical Design, Vol. 119, No. 1, pp. 15-19.

[12] DeCarlo R.A., Zak S.H., Matthews G.P, 1988, "Variable Structure Control of Nonlinear Multivariable Systems: A Tutorial", Proceedings of the IEEE, Vol. 76, No. 3, pp. 212-232.

[13] Donmez M.A., Blomquist D.S., Hocken R.J., Liu C.R., Barash M.M., 1986, "A general methodology for machine tool accuracy enhancement by error compensation", Precision Engineering, Vol. 8, No. 4, pp. 187-196.

[14] Erkorkmaz K., Altintas Y., 1998, "High Speed Contouring Control Algorithm for CNC Machine Tools", Proceedings of the ASME Dynamic Systems and Control Division, DSC-64, pp. 463-469.

[15] Erkorkmaz K., 1999, "High Speed Contouring Control for Machine Tool Drives", M.Sc. Thesis, University of British Columbia, Department of Mechanical Engineering, Vancouver.

[16] Erkorkmaz K., Altintas Y., 2001, "High Speed CNC System Design: Part I - Jerk Limited Trajectory Generation and Quintic Spline Interpolation", International Journal of Machine Tools and Manufacture, Vol. 41, No. 9, pp. 1323-1345.

[17] Erkorkmaz K., Altintas Y., 2001, "High speed CNC system design. Part II: modeling and identification of feed drives", International Journal of Machine Tools and Manufacture, Vol. 41, No. 10, pp. 1487-1509.

[18] Erkorkmaz K., Altintas Y., 2001, "High speed CNC system design. Part III: high speed tracking and contouring control of feed drives", International Journal of Machine Tools and Manufacture, Volume 41, No. 11, pp. 1637-1658.

[19] Erkorkmaz K., 2004, "Optimal Trajectory Generation and Precision Tracking Control for Multi-Axis Machines", PhD Thesis, University of British Columbia.

[20] Erkorkmaz K., Altintas Y., 2005, "Precision Tracking Controller Design for High Speed Feed Drives", Proceedings of the ASME Dynamic Systems and Control Division, IMECE'05, Orlando, Florida.

[21] Erkorkmaz K., Kamalzadeh A., 2006, "High bandwidth control of ball screw drives", Annals of CIRP, Vol. 55, No. 1, pp. 393-398.

[22] Ferretti G., Magnani G., Rocco P., 1998, "Modeling, Identification, and Compensation of Pulsating Torque in Permanent Magnet AC Motors", IEEE Trans. Ind. Elec., Vol. 45, No. 6, pp. 912-920.

[23] Gan W.C., Qiu L., 2004, "A Gain Scheduled Robust Regulator for Torque Ripple Elimination of AC Permanent Magnet Motor Systems", Proc. IEEE Intl. Conf. on Control Applications CCA'2004, Taiwan, pp. 284-289.

[24] Gan W.C., Qiu L., 2004, "Torque and Velocity Ripple Minimization of AC Permanent Magnet Motor Control Systems Using the Internal Model Principle", IEEE/ASME Trans. Mechatronics, Vol. 9, No. 2, pp. 436-447.

[25] Hyde J.M., Seering W.P., 1991, "Using Input Command Pre-Shaping to Suppress Multiple Mode Vibration", Proceedings of the IEEE International Conference on Robotics and Automation, Vol. 3, pp. 2604-2609.

[26] Heisel U., Koscsák G., Stehle T., 2006, "Thermography-based investigation into thermally induced positioning errors of feed drives by example of a ball screw", Annals of CIRP, Vol. 55, No. 1, pp. 423-426.

[27] Hillsley K.L., Yurkovich S., 1991, "Vibration control of a two-link flexible robot arm", Proc. IEEE International Conf. Robotics and Automation, Vol. 3, pp. 2121-2126.

[28] Jahns T.M., Soong W.L., 1996, "Pulsating Torque Minimization Techniques for Permanent Magnet AC Motor Drives-a Review", IEEE Transactions on Industrial Electronics, Vol. 43, No. 2, pp. 321–330.

[29] Jones S.D., Ulsoy A.G., 1999, "An approach to control input shaping with application to coordinate measuring machines", Transactions of ASME, Journal of Dynamic Systems, Measurement, and Control, Vol. 21, No. 2, pp. 242-247.

[30] Kalman R.E., 1960, "A New Approach to Linear Filtering and prediction Problems", Journal of Basic Engineering, Vol. 82, pp. 35-44.

[31] Kamalzadeh A., Erkorkmaz K., 2007, "Accurate Tracking Controller Design for High Speed Drives," International Journal of Machine Tools and Manufacture, Vol. 47, No. 9, pp. 1393-1400.

[32] Kamalzadeh A., Erkorkmaz K., 2007, "Compensation of Axial Vibrations in Ball Screw Drives", Annals of CIRP, Vol. 56, No. 1, pp. 373-378.

[33] Kamalzadeh A., Erkorkmaz K., 2007, "Compensation of lead errors and elastic deformations in ball screw drives", Proc. CIRP/NIST Intl. Conf. on Smart Machining Systems (ICSMS'07), Mar 13-15 Gaithersburg, MD, also to appear in CIRP - Journal of Manufacturing Systems, Vol. 36, No. 5, 2007.

[34] Kamalzadeh A., Erkorkmaz K., 2008, "Robust Compensation of Elastic Deformations in Ball Screw Drives", 3rd CIRP International Conference on High Performance Cutting, Dublin, Ireland, June 12-13 (also submitted to the International Journal of Machine Tools and Manufacture).

[35] Kato S., Sato N., Matsubayashi T., 1972, "Some Considerations on Characteristics of Static Friction of Machine Tool Slideway", ASME Journal of Lubrication Technology, Vol. 94, No. 3, pp. 234-247.

[36] Koren Y., 1980, "Cross-Coupled Biaxial Computer Control for Manufacturing Systems", ASME Journal of Dynamic Systems Measurement, and Control, vol. 102, pp. 265-272.

[37] Koren Y., Lo C.C., 1991, "Variable-Gain Cross-Coupling Controller for Contouring", Annals of CIRP, Vol. 40, No.1, pp. 371-374.

[38] Lee H.S., Tomizuka M., 1996, "Robust Motion Controller Design for High-Accuracy Positioning Systems", IEEE Transactions on Industrial Electronics, Vol. 43, No. 1, pp. 48-55.

[39] Le-Huy H., Perret R., Feuillet R., 1986, "Minimization of Torque Ripple in Brushless DC Motor Drives", IEEE Transactions in Industry Applications, Vol. IA-22, No. 4, pp. 748- 755.

[40] Levi, E.C., 1959, "Complex-Curve Fitting", IRE Trans. Automatic Control, Vol. AC-4, pp. 37-44.

[41] Lim H., Seo J.W., Choi C.H., 2000, "Position Control of XY Table in CNC Machining Center with Non-rigid Ballscrew", Proceedings of the American Control Conference, pp. 1542-1546.

[42] Lim H., Seo J.W., Choi C.H., 2001, "Torsional Displacement Compensation in Position Control for Machining Centers", Control Engineering Practice, Vol. 9, No. 1, pp 79-87.

[43] Lin M.C., Ravani B., Velinsky S.A., 1994, "Kinematics of the Ball Screw Mechanism", ASME Journal of Mechanical Design, Vol. 116, No. 3, pp. 849-855.

[44] Ljung L., 1998, System Identification: Theory For The User, 2nd Edition, Prentice-Hall of Canada Ltd.

[45] Matsui N., Makino T., Satoh H., 1993, "Autocompensation of Torque Ripple of Direct Drive Motor by Torque Observer", IEEE Transactions on Industry Applications, Vol. 29, No. 1, Part 1, pp. 187-194.

[46] Nagase K., Okuyama T., Takahashi J., Saitoh K., 1989, "A Method for Suppressing Torque Ripple of an AC Motor by Current Amplitude Control", IEEE Transactions on Industrial Electronics, Vol. 36, No. 4, pp. 504-510.

[47] Ogata K., 1987, Discrete-Time Control Systems, Prentice-Hall, Englewood Cliffs, NJ.

[48] Ogata K., 1997, "Modern. Control Engineering", Third Edition, Prentice-Hall, NJ.

[49] Okwudire C., 2005, M.Sc. Thesis: Finite Element Modeling of Ballscrew Feed Drive Systems for Control Purpose, The University of British Columbia", Department of Mechanical Engineering, Vancouver, Canada.

[50] Parasiliti F., Petrella R., Tursini M., 1999, "Torque Ripple Compensation in Permanent Magnet Synchronous Motors Based on Kalman Filter", Proc. IEEE Conf. on Ind. Electronics, ISIE '99, Vol. 3, pp. 1333-1338.

[51] Petrovic V., Ortega R., Stankovic A.M., Tadmor G., 2000, "Design and Implementation of an Adaptive Controller for Torque Ripple Minimization in PM Synchronous Motors", IEEE Trans. Power Elec., Vol. 15, No. 5, pp. 871-880.

[52] Pritschow G., Philipp W., 1992, "Research on the Efficiency of Feedforward Controllers in Direct Drives", Annals of CIRP, Vol. 41, No. 1, pp. 411-415.

[53] Pritschow G., 1996, "On the Influence of the Velocity Gain Factor on the Path Deviation", Annals of CIRP, Vol. 45, No. 1, pp. 367-371.

[54] Pritschow G., 1998, "A Comparison of Linear and Conventional Electromechanical Drives", Annals of CIRP, Vol. 47, No. 2, pp. 541-548.

[55] Sadegh N., Horowitz R., 1990, "Stability and Robustness Analysis of a Class of Adaptive Controllers for Robotic Manipulators", International Journal of Robotics Research, Vol. 9, No. 3, pp. 74-92.

[56] Schäfers E., 2006, "Mechatronic Modeling and Analysis of Machine Tools", Proc. 2nd International Conference on High Performance Cutting (CIRP-HPC'06), Vancouver, June 12-13.

[57] Schulz H., Würz T., 1998, "Balancing Requirements for Fast Rotating Tools and Spindle Systems", Annals of CIRP - Manufacturing Technology, Vol. 47, No. 1, pp. 321-324.

[58] Skogestad S., Postlethwaite I., 1996, Multivariable Feedback Control: Analysis and Design, John Wiley & Sons.

[59] Slocum A.H., 1992, “Precision Machine Design”, Society of Manufacturing Engineers, Dearborn MI.

[60] Slotine J.J.E., Li W., 1988, “Adaptive Manipulator Control: A Case Study”, IEEE Transactions on Automatic Control, Vol. 33, No. 11, pp. 995-1003.

[61] Smith O.J.M, 1958, Feedback Control Systems, McGraw-Hill Book Company, Inc., New York, N.Y., pp. 331-345.

[62] Smith A.D., 1999, Ph.D. Thesis: Wide Bandwidth Control of High-Speed Milling Machine Feed Drives, University of Florida, Department of Mechanical Engineering, Florida.

[63] Symbolic Math Toolbox User’s Guide, 1998, The MathWorks Inc., Natick, MA.

[64] Symens W., Van Brussel H., Swevers J., 2004, “Gain-Scheduling Control of Machine Tools with Varying Structural Flexibility”, Annals of CIRP, Vol. 53, No. 1, pp. 321-324.

[65] Tomizuka M., 1987, “Zero Phase Error Tracking Algorithm for Digital Control”, ASME Journal of Dynamic Systems, Measurement, and Control, Vol. 109, pp. 65-68.

[66] Tung E.D., Tomizuka M., 1993, “Feedforward Tracking Controller Design Based on the Identification of Low Frequency Dynamics”, ASME Journal of Dynamic Systems, Measurement and Control, Vol. 115, No. 3, pp. pp. 348-356.

[67] Utkin V.I., 1977, “Variable Structure System with Sliding Modes”, IEEE Transactions on Automatic Control, Vol. AC-22, No. 2, pp.212-222.

[68] Varanasi K.K., Nayfeh S.A., 2004, “Dynamics of Lead-Screw Drives: Low-Order Modeling and Experiments”, Dynamic Systems, Measurement, and Control, Vol. 126, pp. 388-396.

[69] Weck M., Ye G., 1990 “Sharp corner tracking using the IKF control strategy”, Annals of CIRP, Vol. 39, No. 1, pp. 437-441.

[70] Wei C.W., Lin J.F., 2003, “Kinematic analysis of the ball screw mechanism considering variable contact angles and elastic deformations”, Transactions of ASME, Journal of Mechanical Design, Vol. 125, No. 4, pp. 717-733.

[71] Zaeh M.F., Oertli T., Milberg J., 2004, “Finite element modeling of ball screw feed drive systems”, Annals of CIRP, Vol. 53, No. 1, pp. 289-292.

[72] Zatarain M., Ruiz de Argandoña I., Illarramendi A., Azpeitia J.L., Bueno R., 2005, “New Control Techniques Based on State Space Observers for Improving the Precision and Dynamic Behaviour of Machine Tools”, Annals of CIRP, Vol. 54, No. 1, pp. 393-396.

[73] Zhang G., Furusho J., Kajitani M., 1996, “Control of Flexible-Joint Manipulators Using Joint Torque and Acceleration Feedback”, Proceedings of the 3rd International Conference on Motion and Vibration Control, Vol.1, pp. 245-250.

[74] Zhang G., Furusho J., 1998, “Control of Robot Arms using Joint Torque Sensors”, IEEE Control Systems Magazine, Vol. 18, No.1, pp. 48–55.

[75] Zhu W.H., Xi Y.G., Zhang Z.J., Bien Z., De Schutter J., 1997, "Virtual Decomposition Based Control for Generalized High Dimensional Robotic Systems with Complicated Structure", IEEE Trans. Robotics & Automation, Vol. 13, No. 3, pp. 411-436.

Appendix A:
Least Squares Identification of Rigid Body Dynamics

This appendix details the method for identification of the drive's rigid body dynamics using Least Squares technique, considering inertia, viscous damping, and Coulomb friction effects.

The dynamics of the drive can be expressed as:

$$\omega(s) = \frac{1}{Js + B}[\tau - T_d] \tag{A.1}$$

as in Eq. (3.4), which can be re-expressed as (Eq. (3.6)):

$$x(s) = \frac{r_g}{s}\frac{1}{Js + B}[K_a K_t u(s) - T_d(s)] \tag{A.2}$$

in terms of axis position.

Above, ω is the angular velocity of the ball screw. J is the motor-equivalent total rotary inertia, B is the viscous friction coefficient, and τ is the motor torque. The disturbance torque (T_d) which is assumed to be mainly due to the Coulomb friction (when the machine is not cutting) is considered in the form of:

$$T_d = \begin{cases} T_C^+ & for \quad \omega > 0 \\ T_C^- & for \quad \omega < 0 \end{cases} \tag{A.3}$$

The ball screw rotational-to-translational motion conversion ratio is $r_g = h_p/(2\pi) = 3.1831\times10^{-3}$ m/rad. The motor torque can be expressed as $\tau(s) = K_a K_t u(s)$, where $u(s)$ is the amplifier input. K_a and K_t are the amplifier gain and the motor torque constants, with catalogue rated values of 1.7193 A/V and 0.57 Nm/A respectively.

The disturbance torque, T_d, can be expressed as a control signal equivalent disturbances:

$$d(s) = T_d(s)/K_a K_t \tag{A.4}$$

In order to simplify the formulation, inertia and viscous friction parameters can be represented by two other parameters, $K_v(s) = K_a K_t / J$ and $p_v(s) = -B/J$, leading to the following expression for the drive's angular velocity in terms of the control signal:

$$\omega(s) = \frac{K_v}{s - P_v}[u(s) - d(s)] \tag{A.5}$$

Correspondingly, the axis position can be written as,

$$x(s) = \frac{r_g}{s}\omega(s) = \frac{r_g}{s} \cdot \frac{K_v}{s - p_v}[u(s) - d(s)] \tag{A.6}$$

Selecting the axis position and velocity as two states, Eq. (A.6) can be transformed into state space form as:

$$\begin{bmatrix} \dot{x}(t) \\ \dot{\omega}(t) \end{bmatrix} = \boldsymbol{A}_c \begin{bmatrix} x(t) \\ \omega(t) \end{bmatrix} + \begin{bmatrix} \boldsymbol{B}_c & -\boldsymbol{B}_c \end{bmatrix} \begin{bmatrix} u(t) \\ d(t) \end{bmatrix}, \text{ where } \boldsymbol{A}_c = \begin{bmatrix} 0 & r_g \\ 0 & p_v \end{bmatrix} \text{ and } \boldsymbol{B}_c = \begin{bmatrix} 0 \\ K_v \end{bmatrix} \tag{A.7}$$

As the control signal is generated through a digital-to-analog convertor using a sampling frequency of T_s, the velocity expression in Eq. (A.5) can be expressed in discrete-time considering a zero order hold at the input [6] as:

$$\omega(k) = \frac{K_{vd}}{z - p_{vd}}[u(k) - d(k)] \quad \text{, where } K_{vd} = \frac{K_v}{-p_v}(1 - e^{p_v T_s}) \text{ and } p_{vd} = e^{p_v T_s} \tag{A.8}$$

Above, K_{vd} and p_{vd} are the gain and pole of the discrete-time transfer function, z is the discrete-time forward shift operator , and k is the sample counter.

Using the above definitions, the discrete-time state space form of Eq. (A.7) is obtained as:

$$\begin{bmatrix} x(k+1) \\ \omega(k+1) \end{bmatrix} = \boldsymbol{A}_d \begin{bmatrix} x(k) \\ \omega(k) \end{bmatrix} + \begin{bmatrix} \boldsymbol{B}_d & -\boldsymbol{B}_d \end{bmatrix} \begin{bmatrix} u(k) \\ d(k) \end{bmatrix} \tag{A.9}$$

$$\text{where } \boldsymbol{A}_d = e^{\boldsymbol{A}_c T_s} \text{ and } \boldsymbol{B}_d = \int_0^{T_s} e^{\boldsymbol{A}_c \lambda} d\lambda \cdot \boldsymbol{B}_c$$

In order to include the effect of Coulomb friction into the rigid body dynamic identification, the following model has been assumed to represent this friction:

$$T_f = \begin{cases} 0 & for \ \ \omega = 0 \\ T_C^+ & for \ \ \omega > 0 \\ T_C^- & for \ \ \omega < 0 \end{cases} \tag{A.10}$$

where T_C^+ and T_C^- are the Coulomb friction parameters for positive and negative directions of motion. Their control signal equivalent values will be $d_f^+ = T_C^+ / K_a K_t$ and $d_f^- = T_C^- / K_a K_t$.

For joint identification of the inertia, viscous damping, and Coulomb friction parameters, the friction model in Eq. (A.10) is combined with the rigid body model in Eq. (A.8). In order to avoid oscillations in the friction model, due to noise in the velocity estimate when the axis is at rest, a sign function is defined with a dead band velocity Ω_d that is just above the velocity measurement noise floor ,

$$\gamma(\omega) = \begin{cases} 0 & for \quad |\omega| \le \Omega_d \\ +1 & for \quad \omega > \Omega_d \\ -1 & for \quad \omega < -\Omega_d \end{cases} \tag{A.11}$$

Consequently, the friction model scaled to the level of the control signal can be expressed as:

$$d_f(\omega(k)) = PV(\omega(k)) \cdot d_f^+ + NV(\omega(k)) \cdot d_f^- \tag{A.12}$$

where:

$$PV: Positive\ Velocity = \frac{1}{2}\gamma(\omega(k)) \cdot (1 + \gamma(\omega(k))) \tag{A.13}$$

$$NV: Nagetive\ Velocity = -\frac{1}{2}\gamma(\omega(k)) \cdot (1 - \gamma(\omega(k)))$$

Now, the rigid body model in Eq. (A.8) can be combined with the control signal equivalent friction model in Eq. (A.12), resulting in:

$$\omega(k) = p_{vd}\,\omega_m(k-1) + K_{vd}\,u(k-1) - [K_{vd}\,d_f^+ \cdot PV(\omega(k-1)) + K_{vd}\,d_f^- \cdot NV(\omega(k-1))] \tag{A.14}$$

The above equation can be written in parameter-regressor form as:

$$\omega(k) = [\omega_m(k-1) \quad u(k-1) \quad -PV(\omega(k-1)) \quad -NV(\omega(k-1))] \begin{bmatrix} p_{vd} \\ K_{vd} \\ K_{vd}\,d_f^+ \\ K_{vd}\,d_f^- \end{bmatrix} \tag{A.15}$$

Considering the availability of the regressor terms and defining the input vector $\mathbf{u} = [u(1),\ u(2),\ ...,u(k-1)]^T$, the velocity vector $\boldsymbol{\omega} = [\omega(2),\ \omega(2),\ ...,\omega(k)]^T$, and parameter vector

$\boldsymbol{\theta} = [p_{vd} \quad K_{vd} \quad K_{vd} d_f^+ \quad K_{vd} d_f^-]^T$, the parameter estimation is cast as a Least Squares (LS) problem where the estimation output vector ($\boldsymbol{Y}$) is:

$$\boldsymbol{Y} = \boldsymbol{\Phi\theta} + \boldsymbol{E} \tag{A.16}$$

or

$$\boldsymbol{\Phi} = \begin{bmatrix} \omega_m(1) & u(1) & -PV(1) & -NV(1) \\ \omega_m(2) & u(2) & -PV(2) & -NV(2) \\ \cdots & \cdots & \cdots & \cdots \\ \omega_m(N-1) & u(N-1) & -PV(N-1) & -NV(N-1) \end{bmatrix} \begin{bmatrix} p_{vd} \\ K_{vd} \\ K_{vd} d_f^+ \\ K_{vd} d_f^- \end{bmatrix} + \boldsymbol{E}$$

Above, $\boldsymbol{E}$ is the vector of output prediction errors. In the LS problem above, the objective is to find the optimal set of parameters, $\hat{\boldsymbol{\theta}}$ in order to minimize the sum of the squares of output prediction errors,

$$\min(\frac{1}{2}\boldsymbol{E}^T\boldsymbol{E}) = \min(\frac{1}{2}(\boldsymbol{Y} - \boldsymbol{\Phi\theta})^T(\boldsymbol{Y} - \boldsymbol{\Phi\theta})) \tag{A.17}$$

which is solved as [44]:

$$\hat{\boldsymbol{\theta}} = (\boldsymbol{\Phi}^T\boldsymbol{\Phi})^{-1}\boldsymbol{\Phi}\cdot\boldsymbol{Y} \tag{A.18}$$

Referring to the definition of K_{vd} and p_{vd} in (A.8), and noting that $K_v(s) = K_a K_t / J$ and $P_v(s) = -B/J$, the estimated inertia, viscous damping, and Coulomb friction parameters can be determined as:

$$\hat{J} = \frac{(\hat{P}_{vd} - 1)K_a K_t T_s}{\hat{K}_{vd} \ln(\hat{P}_{vd})} = \frac{(\hat{\boldsymbol{\theta}}(1) - 1)K_a K_t T_s}{\hat{\boldsymbol{\theta}}(2)\ln(\hat{\boldsymbol{\theta}}(1))} \tag{A.19}$$

$$\hat{B} = \frac{(1 - \hat{P}_{vd})K_a K_t}{\hat{K}_{vd}} = \frac{(1 - \hat{\boldsymbol{\theta}}(1))K_a K_t}{\hat{\boldsymbol{\theta}}(2)} \tag{A.20}$$

$$T_C^+ = K_a K_t d_f^+ = K_a K_t \hat{\boldsymbol{\theta}}(3) / \hat{\boldsymbol{\theta}}(2) \tag{A.21}$$

$$T_C^- = K_a K_t d_f^- = K_a K_t \hat{\boldsymbol{\theta}}(4) / \hat{\boldsymbol{\theta}}(2) \tag{A.22}$$

Appendix B:
Kalman Filter Design

This appendix details the design of a Kalman filter for disturbance observation in the drive, which is used in identification of friction and torque ripples in Chapter 3 and Chapter 5. The Kalman filter design here is based on the methodology applied in [17]. The filtering schematic was presented earlier in Chapter 3, and is shown here in Figure B.1. The ball screw drive motion is under control while the Kalman filter estimates the disturbance using the input torque and measured rotational position.

The Kalman filter is an observer designed to estimate the states of a dynamic system, where the system inputs and the measurements are corrupted by noise with known statistical properties (variances). The dynamic system is assumed to have a certain model with known parameters. Selecting the axis rotational displacement and velocity as two states, the following continuous state space model is assumed to hold for the ball screw drive dynamics, which is similar to Eq. (A.9) :

$$\begin{bmatrix} \dot{\theta}(t) \\ \dot{\omega}(t) \end{bmatrix} = \boldsymbol{A}_c \begin{bmatrix} \theta(t) \\ \omega(t) \end{bmatrix} + \begin{bmatrix} \boldsymbol{B}_c & -\boldsymbol{B}_c \end{bmatrix} \begin{bmatrix} u(t) \\ d(t) \end{bmatrix}, \text{ where } \boldsymbol{A}_c = \begin{bmatrix} 0 & 1 \\ 0 & p_v \end{bmatrix} \text{ and } \boldsymbol{B}_c = \begin{bmatrix} 0 \\ K_v \end{bmatrix} \tag{B.1}$$

where $K_v(s) = K_a K_t / J$ and $P_v(s) = -B / J$.

Considering the sampling frequency of T_s (0.125 msec in the Kalman filter design), the discrete-time form of the above state space model can be written as:

$$\begin{bmatrix} \theta(k+1) \\ \omega(k+1) \end{bmatrix} = \boldsymbol{A}_d \begin{bmatrix} \theta(k) \\ \omega(k) \end{bmatrix} + \begin{bmatrix} \boldsymbol{B}_d & -\boldsymbol{B}_d \end{bmatrix} \begin{bmatrix} u(k) \\ d(k) \end{bmatrix} \tag{B.2}$$

where $\mathbf{A}_d$ and $\mathbf{B}_d$ are calculated as $\mathbf{A}_d = e^{\mathbf{A}_c T_s}$ and $\boldsymbol{B}_d = \int_0^{T_s} e^{\boldsymbol{A}_c \lambda} d\lambda \cdot \boldsymbol{B}_c$ [47].

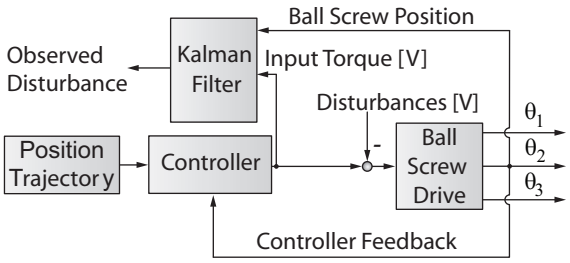

Figure B.1: Kalman filtering block diagram.

In order to design the Kalman filter, variances of the input torque and position measurement noise need to be estimated. The input torque command (control signal or u) is generated by a 16-bit Digital-to-Analog convertor with ± 10 V output range. Hence, the resolution is $\delta u = (20/2^{16}) = 3.052\text{x}10^{-4}$ V. The difference ($\tilde{u}$) between the ideal input u and DAC output $u*$, can assume values between $-\delta u$ and $+\delta u$, and is considered to have a uniform distribution. Assuming a zero mean value for $\tilde{u}$, ($E\{\tilde{u}\} = 0$), its variance can be calculated as:

$$R_{\tilde{u}} = E\{(\tilde{u} - E\{\tilde{u}\})^2\} = E\{\tilde{u}^2\} = \int_{-\infty}^{\infty} p(\tilde{u}) \cdot \tilde{u}^2 \cdot d\tilde{u} = \int_{-\delta u/2}^{\delta u/2} \frac{1}{\delta u} \cdot \tilde{u}^2 \cdot d\tilde{u} = \frac{(\delta u)^2}{12} \tag{B.3}$$

$$R_{\tilde{u}} = 7.761\times10^{-9} \quad \text{V}^2$$

High resolution rotary encoders instrumented on the setup (Encoder 1 and 2) generate 5000 sine waves per revolution, which can be reliably interpolated 400 times in the data acquisition system. Using Encoder 2 for the Kalman filtering, a resolution of

$$\delta\theta = \frac{2\pi \ [rad]}{5000\times400} = 3.142\times10^{-6} \text{ rad} \tag{B.4}$$

is achieved, which is equivalent to 10 nm of table linear motion.

Similar to $\tilde{u}$, $\tilde{\theta}$ is the difference between the actual position (θ) and the measured position (θ_m),

$$\tilde{\theta} = \theta_m - \theta \tag{B.5}$$

Assuming $\tilde{\theta}$ to have a uniform distribution between $-\delta\theta/2$ and $\delta\theta/2$, where $\delta\theta = 3.142\times10^{-6}$ rad is the encoder resolution, the position measurement variance can be expressed as,

$$R_{\tilde{\theta}} = \frac{(\delta\theta)^2}{12} = \frac{(3.142\times10^{-6})^2}{12} = 8.2247\times10^{-13} \quad \text{rad}^2 \tag{B.6}$$

The disturbance can be added as a 3rd variable into the model in B.2, enabling the Kalman filter to estimate it as a dynamic state. The disturbance state ($d(k)$) is assumed to consist of a piecewise constant signal with a perturbation of w_d as follows,

$$d(k+1) = d(k) + w_d(k) \ \text{[V]} \tag{B.7}$$

The disturbance perturbation variance, $R_{wd} = \text{var}\{w_d\}$, will be used as a tuning parameter in the design, which determines the speed and aggressiveness of the Kalman filter. Incorporating Eq. (B.7)

into the state space model in Eq. (B.2), and considering $\tilde{u}$, the difference between the ideal u and actual DAC output u^*, the following augmented state-space model is obtained:

$$\begin{bmatrix} \theta(k+1) \\ \omega(k+1) \\ d(k+1) \end{bmatrix} = \boldsymbol{A} \begin{bmatrix} \theta(k) \\ \omega(k) \\ d(k) \end{bmatrix} + \boldsymbol{B}[u(k)] + \boldsymbol{W} \begin{bmatrix} \tilde{u}(k) \\ \tilde{w}_d(k) \end{bmatrix}, \tag{B.8}$$

$$\text{where } \boldsymbol{A} = \begin{bmatrix} \boldsymbol{A_d} & -\boldsymbol{B_d} \\ 0_{1\times 2} & 1 \end{bmatrix}, \boldsymbol{B} = \begin{bmatrix} \boldsymbol{B}_d \\ 0 \end{bmatrix}, \text{ and } \boldsymbol{W} = \begin{bmatrix} \boldsymbol{B}_d & 0_{2\times 1} \\ 0 & 1 \end{bmatrix}$$

Considering the measurement noise of the rotary encoder, $\tilde{\theta} = \theta_m - \theta$, the measured output, θ_m can be expressed in terms of the states as,

$$[\theta_m(k)] = \boldsymbol{C} \begin{bmatrix} \theta(k) \\ \omega(k) \\ d(k) \end{bmatrix} + \boldsymbol{V}[\tilde{\theta}(k)], \tag{B.9}$$

$$\text{where } \boldsymbol{C} = [1 \;\; 0 \;\; 0], \text{ and } \boldsymbol{V} = [1]$$

In the above state space model, $\boldsymbol{A}$ and $\boldsymbol{B}$ are the augmented system and input matrices. $\boldsymbol{W}$ determines how the process noise vector $[\tilde{u}(k) \;\; \tilde{w}_d(k)]^{\mathrm{T}}$ affects the state transition. $\boldsymbol{C}$ is the output matrix and $\boldsymbol{V}$ relates the measurement noise $\tilde{\theta}$ to the measured angular position θ_m. The numerical values of $\boldsymbol{A}$ and $\boldsymbol{B}$, in the above state space model can be obtained by substituting the dynamic parameters identified in Chapter 3 (J =2.1×10^{-3} kgm^2, B =1.015 kgm^2/sec), and rated values for the amplifier gain and motor constant (K_a = 1.7193 A/V, K_t = 0.57 Nm/A) into Eq. (B.1), and following the rest of the formulation in this appendix. Hence, $\boldsymbol{A}$ and $\boldsymbol{B}$ are obtained as:

$$\boldsymbol{A} = \begin{bmatrix} 1 & 1.2500\times 10^{-4} & 3.6458\times 10^{-6} \\ 0 & 0.999939 & 5.8332\times 10^{-2} \\ 0 & 0 & 1 \end{bmatrix}, \text{ and } \boldsymbol{B} = \begin{bmatrix} 3.6458\times 10^{-6} \\ 5.8332\times 10^{-2} \end{bmatrix} \tag{B.10}$$

The Kalman filter estimates the angular position, velocity, and disturbance in the following form,

$$\begin{bmatrix} \hat{x}(k) \\ \hat{\omega}(k) \\ \hat{d}(k) \end{bmatrix} = (\mathbf{I} - \mathbf{K}_{obs}\mathbf{C})\mathbf{A} \begin{bmatrix} \hat{x}(k-1) \\ \hat{\omega}(k-1) \\ \hat{d}(k-1) \end{bmatrix} + (\mathbf{I} - \mathbf{K}_{obs}\mathbf{C})\mathbf{B}[u(k-1)] + \mathbf{K}_{obs} \begin{bmatrix} x_m(k) \\ \omega_m(k) \end{bmatrix} \tag{B.11}$$

The filter design requires obtaining the constant observer gain $\boldsymbol{K}_{obs}$ through the below off-line iteration until the individual entries of $\boldsymbol{K}_{obs}$ converge to steady-state values [30],

$$\begin{aligned}
&\boldsymbol{P}(k\,|\,k-1) = \boldsymbol{A}\boldsymbol{P}(k-1\,|\,k-1)\boldsymbol{A}^{\mathrm{T}} + \boldsymbol{W}\boldsymbol{R}_{\boldsymbol{w}}\boldsymbol{W}^{\mathrm{T}} \\
&\boldsymbol{K}_{obs}(k) = \boldsymbol{P}(k\,|\,k-1)\boldsymbol{C}^{\mathrm{T}}[\boldsymbol{R}_{\boldsymbol{v}} + \boldsymbol{C}\boldsymbol{P}(k\,|\,k-1)\boldsymbol{C}^{\mathrm{T}}]^{-1} \\
&\boldsymbol{P}(k\,|\,k) = [\boldsymbol{I} - \boldsymbol{K}_{obs}(k)\boldsymbol{C}]\boldsymbol{P}(k\,|\,k-1)
\end{aligned} \tag{B.12}$$

where $\boldsymbol{R}_{\boldsymbol{w}} = \mathrm{diag}\{R_{\tilde{u}}, R_{wd}\}$ and $\boldsymbol{R}_{\boldsymbol{v}} = [R_{\tilde{\theta}}]$.

In the above equations, $\boldsymbol{P}(k-1\,|\,k-1)$ is the covariance of state estimation error for iteration $k-1$. $\boldsymbol{P}(k\,|\,k-1)$ is its prediction to the next iteration based on knowledge of plant dynamics ($\boldsymbol{A}$) and process input noise ($\boldsymbol{W}$ and $\boldsymbol{R}_{\boldsymbol{w}}$). The gain $\boldsymbol{K}_{obs}$ is then computed to yield an optimal state estimate, considering the effect of measurement noise ($\boldsymbol{R}_{\boldsymbol{v}}$). Finally, using the new value of the state estimation gain $\boldsymbol{K}_{obs}$, the state estimation error covariance is updated to $\boldsymbol{P}(k\,|\,k)$ for the next iteration.

In the iterative calculation process, $\boldsymbol{P}(k\,|\,k)$ is initially set to a large value (e.g. $\boldsymbol{P}(1\,|\,1) = \alpha\boldsymbol{I}$) where α is a large number (10^{12}). $\boldsymbol{K}_{obs}$ is initially set to zero and is obtained after the convergence of iterative algorithm, usually within the first 50 or 100 iterations. The steady-state value of $\boldsymbol{K}_{obs}$ is then used in Eq. (B.11) to obtain the state estimates $[\hat{x}(k)\ \hat{\omega}(k)\ \hat{d}(k)]^{\mathrm{T}}$.

The disturbance perturbation variance (R_{wd}) is tuned in tracking tests where the estimated disturbance $\hat{d}$ is desired to approach the constant steady-state value of Coulomb friction reasonably quickly, without too much oscillation. At the same time, minimal noise and oscillation level is desired in the $\hat{d}$ estimate. Higher values of R_{wd} lead to a faster estimate, but also higher sensitivity to noise. By trial and error, R_{wd} was tuned to be:

$$R_{wd} = 77\times10^{-7} \quad \mathrm{V}^2 \tag{B.13}$$

resulting in reasonably fast estimation and also acceptable noise level.

Considering the covariance values,

$$\boldsymbol{R}_{\boldsymbol{w}} = diag\{R_{\tilde{u}}, R_{wd}\} = \begin{bmatrix} 7.761\times10^{-9} & 0 \\ 0 & 77\times10^{-7} \end{bmatrix} \text{ and } \boldsymbol{R}_{\boldsymbol{v}} = [R_{\tilde{\theta}}] = 8.2247\times10^{-13} \tag{B.14}$$

after iterating Eq. (B.12) using the state space matrices in Eq. (B.8) and (B.9), the state estimation gain was obtained as:

$$\boldsymbol{K}_{obs} = \begin{bmatrix} 0.430486 \\ 0.963055\times10^{3} \\ 2.30976\times10^{3} \end{bmatrix} \tag{B.15}$$

Hence, observer poles ($\mathrm{eig}([\boldsymbol{I} - \boldsymbol{K}_{obs}\boldsymbol{C}]\boldsymbol{A})$) with the following natural frequency and damping ratio values were obtained, which determine the "activeness" of the designed Kalman filter:

$$p_{1,2,3} = 358\ \mathrm{Hz},\ \zeta_{1,2} = 0.5,\ \zeta_{3} = 1.$$

Appendix C:
Finite Element Analysis of the Ball Screw Drive

The layout of the ANSYS model is shown in Figure C.1. The FE modeling was briefly described in Section 3.4.1.

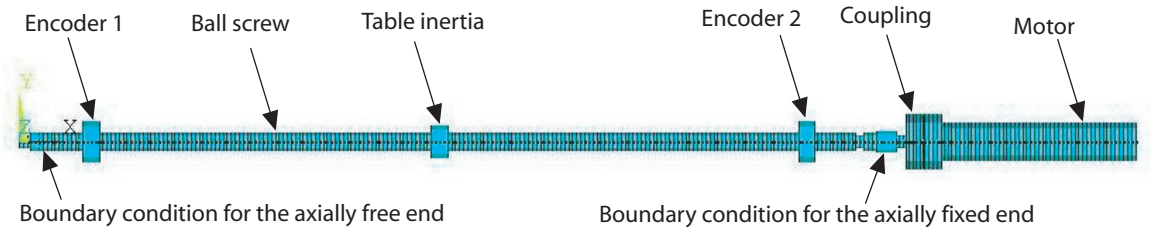

Figure C.1: Layout of FE model in ANSYS.

The element used for modeling of the ball screw, motor, coupling, bearing rings, and the disk representing the table inertia is a pipe element, ("PIPE16"), as illustrated in Figure C.2. The material selected for the model is steel with 210 MPa Young's modulus, 0.3 Poisson's ratio, and 7850 kg/m^3 density. The inner diameter for the elements was set to zero.

More details about the finite element model including the ball screw sections, inertias, and stiffness parameters are presented in Table C.1 through Table C.3. The axial position of the connection points, referenced from the free (left hand) end of the ball screw according to Figure C.1, are summarized in Table C.3. These points denote the connections between the table and the ball screw, the motor and the coupling, and the coupling and the ball screw.

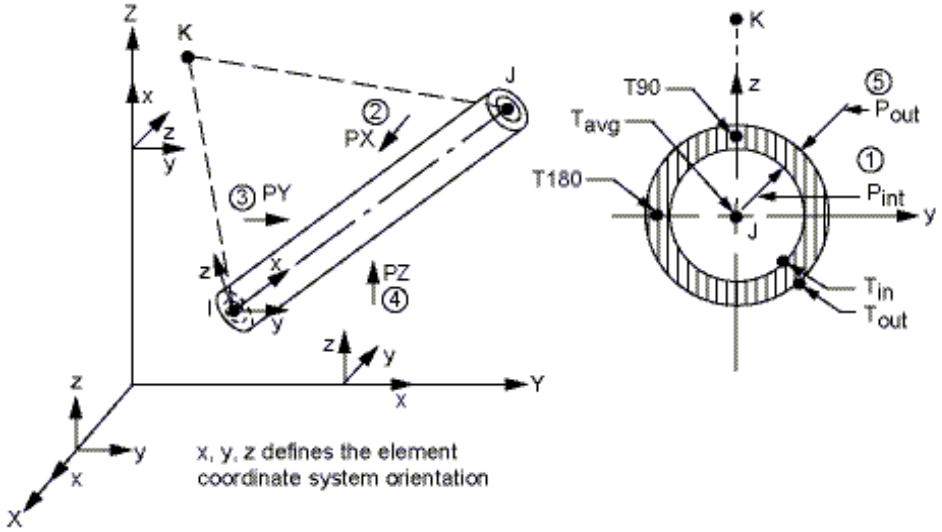

Figure C.2: ANSYS "PIPE16" element [4], source: ANSYS 2004.

The axial positions of Encoders 1, 2, and 3, illustrated in Figure C.1, are respectively 89, 974, 1360 mm from the free end of the ball screw. The torsional stiffness of the nut is calculated based on the catalogue value of its axial stiffness, as explained in the following. Considering the pitch (p = 20 mm) of the ball screw and the radial distance of rolling balls with respect to the ball screw central axis (r = 0.0105 m), the simplified free body diagram shown in Figure C.3(a) is used to represent the ball screw nut contact.

Table C.1: Details of the finite element model.

Section	Axial position (begins at) [mm]	Axial position (ends at) [mm]	Outside diam. [mm]	Inside diam. [mm]	Part	Boundary condition
1	0	15	15	0	Ball screw	
2	15	25	15	0	Ball screw	Y and Z fixed
3	25	1035	20	0	Ball screw	
4	1035	1045	15	0	Ball screw	
5	1045	1060	19.5	0	Ball screw	
6	1060	1075	15	0	Ball screw	X, Y, Z, Ry, and Rz fixed
7	1075	1100	15	0	Ball screw	
8	1100	1120	12	0	Ball screw	
9	1130.6	1380.6	46.6	0	Motor	X, Y, Z, Ry, and Rz fixed
10	1097	1117	65	0	Coupling (left part)	X, Y, Z, Ry, and Rz fixed
11	1120	1140	65	0	Coupling (right part)	X, Y, Z, Ry, and Rz fixed
12	510	530	37	0	Table inertia (represented by a disk)	
13	1060	1075	22	15	Right bearing inertia (represented by a ring)	
14	15	25	23	15	Left bearing inertia (represented by a ring)	

Table C.2: Inertia/stiffness parameters for the finite element model.

Parameters:	**Values:**
Coupling stiffness	39543 Nm/rad
Nut torsional stiffness (the stiffness for the torsional spring used to connect the ball screw to the disk representing the table) – the value is calculated from the axial stiffness of the nut given in its catalogue (137×10^6 N/m)	15104 Nm/rad
Inertia of the motor rotor	9.1×10^{-4} kgm^2
Full equivalent inertia of the table	3.3916×10^{-4} kgm^2

Table C.3: Connection points.

Connection between	**Axial position [mm] from the free end of the ball screw**
Table and the ball screw	520 for the table-at-the-middle position 670 for the table-at-right position 370 for the table-at-left position
Coupling and ball screw	1097
Motor and coupling	1140

The ball contact force, F_b, is the force transmitted by a single rolling ball. This force can be decomposed to three components in the axial (F_{ba}), tangential (F_{bt}), and radial (F_{br}) directions in a cylindrical coordinate aligned with the ball screw axis. Assuming a well designed ball screw, the radial component, F_{br}, is negligible [62] . As a result, the 3-dimensional free body diagram of the rolling ball is simplified to a planar diagram, shown in Figure C.3(a). Assuming n number of balls in contact, the resultant axial force is $F_a = nF_{ba}$ and the resultant transmitted torque is $\tau = nF_{bt}r$.

Figure C.3(b) shows an exaggerated deformation of a single ball in the nut. Similar to the decomposition of forces in the nut, the ball deformation (Δd) has two components of axial deformation (Δd_a) and tangential deformation (Δd_t). The tangential deformation results in an angular displacement between the ball screw and nut with the amount $\Delta\psi = \dfrac{\Delta d_t}{r}$ [rad].

The axial stiffness of the ball screw nut may be written as $k_a = \frac{F_a}{\Delta d_a} = \frac{nF_{ba}}{\Delta d_a}$, where $F_{ba} = F_b \cos\theta$ and $\Delta d_a = \Delta d \cos\theta$ as seen in Figure C.3. Substituting the expressions for F_{ba} and Δd_a yields,

$$k_a = \frac{F_b \cos\theta}{\Delta d \cos\theta} = \frac{nF_b}{\Delta d} \tag{C.1}$$

The torsional stiffness of ball screw nut may be defined as $k_t = \frac{\tau}{\Delta\psi}$. As shown in Figure C.3, $F_{bt} = F_b \sin\theta$ and $\Delta d_t = \Delta d \sin\theta$. Substituting τ, $\Delta\psi$, F_{bt}, and Δd_t,

$$k_t = \frac{\tau}{\Delta\psi} = \frac{nF_{bt} r}{(\frac{\Delta d_t}{r})} = \frac{nF_{bt} r^2}{\Delta d \sin\theta} = \frac{nF_b \sin\theta r^2}{\Delta d \sin\theta} = \frac{nF_b r^2}{\Delta d} \tag{C.2}$$

Using Eq. (C.1) and (C.2), the torsional stiffness can be expressed as

$$k_t = K_a r^2 \tag{C.3}$$

Using the catalogue values of K_a (137×10^6 N/m) and r (0.0105 m), the torsional stiffness can be calculated as

$$k_t = 137\times10^6 \times 0.0105^2 = 15104 \text{ Nm/rad} \tag{C.4}$$

This value is used for the nut torsional stiffness in the FE modeling.

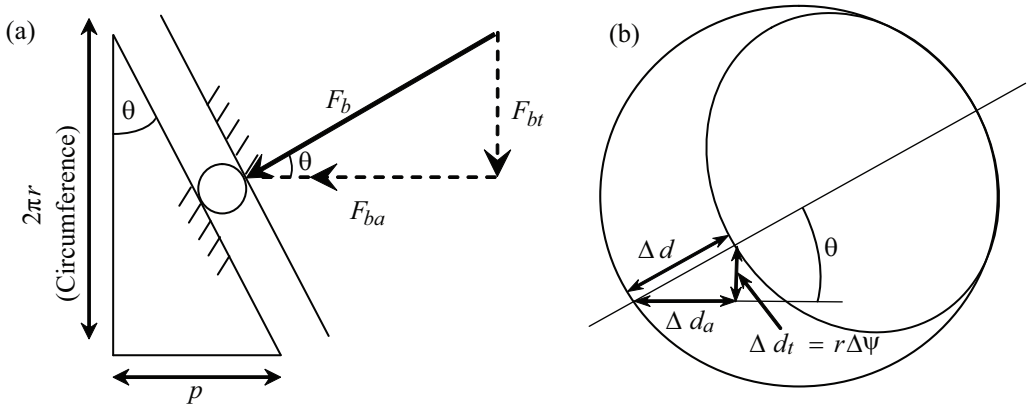

Figure C.3: Nut planar schematic: (a) Force components, (b) Deformation.